Dark Matter Search Experiment with Double Phase Xe Detector

二相型キセノン検出器による暗黒物質探索実験

Pure and applied Physics
Graduate School of Science and Engineering
Waseda University
Masaki Yamashita

2003 July

Abstract

There is strong evidences for the dark matter in our universe from various observations. A direct search for dark matter is important not only in astrophysics but in particle physics since there is a possibility that the dark matter is neutralino, which is the lightest super-partner in supersymmetric theories. The direct search, by means of nuclear recoil with low energy, is limited by the radioactive background from a detector itself as well as the sensitivity of the detector, which is required to have low energy threshold. However, there is the technique, which can distinguish nuclear recoil from electron recoil due to the background from a detector and the surrounding materials, developed using bolometric detectors combining with observation of ionization or scintillation signal.

CDMS, EDELWEISS and ZEPLIN I experiments, which have set the limit for a WIMP-nucleon cross section in the spin independent case, excludes DAMA allowed region. For further search such as the annual modulation, a detector with large volume will be required to have enough statistics for small event rate less than 10^{-1} count/day/kg/keV although the mass of bolometers used in previous experiments is a few hundreds grams per module.

From this point of view, a double phase Xe detector was proposed since it is easier to have large mass and the R & D for this detector has been carried out in the laboratory on the ground level from 1998 to 2001. We built the detector with 0.3 liter fiducial volume and measured its basic performance. We succeeded to utilize a PTFE reflector for liquid Xenon scintillation light and have been able to distinguish nuclear recoil from electron recoil using the direct scintillation and the proportional scintillation. From 2001, we started an underground experiment using a prototype detector in Kamioka mine, Japan. The background study, the radioactivity of all the materials used for this detector, was carried out using HPGe detector in the mine. Low background PMTs were developed by our group. The result of the prototype detector was 1 order of magnitude worse than the current limit in the WIMP-nucleon cross section. However, the origin of the radioactive source has been identified and the background level is understood quantitatively. The expected results with a 15 Kg detector in the next phase will be three order of magnitude better than the current limit.

Contents

Chapter 1

Introduction

1.1 Dark matter

"Dark Matter" signifies the invisible matter whose presence is only known through its gravitational effects. There is strong evidence from a variety of different observations for a large amount of dark matter in the Universe [1, 2].

The most robust evidence for dark matter comes from the rotation curve of spiral galaxies. Fig.1.1 shows the circular rotation velocities as a function of distance from the center. The circular velocities of clouds of neutral hydrogen can be measured by using 21-cm emission as a function of the distance r from the center of the galaxy. The orbital velocity distribution is expected from the Kepler's law,

$$v^2 = \frac{M(r)G}{r}, \tag{1.1}$$

where G is the gravitational constant and $M(r)$ is the total mass within a radius r. If the luminous matter was all there was, the rotation curve would drop at larger r, however the velocity curves stay flat even outside the luminous disk, it indicates $M(r) \propto r$. These observations show the existence of non-luminous matter.

1.2 Cosmology

It is convenient to scale energy densities to the critical density , $\rho_c \equiv 3H_0^2/8\pi G = 5.2 \times 10^{-6}$, H_0 is the present value of Hubble parameter.

$$\Omega_i \equiv \rho_i/\rho_c, \tag{1.2}$$

$$\Omega_0 \equiv \Sigma_i \Omega_i, \tag{1.3}$$

$$\begin{cases} \Omega_0 & > 1 \quad \text{open}, \\ \Omega_0 & = 1 \quad \text{flat}, \\ \Omega_0 & < 1 \quad \text{close}. \end{cases} \tag{1.4}$$

A value of total density Ω_0 can be estimated by the Cosmic Microwave Background (CMB) radiation experiments which study the power spectrum of its angular distribution.

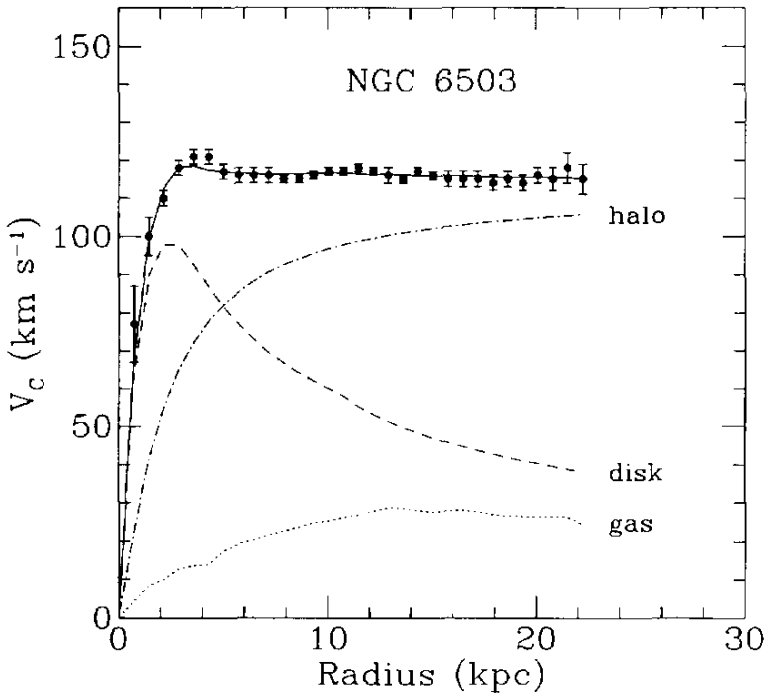

Figure 1.1: Rotation curve for the spiral galaxy NGC6503. The points are the measured circular rotation velocities as a function of distance from the center of the galaxy. The dashed and dotted curve are the contribution to the rotational velocity due to the observed disk and gas, respectively, and the dot-dash curve is the contribution from the dark halo. This figure is derived from Ref.[3].

Boomerang[4] gives $\Omega_0 = 1.02 \pm 0.06$, DASI[5] 1.04 ± 0.06, MAXIMA[6] $0.9^{+0.18}_{-0.16}$. These result are consistent with the generic prediction $\Omega_0 = 1$ of inflationary models.

Type Ia supernovae provide the information on the relationship between redshift and distance [7]. The result gives

$$0.8\Omega_M - 0.6\Omega_\Lambda \sim -0.2 \pm 0.1, \tag{1.5}$$

where Ω_M is the total pressureless matter density (baryonic and nonbaryonic), Ω_Λ is the density of unknown component(strongly suggested the presence of exotic form of dark mass-energy).

The combined results of CMB and Type Ia supernovae was reported in Ref.[8]

$$\Omega_\Lambda = 0.71 \pm 0.11,\ \Omega_M = 0.31^{+0.13}_{-0.12}. \tag{1.6}$$

The photons of CMB have $\rho_\gamma = \frac{\pi^2}{15} T_0^4$, where $T_0 = 2.73K$ is the present temperature of CMB,

$$\Omega_\gamma = 5.1 \times 10^{-5} \tag{1.7}$$

is reported from Ref.[9]. Results from Big Bang nucleosynthesis indicate that the total baryon density is

$$\Omega_B = 0.039 \pm 0.004. \tag{1.8}$$

Stars contribute roughly 10% of this

$$\Omega_{lum} \sim 0.004. \tag{1.9}$$

Values of Ω are summarized in Fig.1.2. $\Omega_{\rm CDM}$ and Ω_ν are described later.

1.3 Local dark matter density

The local dark matter density, ρ_D and the velocity dispersion of dark matter particles, $\bar{v} = < \vec{v}^2 >^{1/2}$ are crucial to both the direct and indirect methods of dark matter detection. In determining ρ_D and $\bar{v}$, the rotation curve is the most important observational quantity since it measures the change in density and sets the scale for the depth of the Galactic potential well. The rotation curve of the Milky Way has been measured repeatedly, but due to our unfortunate location inside the Galaxy, the errors are larger than those for external galaxies. The IAU standard value for the rotation velocity at the Sun's distance from the Galactic center is about 220km/s. Flores argues for ρ_D in the range 0.3 - 0.43 GeV cm^{-3}[10]. In this thesis, it is adopted that,

$$\rho_D = 0.3\ \text{GeVcm}^{-3} \tag{1.10}$$

for compare the results easily to the other experiments.

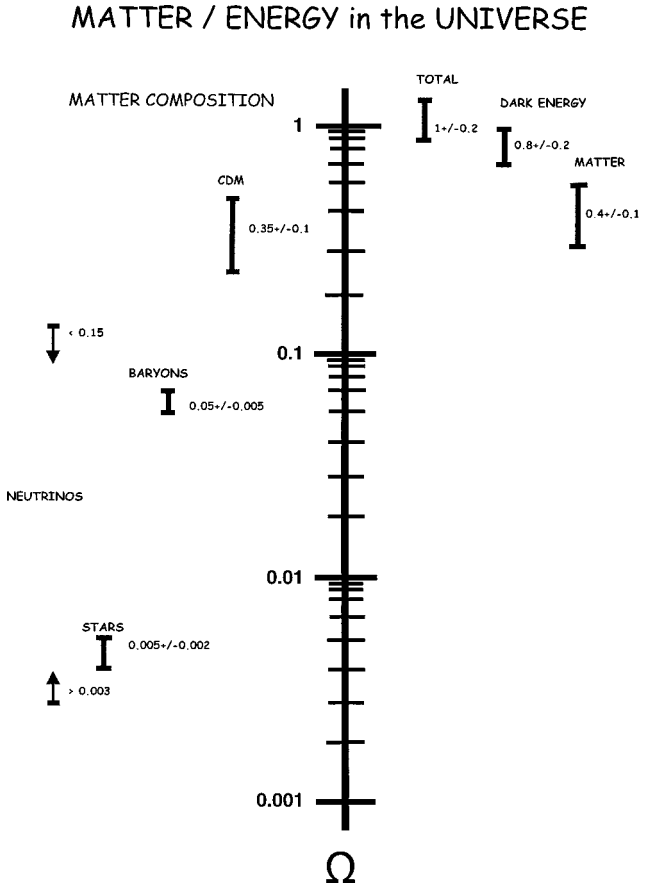

Figure 1.2: Summary of matter/energy in the Universe. Most recent values of Ω are described in the text. This figure is derived from Ref. [1].

1.4 Dark matter candidates

The type of dark matter is classified as baryonic or nonbaryonic matter. In this section, these searches are described.

1.4.1 Searches for baryonic dark matter

Baryonic matter can exist in the halos of galaxies in the form of remnants, for example white dwarfs, neutron starts, black holes, of an early generation of massive stars. These MAssive Compact Halo Objects are searched by gravitational lensing effects by some groups, MACHO, EROS and OGLE. Millions of stars in the Large Magellanic Cloud (LMC) and the Small Magellanic Cloud (SMC) are monitored by them, and when a MACHO passes directly between earth and star, the MACHO acts a gravitational lens and magnifies the source star. A combined results from EROS and MACHO [2] excluded the masses from 10^{-7} to 10^{-1} region, and the result from MACHO [11] indicated that MACHOs with masses of $\sim 0.5\ M_{\odot}$ comprise ~ 20 % of total mass of the halo. But such objects should be shine, so this situation is not understood clearly at now.

1.4.2 Searches for nonbaryonic dark matter

The nonbaryonic dark matter is classified as “hot” or “cold” depending on whether it is relativistic or nonrelativistic.

Hot dark matter

Neutrino Neutrino could be a significant component of dark matter if their masses are in the approximate range 1 - 50 eV. $m_\nu \geq 20$ eV would mean that neutrinos are dominant. However, tritium decay sets an effective mass limit of 2.8 eV [12].

The neutrino experiments, Super Kamiokande (Super-K) and SNO indicate that neutrino mass exists. A squared mass difference from atmospheric neutrino oscillation analysis by Super-K [13] is in the range of 10^{-3} eV^2.

This difference, together with the tritium decay result, limits the sum of the mass eigenvalues of active neutrinos to be between 0.05 and 8.4 eV, so that

$$0.001 \leq \Omega_\nu \leq 0.18 \tag{1.11}$$

for the neutrino contribution to the critical density.

Cold dark matter

The two best known and most studied cold dark matter candidates are the lightest supersynmmetric particle (LSP) and the axion.

Axion Axion is predicted by extensions of the Standard Model which resolve the strong *CP* problem. Axion in the mass range of 10^{-5} eV $\leq m \leq 10^{-2}$ eV are viable dark matter candidates. Axion couple to two photons via intermediate quark states and could be detected by interaction with a magnetic field that produces a faint microwave radiation detectable in a tunable cavity. Two new experiments, US halo axion detector [14] and Kyoto CARRACK [15] will explore to reach the required sensitivity for parts of the mass range, or can do so with further upgrades.

WIMP The neutralino is linear combinations of the superpartners of the photon, the Z^0, and two neutral Higgs bosons. It is called Weakly Interacting Massive Particle (WIMP) and described later in detail.

Chapter 2

WIMP search

WIMPs interact with normal matter by elastic scattering from nuclei. The energy deposited by the resulting recoil nuclei has a characteristic exponential spectrum (See Chapter 3).

2.1 MSSM and neutralino

The Minimal Supersymmetric extension of the Standard Model (MSSM) contains all the known fields of the standard model and an extra Higgs multiplets. The interactions of the theory are all those which are allowed by the gauge symmetry SU(3) $\times$ SU(2) $\times$ SU(1). The MSSM possesses a multiplicative R parity invariance,

$$R = (-1)^{3(B-L)+2S}, \tag{2.1}$$

where B, L are the baryon and lepton number operators and S is the spin. This means that $R = 1$ for ordinary particles and $R = -1$ for their superpartners.

In supersymmetry, there is a fermionic (bosonic) degree of freedom for every bosonic (fermionic) degree of freedom, so the particle is greatly extended in the MSSM (Table 2.1). The lightest supersymmetric particle (LSP) is stable by the invariance of R parity, so it can be WIMP.

MSSM predicts four neutral, massive Majorana fermions; these masseigenstates are linear combinations of the superpartners of the photon (photino($\tilde{\gamma}$)), the Z^0 boson (zino$\tilde{Z}$), and two neutral Higgs bosons (higgsinos($\tilde{H_1}$, $\tilde{H_2}$)). They are called neutralinos(χ).

$$\chi = N_1\tilde{B} + N_2\tilde{W}^3 + N_3\tilde{H}_1^0 + N_4\tilde{H}_2^0, \tag{2.2}$$

where $\tilde{B}$ and $\tilde{W}^3$ are the supersymmetric partners of the U(1) gauge field B and the third component of the SU(2) gauge field W^3 that mix to make the photon and Z^0 boson.

A useful parameter for describing the neutralino composition is the gaugino fraction,

$$f_g = |N_1|^2 + |N_2|^2, \tag{2.3}$$

if $f_g > 0.5$, then neutralino is primarily gaugino and $f_g < 0.5$, the neutralino is primarily higgsino.

Normal particles		SUSY partners	
Symbol	Name	Symbol	Name
$q = u, c, t$	up quarks	$\tilde{q}_u^1, \ldots, \tilde{q}_u^6$	up squarks
$q = d, s, b$	down quarks	$\tilde{q}_d^1, \ldots, \tilde{q}_d^6$	down squarks
$l = e, \mu, \tau$	leptons	$\tilde{l}_1, \ldots, \tilde{l}_6$	sleptons
ν	neutrinos	$\tilde{\nu}_1, \ldots, \tilde{\nu}_3$	sneutrinos
g	gluons	$\tilde{g}$	gluinos
$W^{\pm}$	W boson	$\tilde{\chi}_1^{\pm}, \tilde{\chi}_2^{\pm}$	charginos
$H^{\pm}$	charged Higgs		
γ	photon		
Z^0	Z boson		
h^0 (H_2^0)	light scalar Higgs	$\tilde{\chi}_1^0, \ldots, \tilde{\chi}_4^0$	neutralinos
H^0 (H_1^0)	heavy scalar Higgs		
A^0 (H_3^0, P_0)	pseudoscalar Higgs		

Table 2.0 Particles of MSSM [18]

2.2 WIMP search by e^+e^- colliders

A search for neutralinos is performed using the data collected with the OPAL detector at the center-of-mass energies ($\sqrt{s}$) of 181-184 GeV at LEP e^+e^- collider at CERN. The lightest neutralino and next-to-lightest neutralino ($\tilde{\chi}_1^0$ and $\tilde{\chi}_2^0$, respectively) can be produced like this,

$$e^+e^- \rightarrow \tilde{\chi}_1^0\tilde{\chi}_2^0. \tag{2.4}$$

$\tilde{\chi}_2^0$ decays as followings,

$$\tilde{\chi}_2^0 \rightarrow \tilde{\chi}_1^0\gamma, \tag{2.5}$$

$$\tilde{\chi}_2^0 \rightarrow \tilde{\chi}_1^0\nu\bar{\nu},\ \tilde{\chi}_1^0 l^+l^- \text{ or } \tilde{\chi}_1^0 q\bar{q}, \tag{2.6}$$

while $\tilde{\chi}_1^0$ will always produce a considerable missing energy and missing momentum signal, $\tilde{\chi}_2^0$ give rise to a spectrum of Eq.2.5 and 2.6.

The current OPAL limit is $M_{\tilde{\chi}_1^0}$ mass > 31.6 GeV/c^2 [16].

2.3 WIMP indirect search

If WIMPs are Majorana neutralinos, pair annihilations can occur. There are numerous final states into which the neutralino can annihilate. Table 2.1 shows neutralino-neutralino annihilation channels. Fig.2.1 shows diagram contributing to neutralino annihilation to fermions.

	Annihilation channel
$\chi\chi \rightarrow$	$f\bar{f}$
	W^+W^-
	Z^0Z^0
	W^+H^-, W^-H^+
	Z^0A^0
	Z^0H^0, Z^0h^0
	A^0A^0, H^0H^0, h^0h^0, H^0h^0
	A^0H^0, A^0h^0
	H^+H^-
	gg
	$\gamma\gamma$

Table 2.1: neutralino-neutralino annihilation channels.

The most likely scenario is a search for high energy neutrino signals from the Sun, Earth, or Galactic center, where WIMP density may be sufficiently enhanced by gravitational capture. Observation of muon neutrinos provide the best hope for observing the

neutrino channel(ν-$\bar{\nu}$), since the resulting upgoing muons produced in the Earth have long range in the neutrino detector such as Super-K. A recent analysis by the Super-K to produce a WIMP-nucleon cross section limit using combined Sun, Earth and Galactic center data appears to exclude parts of the DAMA-allowed region [17].

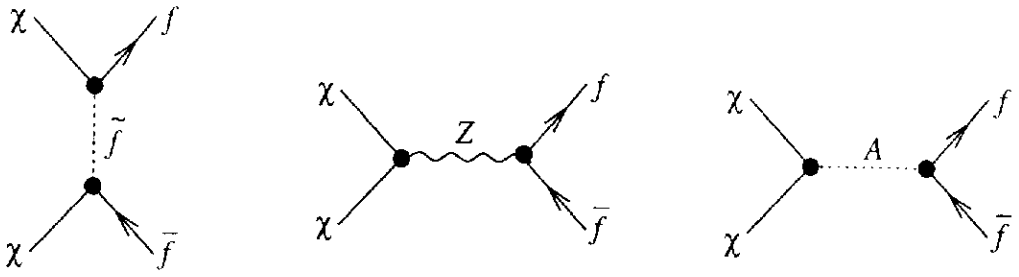

Figure 2.1: Feynman diagrams contributing to neutralino annihilation into fermions.

2.4 WIMP direct search

WIMPs interact with normal matter(target) by elastic scattering from nuclei. Fig.2.2 and Fig.2.3 show the Feynman diagrams contributing to the spin dependent and the spin independent elastic scattering of neutralinos from quarks.

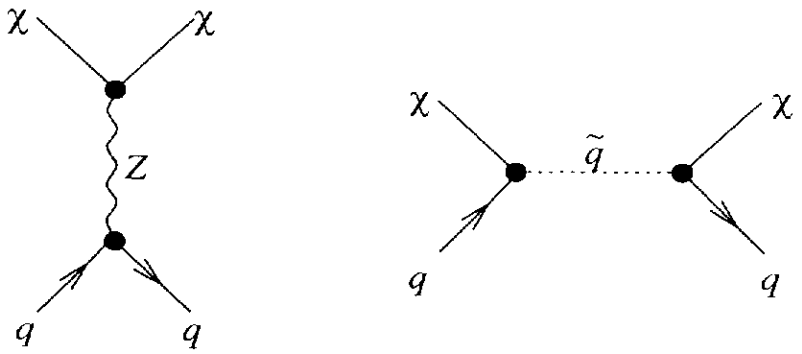

Figure 2.2: Feynman diagrams contributing to the spin independent elastic scattering of a neutralino from quarks

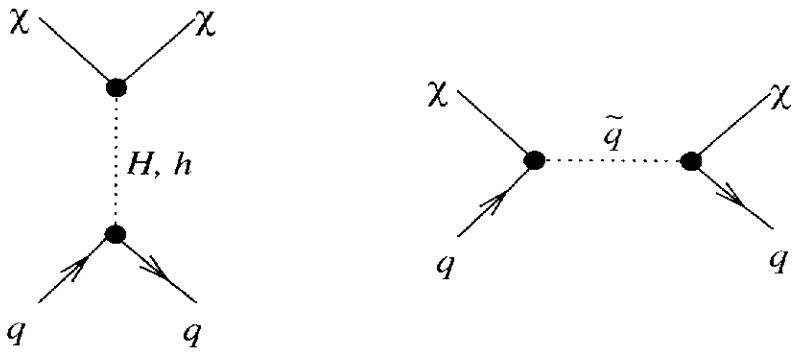

Figure 2.3: Feynman diagrams contribution to the spin dependent elastic scattering of a neutralino from quarks

It is expected that event rate would be less than $1\text{kg}^{-1}\text{day}^{-1}$ in a few keV up to a few ten keV, so low energy threshold, low background and a large mass are needed for the detector (See Chapter 3). WIMPs direct searches are under way or planned in deep underground laboratory all over the world. Present WIMPs direct searches are summarized in Table2.2.

Method	Group	Site	Target	Mass
Scintillation	DAMA[19, 20]	Gran Sasso	NaI	9×9.70 kg
			Xe	6.50 kg
			CaF	0.37 kg
	ELEGANT[21]	Oto	NaI	20× 36.5 kg
			CaF	25×0.29 kg
	UKDMC [22]	Bulby	NaI	6× 8 kg
	ZEPLIN [23]	Bulby	Xe	4 kg
	XMASS	Kamioka	Xe	100 kg
Ionization	IGEX [24]	Canfranc	Ge	2.0 kg
	HDMS [25]	Gran Sasso	Ge	2.758 kg
Bolomater	CRESST [26]	Gran Sasso	$CaWO_4$	262 g
	Tokyo	Kamioka	LiF	8×21 g
			NaF	8×22 g
Bol/Ion	EDELWEISS[27]	Frejus	Ge	3×320 g
	CDMS[28]	Shallow depth	Ge	6×165 g
Sci/Ion	XMASS	Kamioka	Xe	1 kg

Table 2.2: Present experimental activities on WIMP direct detection.

In 1998, DAMA reported an allowed region for WIMP with 100 kg NaI using annual modulation analysis in the total count rate over 4 years [29, 30]. However the technique does not separate nuclear recoils from the much larger low-energy background which could be subject to other modulating systematics.

CDMS [28]and EDELWEISS [27] excluded that region. These experiment is using Ge detector with measuring both phonon and charge signal to discriminate gamma or beta rays from nuclear recoil events. Fig. 2.4 shows these results.

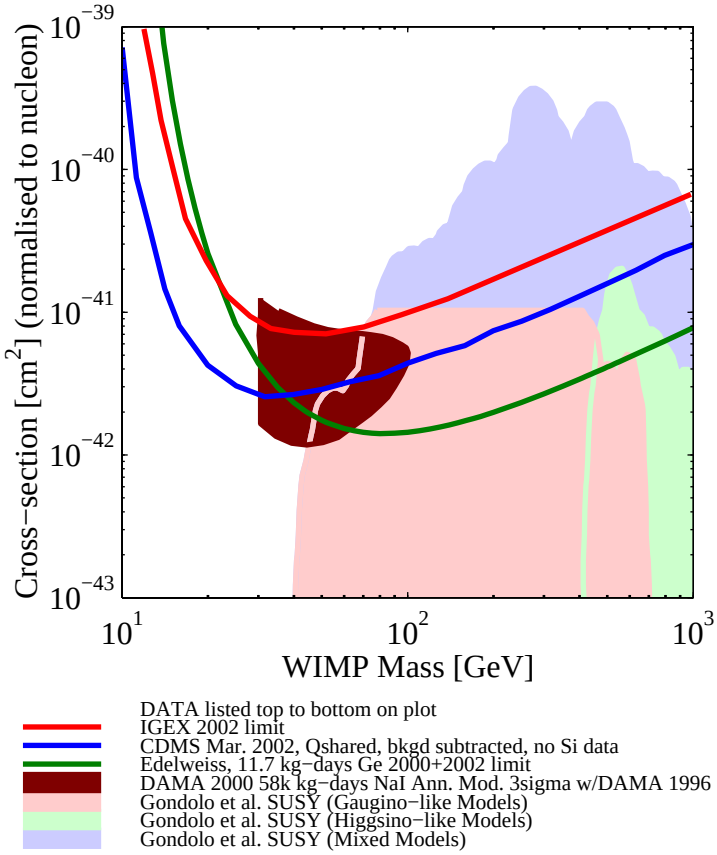

Figure 2.4: Spin independent exclusion limits. Allowed region at 3σ CL from DAMA and limits from CDMS, EDELWEISS and IGEX experiments. This figure is taken from Ref.[31].

Neutralinos can be detected also by spin dependent interaction. Results of the spin dependent interaction are shown in Fig 2.5.

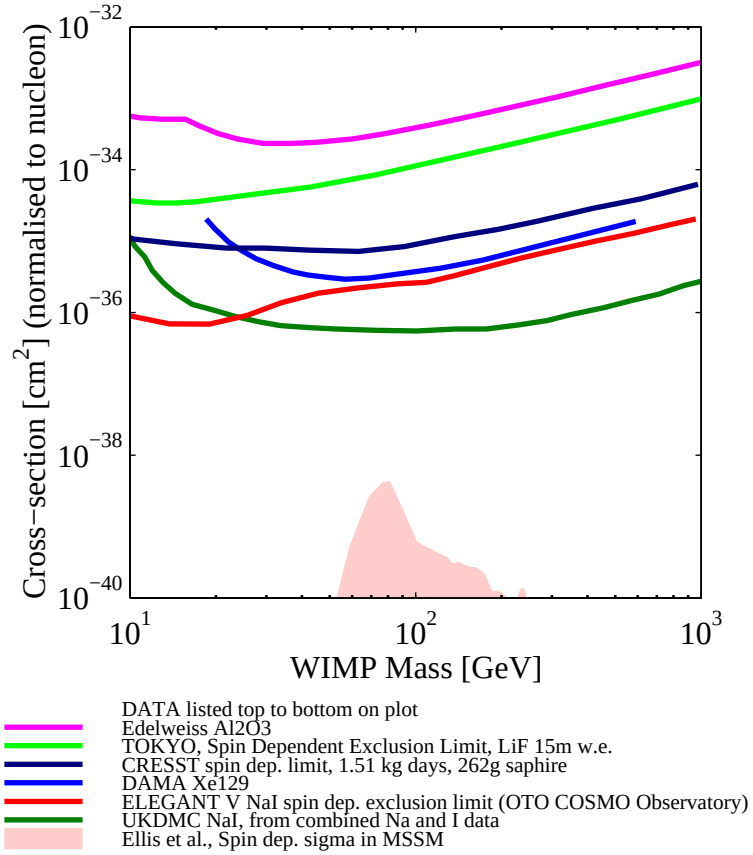

Figure 2.5: Spin dependent exclusion limits.This figure is taken from Ref.[31].

Chapter 3

Direct detection of WIMP

A number of experiments are underway or planned to investigate new heavy weakly interacting particles (WIMPs) in our Galaxy. The experiments aim to detect (or set limits on) nuclear recoils arising from collisions between WIMPs and target nuclei. In this section, the theoretical framework of the direct detection of WIMPs is described [32].

3.1 Total event rate

The particle density of dark matter particles is given by :

$$dn = \frac{n_0}{k} f(\mathbf{v}, \mathbf{v_E}) d^3\mathbf{v}, \tag{3.1}$$

where k is a normalization constant, n_0 is the mean dark matter particle number density ($= \rho_D / M_\chi$ for dark matter particle mass M_χ, density ρ_D), $\mathbf{v}$ is the dark matter velocity onto the target, $\mathbf{v_E}$ is Earth (target) velocity relative to the dark matter distribution, and $\mathbf{v}_{\rm esc}$ is the local Galactic escape velocity. A Maxwellian distribution with the velocity dispersion v_0 is assumed for dark matter velocity:

$$f(\mathbf{v}, \mathbf{v_E}) = \exp(-(\mathbf{v}+\mathbf{v_E})^2 / v_0^2) \tag{3.2}$$

for $v_{\rm esc} = \infty$,

$$k = k_0 = (\pi v_0^2)^{3/2}, \tag{3.3}$$

where the same distribution truncated at $|\mathbf{v}+\mathbf{v_E}| = v_{\rm esc}$ would give

$$k = k_1 = k_0 \left[\mathrm{erf}\left(\frac{v_{\rm esc}}{v_0}\right) - \frac{2}{\sqrt{\pi}} \frac{v_{\rm esc}}{v_0} \mathrm{e}^{-v_{\rm esc}^2 / v_0^2} \right], \tag{3.4}$$

where erf(x) = $2/\sqrt{\pi} \int_0^x \exp(-t^2)$.
The event rate per unit mass on a target of atomic mass A AMU, with cross section per nucleus for zero momentum transfer σ_0 is

$$dR = \frac{N_0}{A} \sigma_0 v dn, \tag{3.5}$$

where N_0 is the Avogadro number (6.02×10^{26} kg^{-1}), v is the dark matter velocity. From Eq.(3.1) and Eq.(3.5), total event rate R is then

$$R = \frac{N_0}{A}\sigma_0 \int v dn = \frac{N_0}{A}\sigma_0 n_0 \langle v \rangle. \tag{3.6}$$

Here, $\langle v \rangle$ is the mean dark matter velocity. The total event rate R_0 for $v_E = 0$ and $v_{\rm esc} = \infty$ is expressed as

$$R_0 = \frac{N_0}{A}\sigma_0 n_0 \frac{2v_0}{\sqrt{\pi}} \tag{3.7}$$

for $v_E \neq 0$ and $v_{\rm esc} \neq 0$, using (3.3), (3.6) and (3.7)

$$R = R_0 \frac{\sqrt{\pi}}{2}\frac{\langle v \rangle}{v_0} = R_0 \frac{k_0}{k}\frac{1}{2\pi v_0^4}\int v f(\mathbf{v}, \mathbf{v_E}) d^3\mathbf{v} \tag{3.8}$$

R_0 is conventionally expressed in units kg^{-1}d^{-1}. Normalized to ρ_D = 0.3 GeVc^{-2}cm^{-3} and v_0 = 230km s^{-1}, (3.7) is written as:

$$R_0 = \frac{377}{M_\chi M_{\rm N}}\left(\frac{\sigma_0}{1{\rm pb}}\right)\left(\frac{\rho_D}{0.3{\rm GeVc^{-2}cm^{-3}}}\right)\left(\frac{v_0}{230{\rm km\ s^{-1}}}\right)\ {\rm kg\ d^{-1}} \tag{3.9}$$

with $M_\chi, M_{\rm N}$ in GeV c^{-2},where $M_{\rm N}$ is the mass of target nucleus ($M_{\rm N}$ = 0.932 A).

3.2 Differential rate

The recoil energy of a nucleus struck (E_R) by a dark matter particle of kinetic energy $E(=\frac{1}{2}M_\chi v^2)$ scattered at angle θ in center of mass is:

$$E_R = Er(1-\cos\theta)/2, \tag{3.10}$$

$$r = \frac{4M_\chi M_{\rm N}}{(M_\chi + M_{\rm N})^2}, \tag{3.11}$$

It is assumed that the scattering is isotropic, so that recoils are uniformly distributed in E_R, over the range $0 \leq E_R \leq Er$,

$$\frac{dR}{dE_R} = \int_{E_{min}}^{E_{max}} \frac{1}{Er} dR(E) = \frac{1}{E_0 r}\int_{v_{min}}^{v_{max}} \frac{v_0^2}{v^2} dR(v), \tag{3.12}$$

where $E_{min}(E_{max})$ is the smallest (biggest) particle energy which can give a recoil energy and v_{min} (v_{max}) is the dark matter particle velocity corresponding to E_{min} (E_{max}),

$$E_{min} = E_R/r\ ,\ v_{min} = (2E_{min}/M_\chi)^{1/2} = (E_R/E_0 r)^{1/2} v_0.$$

The differential form of (3.8) is

$$dR = R_0 \frac{k_0}{k}\frac{1}{2\pi v_0^4} v f(\mathbf{v}, \mathbf{v_E}) d^3 v, \tag{3.13}$$

using Eq.(3.12) and Eq.(3.13)

$$\frac{dR}{dE_R} = \frac{R_0}{E_0 r}\frac{k_0}{k}\frac{1}{2\pi v_0}\int_{v_{min}}^{v_{max}}\frac{1}{v}f(\mathbf{v},\mathbf{v_E})d^3\mathbf{v}, \tag{3.14}$$

Hence, from Eq.(3.14), the nuclear recoil spectrum for v_E = 0 is written as

$$\frac{dR(0,\infty)}{dE_R} = \frac{R_0}{E_0 r}\mathrm{e}^{-E_R/E_0 r}, \tag{3.15}$$

With non zero v_E and finite v_{esc}, (3.14) gives

$$\begin{aligned}
\frac{dR(0,v_{\mathrm{esc}})}{dE_R} &= \frac{k_0}{k_1}\frac{R_0}{E_0 r}(\mathrm{e}^{-E_R/E_0 r} - \mathrm{e}^{-v_{\mathrm{esc}}^2/v_0^2}) \\
&= \frac{k_0}{k_1}\left[\frac{dR(0,\infty)}{dE_R} - \frac{R_0}{E_0 r}\mathrm{e}^{-{v_{\mathrm{esc}}}^2/v_0^2}\right], && (3.16)\\
\frac{dR(v_E,\infty)}{dE_R} &= \frac{R_0}{E_0 r}\frac{\sqrt{\pi}}{4}\frac{v_0}{v_E}\left[\mathrm{erf}\left(\frac{v_{min}+v_E}{v_0}\right) - \mathrm{erf}\left(\frac{v_{min}-v_E}{v_0}\right)\right] && (3.17)\\
&\sim c_1\frac{R_0}{E_0 r}\mathrm{e}^{-c_2 E_R/E_0 r}, && (3.18)\\
\frac{dR(v_E,v_{\mathrm{esc}})}{dE_R} &= \frac{k_0}{k_1}\left[\frac{dR(v_E,\infty)}{dE_R} - \frac{R_0}{E_0 r}\mathrm{e}^{-v_{\mathrm{esc}}^2/v_0 2}\right], && (3.19)
\end{aligned}$$

where c_1, c_2 are fitting constants. Values of c_1, c_2 for different months are $c_1 = 0.738, c_2 = 0.540$ in June, $c_1 = 0.771, c_2 = 0.592$ in December, $c_1 = 0.751, c_2 = 0.561$ in average through the year [32].

3.3 Elastic scattering cross section

The WIMP-nucleus elastic scattering cross section depends on the WIMP-quark interaction strength. The total WIMP-nucleus cross section σ_0 at zero momentum transfer can be written as [18]

$$\sigma_0 = 4G_F^2\mu_{\mathrm{N}}^2 C_{\mathrm{N}}, \tag{3.20}$$

where the WIMP-target reduced mass μ_{N} is given by $M_\chi M_{\mathrm{N}}/(M_\chi + M_{\mathrm{N}})$ for WIMP mass M_χ and target nucleus mass M_{N}, the Fermi coupling constant $G_F/(\hbar c)^3$ = 1.166 GeV^{-2} with $\hbar c$ = 0.197 GeV fm and C_{N} is a dimensionless number that carries all the particle -physics model information. It is conventional to normalize to WIMP-nucleus cross section when comparing results from different experiments which use different target materials. The WIMP-proton cross section $\sigma_{\chi-p}$ is written as

$$\sigma_{\chi-p} = \sigma_0\frac{\mu_p^2}{\mu_{\mathrm{N}}^2}\frac{C_p}{C_{\mathrm{N}}}, \tag{3.21}$$

where μ_p is the reduced mass which is expressed above and $C_{\rm p}$ is the enhancement factor for proton.
In this section, the cross section for the coherent (spin independent) $\sigma^{\rm SI}$ and the axial vector (spin dependent) $\sigma^{\rm SD}$ interaction are described.

3.3.1 Spin independent interaction

In the spin independent (SI) case, $C_{\rm N}$ is expressed as [36]

$$C_{\rm N} = \frac{1}{\pi G_F^2}\left[Z f_p + (A-Z) f_n\right]^2, \tag{3.22}$$

where f_p and f_n are the effective WIMP couplings to protons and neutrons, respectively which are determined by the information of quark mass ratio and chiral symmetry applied to baryons. For Majorana WIMPs $f_p \simeq f_n$, one typically has

$$\frac{C_{\rm N}}{C_p} \simeq \frac{C_{\rm N}}{C_n} \simeq A^2 \tag{3.23}$$

and from Eq.(3.21) and Eq.(3.23)

$$\sigma^{SI}_{\chi-{\rm p}} = \sigma_0 \frac{\mu_p^2}{\mu_{\rm N}^2}\frac{1}{A^2}. \tag{3.24}$$

For massive Dirac neutrino-like WIMPs $f_p \simeq 0$

$$\frac{C_{\rm N}}{C_{\rm p}} \simeq \frac{C_{\rm N}}{C_n} \simeq (A-Z)^2. \tag{3.25}$$

3.3.2 Spin dependent interaction

In the spin dependent case(SD), $C_{\rm N}$ is expressed as [36]

$$C_T = \frac{8}{\pi}\lambda^2 J(J+1), \tag{3.26}$$

where

$$\lambda \equiv \frac{1}{J}(a_p\langle S_p\rangle + a_n\langle S_n\rangle), \tag{3.27}$$

a_p and a_n are effective WIMP-proton and WIMP-neutron couplings and $\langle S_{p,n}\rangle = \langle N \mid S_{p,n} \mid N\rangle$ are the expectation values of the proton and neutron spins within the nucleus and J is the total nuclear spin. The full expressed a_p, a_n are reported in [18, 37]. In the case of the WIMP-nucleon interaction mediated by Z-exchange one has [38]

$$\frac{a_n}{a_p} = \left(\sum_{q=u,d,s} T_{3q}\Delta q\right)_n \Big/ \left(\sum_{q=u,d,s} T_{3q}\Delta q\right)_p, \tag{3.28}$$

where T_{3q} denotes the third component of the quark weak isospin, Δq are the fractional spin carried by the quark q in the appropriate nucleon. Then, from Eq.(3.21), Eq.(3.26) and Eq.(3.28)

$$\sigma^{SI}_{\chi-p} = \sigma_0 \frac{\mu_p^2}{\mu_{\rm N}^2} \frac{(\lambda^2_{p,Z} J(J+1))^{\rm proton}}{(\lambda^2_{N,Z} J(J+1))^{\rm Nuclear}} \tag{3.29}$$

$$= \sigma_0 \frac{\mu_p^2}{\mu_{\rm N}^2} \frac{0.75}{(\lambda^2_{N,Z} J(J+1))^{\rm Nuclear}} \tag{3.30}$$

From Eq.(3.30), under the assumption of a pure Z exchange , allows us the conversion of any experimental upper limit into upper bound on σ^{proton}_{SD}, in the same way as for the spin independent case. Table 3.1 shows $\lambda^2_{p,Z} J(J+1)$ values on various targets. The value of Δq are from Ref.[35]

$$\Delta u = 0.83 \pm 0.03, \quad \Delta d = -0.43 \pm 0.03, \quad \Delta s = -0.10 \pm 0.03 \tag{3.31}$$

These values are for quarks in proton. In case of neutron the isospin symmetry substitutions are needed,

$$\Delta u \to \Delta d, \quad \Delta d \to \Delta u. \tag{3.32}$$

a_n/a_p is calculated using these value,

$$a_n/a_p = -0.853. \tag{3.33}$$

Nucleus	J	Odd Nucleon	$\langle S_p \rangle$	$\langle S_n \rangle$	$\lambda^2_{p,Z} J(J+1)$
^{7}Li	3/2	p	0.497	0.004	0.406
^{19}F	1/2	p	0.441	-0.109	0.855
^{23}Na	3/2	p	0.248	0.020	0.089
^{73}Ge	9/2	n	0.009	0.372	0.105
^{125}Te	1/2	n	0.001	0.287	0.178
^{127}I	5/2	n	0.309	0.075	0.084
^{129}Xe	1/2	n	0.028	0.359	0.232
^{131}Xe	3/2	n	-0.009	-0.227	0.057

Table 3.1: Values of $\langle S_p \rangle$, $\langle S_n \rangle$ $\lambda^2_{p,Z} J(J+1)$ for various nuclei. Values for Li, F are taken from Ref.[39], for Na, Te, I, Xe are taken from Ref.[34], for Ge is taken from Ref.[40].

3.4 Nuclear form factor correction

When the moment transfer $q = (2M_{\mathrm{N}}E_R)^{1/2}$ is such that the wavelength h/q is no longer large compared to the nuclear radius, the effective cross section begins to fall with increasing q, even in the case of spindependent scattering which effectively involves a single nucleon. Here h is the Planck constant. It is adequate to represent this by 'Form Factor', F, which is a function of the dimensionless quantity qr_n where r_n is an effective nuclear radius.

$$q = (2M_{\mathrm{N}}E_R)^{1/2}/\ \hbar. \qquad (\hbar c \equiv 197.3 \text{ MeV fm}) \tag{3.34}$$

Cross section then behave as:

$$\sigma(qr_n) = \sigma_0 F^2(qr_n), \tag{3.35}$$

where σ_0 is the cross section at zero momentum transfer. For the spin independent case, the form factor is written as:

$$\begin{aligned} F^2(E_R) &= \left[\frac{3j_1(qr_n)}{qr_n}\right]^2 \exp[-(qs)^2] \\ &= \left(\frac{3\,[\sin(qr_n) - qr_n\cos(qr_n)]}{(qr_n)^3}\right)^2 \exp[-(qs)^2], \end{aligned} \tag{3.36}$$

where $\mathrm{j}_1(\mathrm{qr}_n)$ is the spherical Bessel function of index 1, s $\simeq$ 1 fm is the thickness parameter for the nuclear surface, $r_n = (R^2 - 5s^2)^{1/2}$ and $R = 1.2A^{1/3}$ fm [33].
For the spin dependent case,

$$F(q)^2 = \frac{S(q)}{S(0)}, \tag{3.37}$$

$$S(q) = a_0^2 S_{00}(q) + a_1^2 S_{11}(q) + a_0 a_1 S_{01}(q).$$

$a_0 = a_p + a_n$ and $a_1 = a_p - a_n$ are the isoscalar and isovector coefficients. The most recent nuclear physics calculations for the spin structure function S(q) [34] was used in our analysis, the ratio a_n/a_p is -0.853 using for the $\triangle q$'s estimates of [35]. Fig3.1, 3.2 shows the value of form factor as a function of recoil energy for spin independent and spin dependent case. Fig3.1 and Fig3.2 show Form Factor ($F(q)^2$) as a function of recoil energy in the spin independent case and the spin dependent respectively.

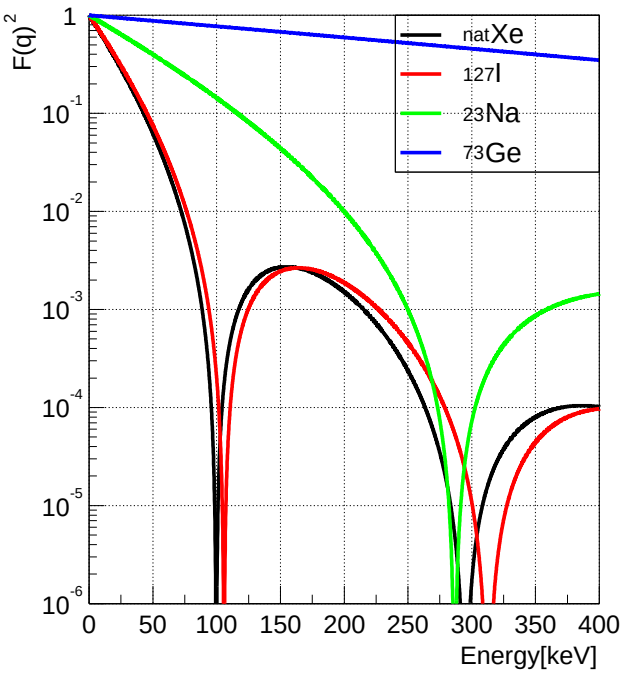

Figure 3.1: Nuclear Form factor as a function of recoil energy for spin independent case in various targets.

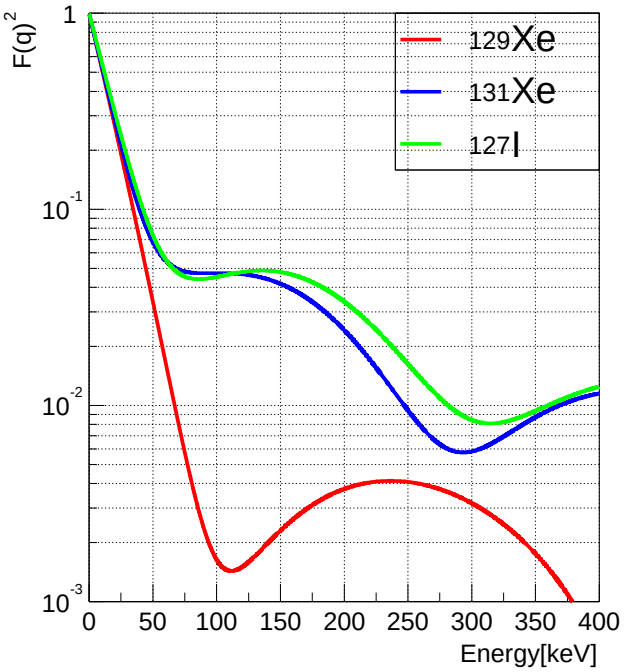

Figure 3.2: Nuclear Form factor as a function of recoil energy for spin dependent case in various targets.

3.5 Quenching factor

For scintillation and ionization detectors are calibrated with gamma sources, but the response of nuclear recoil is different from an electron recoil. The ratio f_Q of an electron recoil to a nuclear recoil is determined by neutron measurement. This is called quenching factor,

$$f_Q = \frac{E_R}{E_v}, \tag{3.38}$$

where E_R is the observed energy for a nuclear recoil as mentioned above and E_v is for an electron recoil of the same energy as the nuclear recoil. Consequently, E_R in the above rates and spectra should be replaced by the 'visible' energy E_v using $E_v = E_R/f_Q$. The quenching factors for various detectors are listed in Table3.2.

Detector	Nucleus	f_Q
Xe	Xe	0.2 [43]
		0.22±0.01[44]
		0.45±0.12[20]
NaI(Tl)[41]	Na	0.3
	I	0.09
CaF(Eu)[42]	Ca	0.08
	F	0.12
Ge[45]	Ge	0.25
Si[46]	Si	0.30

Table 3.2: The quenching factors for various detectors.

Quenching factor for LXe is described in detail in 4.6.

3.6 Expected spectrum

From various factors discussed above, we can calculate the expected spectrum. The parameters for this spectrum are listed in Table7.1. Fig3.3 and Fig3.4 are the expected spectrum in the SI and SD case respectively. In this estimation, WIMP mass 50GeV and 100GeV are used.

$\sigma^{SI}_{\chi-p}$	1.0×10^{-5}pb
$\sigma^{SD}_{\chi-p}$	1.0×10^{-1}pb
Dark Matter density ρ_D	0.3 GeV/c^{-2}
Dispersion of Dark Matter velocity v_0	220km/s
Earth(Target) velocity v_E	232km/s
Local Galactic escape velocityv_{esc}	650km/s
Quenching Factor	0.263[see Sec.7.2]

Table 3.3: Astrophysical and nuclear parameters used to calculate the spectrum.

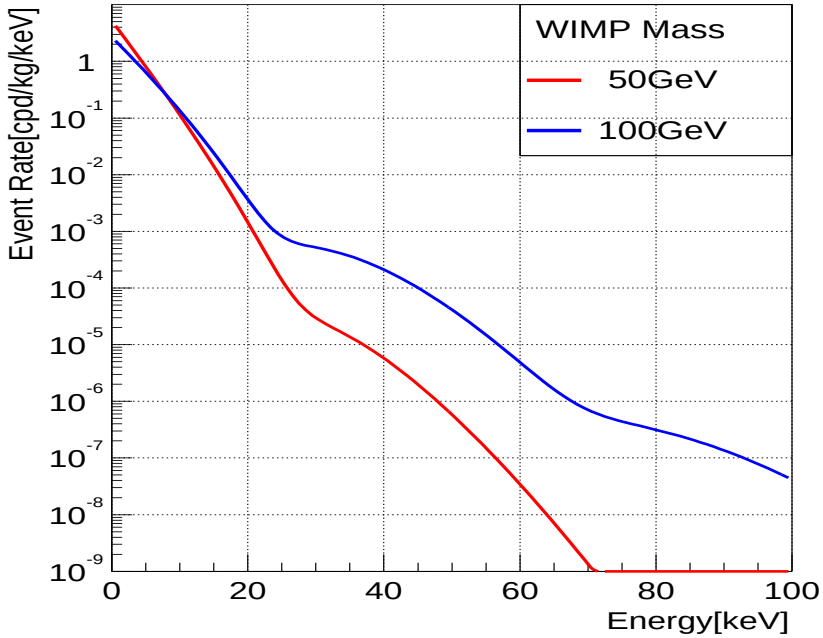

Figure 3.3: Spin Independent case: natural Xe, $\sigma_p = 1.0 \times 10^{-5}$ pb was assumed.

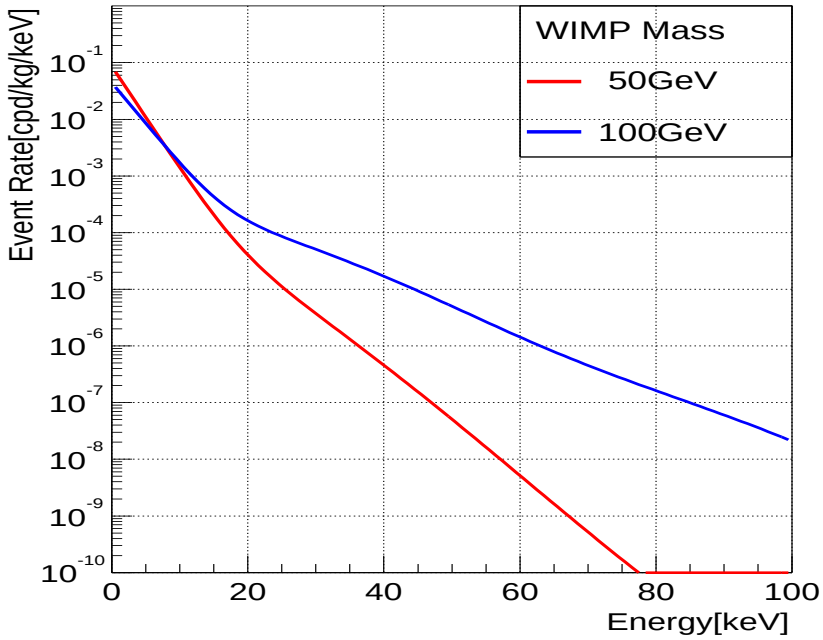

Figure 3.4: Spin Dependent case: natural Xe, $\sigma_p = 1.0 \times 10^{-1}$ pb was assumed.

3.7 Annual modulation

The annual modulation of the WIMP rate on a target detector is induced by the Earth's motion around the Sun[47]. The expected nuclear recoil energy spectrum depends on the WIMP velocity distribution and on the Earth's velocity in the galactic frame, $v_r(t)$. It varies along the year due to the expression,

$$v_E(t) = V_{sun} + V_{earth}\cos\gamma\cos\omega(t-t_0), \tag{3.39}$$

where V_{sun} = 232 km/s is the Sun's velocity with respect to the halo, V_{earth} = 30 km/s is the Earth's orbital velocity around the Sun on a plane with inclination $\gamma = 60^\circ$ respect to the galactic one, $\omega = 2\pi/T$ with T = 1 year and $t_0 \simeq$ 2nd June. Fig.3.5 illustrates the motion of the Earth relative to the Galactic coordinates. The annual modulation signature is the one of the most strong evidence of WIMPs, but the total event variation is only $\sim$ 3 %, a large mass detector is needed for statistics.

Fig.3.6 shows the expected spectrum in Jun 2nd, Dec 4th and their rate difference. In this calculation, the following value were used.

- Cross section to WIMP for SI case is 1.0×10^{-5}pb.
- WIMP mass is 50 GeV.
- V_E in Jun 2nd is 247 km/s.
- V_E in Dec 4th is 217 km/s.

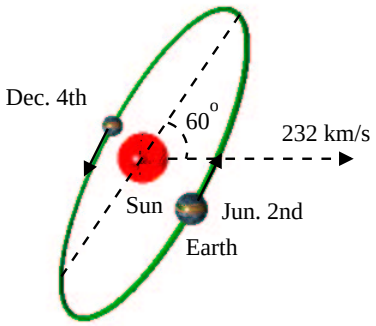

Figure 3.5: The motion of the Earth relative to the Galactic coordinates.

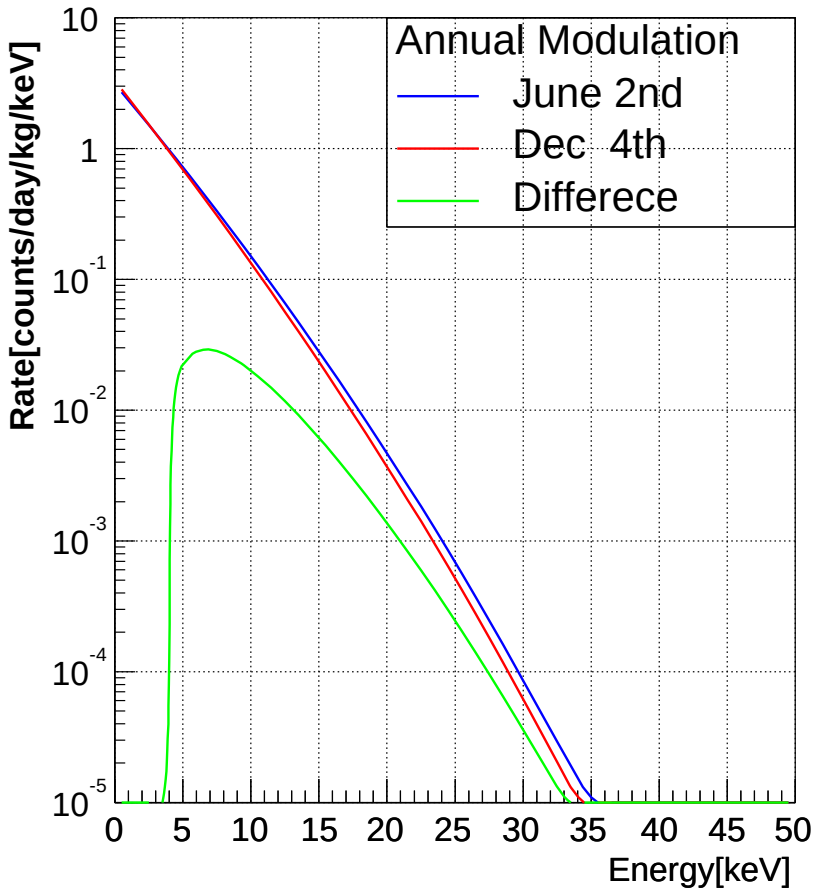

Figure 3.6: Expected energy spectrum for M = 50 GeV in Jun 2nd, Dec 4th and their difference. The parameters are listed in Table 7.1. V_Es are calculated by using Eq.3.39.

Chapter 4

Liq.Xe detector

Since the end of 1970, many new devices based on rare gas liquids have been proposed in the fields of elementary particles and astrophysics experiments. In this chapter, LXe's property is described.

4.1 Why xenon?

Until now, as mentioned in Chapter2, the following detectors have been good showing for the result of the WIMP direct search,

- Large scintillator (NaI(Tl)),
- Strong background rejection by using two signal (Ge).

Considering the above situation, the next generation search will need

- a low energy threshold (the event rate reduce exponentially),
  $\rightarrow$ high light yield, good photo-coverage, high quantum efficiency PMT. PMT is famous for a low noise device.
- strong background rejection technique,
  $\rightarrow$ using two kinds of signals, self shielding[75].
- large mass for the statistics and annual modulation.
  $\rightarrow$ inorganic scintillators are suitable for handling and costs. For the LXe detector, to design the cryogenics is easier than bolometer, because the operating temperature is 165K, while the bolometric detector is $\sim$ mK.

We have recognized the Xenon detector will satisfy all item the above.
In this chapter, the property of LXe is introduced.

4.2 Physical properties of LXe

The Liquid Xe (LXe) is expected to be an excellent detector medium for gamma rays because of its fast response, high scintillation yield, large atomic number, and high density. The summary of LXe property is listed in Table 4.1.

Atomic Number	54
Mass Number	131.29
Density	3.06g/cm^3
Boiling point	165K
Melting point	161K
Radiation length	27.7mm
Scintillation wave length	178nm
Refractive Index	1.61[48]
Energy per scintillation photon	21.6$\pm$2.8eV [49]
Decay time(recombination)	45ns
Decay time(Fast Components)	4.2ns
Decay time(Slow Components)	22ns
Scintillation absorption length	$\geq$ 100cm
Rayleigh scattering length	29cm [52]
	30cm (calculated)[53]

Table 4.1: Physical properties of Liq.Xe

Fig.4.1 shows the phase diagram of Xe. The LXe detectors are usually operated in 170-185 K using the refrigerator or liquid Nitrogen. Fig.4.2 shows the gamma cross section for Xe. Because of its high atomic number, the LXe detector is favorable to the gamma ray detector. Table4.2 shows the natural abundance of Xe. As mentioned in Section3.3, ^{129}Xe and ^{131}Xe are very interesting isotopes in spin dependent case because of their cross section to WIMP. Furthermore, ^{136}Xe can be used in the double beta decay experiment. The isotope separation is possible by centrifugal separation.

Isotope	^{124}Xe	^{126}Xe	^{128}Xe	^{129}Xe	^{130}Xe	^{131}Xe	^{132}Xe	^{134}Xe	^{136}Xe
Abn.[%]	0.10	0.09	1.92	26.4	4.07	21.2	26.9	10.4	8.87

Table 4.2: Natural abundance of Xe.

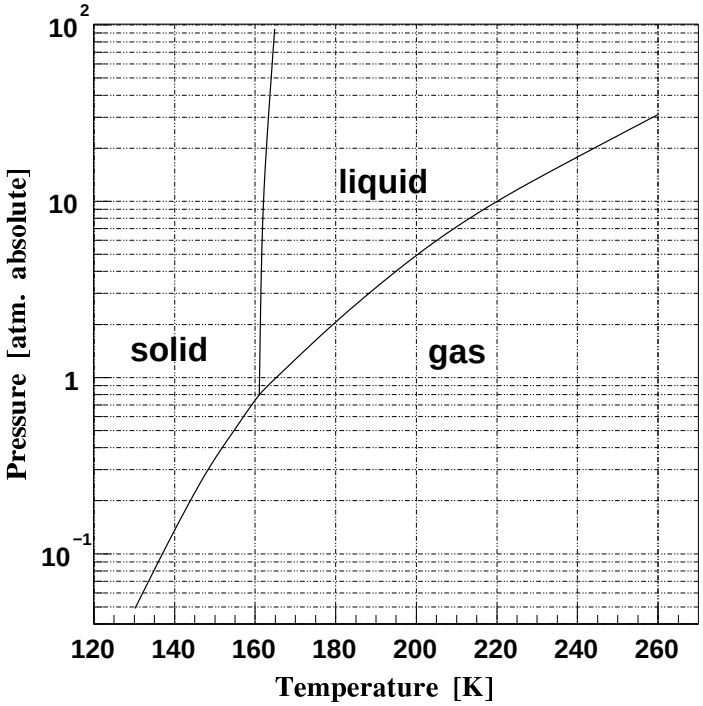

Figure 4.1: Phase diagram of Xe.

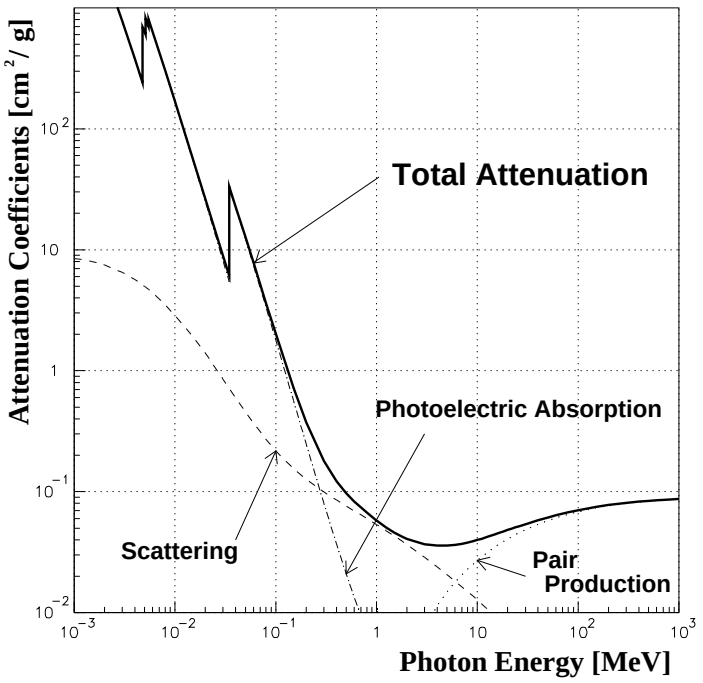

Figure 4.2: Photon cross section for Xe.

4.3 Ionization

In the design of LXe detector which is operated in the ionization mode it is necessary to know the mean number of ion pairs (= W-value) produced in the liquid by the ionizing radiation. In the middle of 1970, W-values in liquid rare gases were measured by using the electron pulse method and energetic conversion electrons as ionizing radiation[58, 59]. W-values in LAr and LXe obtained by this method are shown in Table 4.3.

Liquid	I[eV]	W_{gas}[eV]	E_g[eV]	$W_{liq}[eV]$
Ar	15.76	26.4	14.3	23.6±0.3
Xe	12.13	21.9	9.28	15.6±0.3

Table 4.3: The W values in the gas and liquid phases of argon and xenon.

4.4 Electron drift velocity and diffusion

The drift velocity of electrons determines the time response of detectors and the diffusion of electrons in the detector gives the limit of the accuracy of position determination.

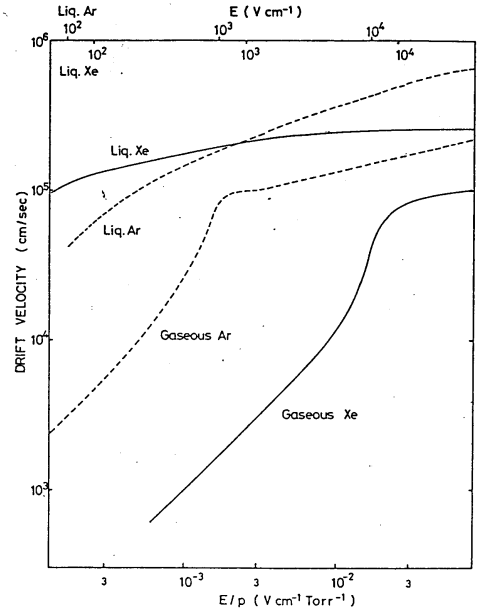

Figure 4.3: Drift velocity of electrons in LXe. For purpose of comparison, that of electrons in LAr, gaseous argon and xenon are also shown. This figure is derived from [55].

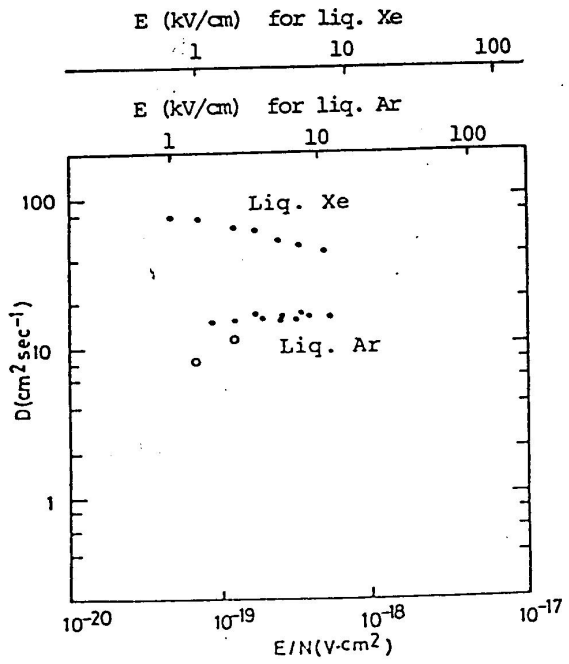

Figure 4.4: Field dependence of the diffusion coefficients of electrons. This figure is derived from [55].

Fig.4.3 shows the drift velocities of electrons in LXe and LAr with the electric field, as well as in gaseous argon and xenon with densities corresponding to the liquid state [54]. Clearly seen, the drift velocity in liquid is larger than that in gas over the whole region. For this reason, LXe is suitable as detector medium of drift chambers. The cloud of electrons produced by the ionizing radiation in LXe gradually spreads during drifting by the diffusion process. Fig.4.4 shows the diffusion coefficients of the electrons in LXe and LAr with electric field strength [55, 56].

4.5 Scintillation

For comparison of the scintillation yield in LXe with that in LAr and NaI(Tl), the W_{ph}, which is the mean energy for produce one photon, is listed in Table 4.5. The scintillation light from LXe has two decay components for α particles or fission fragments due to de-excitation of singlet and triplet states of excited dimer. The decay shapes for electrons, α particles and fission fragments in LXe are shown in Fig.4.5.

The wave length spectrum of LXe shows a single peak, corresponding to 174 nm, with a width of approximately 10 nm, which is almost equal to that of scintillation from its gas state. In addition, the scintillation from LXe has two decay time constants. Excited atoms Xe^* produced by ionizing radiation from excited molecules Xe_2^* through collision with other atoms on the ground state and VUV photons are emitted in transitions from the

lowest excited molecular state of Xe_2^* to the dissociative ground state. The scintillation light from LXe is produced by the two processes summarized in the following[55]:

$$\begin{aligned} Xe^* + Xe &\rightarrow Xe_2^*, && (4.1)\\ Xe_2^* &\rightarrow 2Xe + h\nu && (4.2) \end{aligned}$$

$$\begin{aligned} Xe^+ + Xe &\rightarrow Xe_2^+, \\ Xe_2^+ + e^- &\rightarrow Xe^{**} + Xe \\ Xe^{**} &\rightarrow Xe^* + \text{heat} && (4.3)\\ Xe^* + Xe &\rightarrow Xe_2^*, && (4.4)\\ Xe_2^* &\rightarrow 2Xe + h\nu && (4.5) \end{aligned}$$

where $h\nu$ denotes the VUV photon and the process Eq.(4.3) corresponds to a non-radiative transition. In this two processes, the excited dimer R_2^*, at the lowest excited level, should be de-excited to the dissociative ground state by emitting a single VUV photon, because the energy gap between the lowest excitation level and the ground level is so large that there exists no decay channel such as non-radiative transitions.

Scintillator	LAr	LXe	NaI(Tl)
Relativistic electrons	25.1±2.5	21.6±2.8	17.2±0.4
α particles	27.5±2.8	19.6±2.0	
Relativistic heavy particles	19.5±2.0	14.7±1.5	

Table 4.4: Measurements and estimates of the average energy needed to produce a scintillation photon, W_{ph}(eV) in LXe, LAr [57]and NaI(Tl)[50, 51]

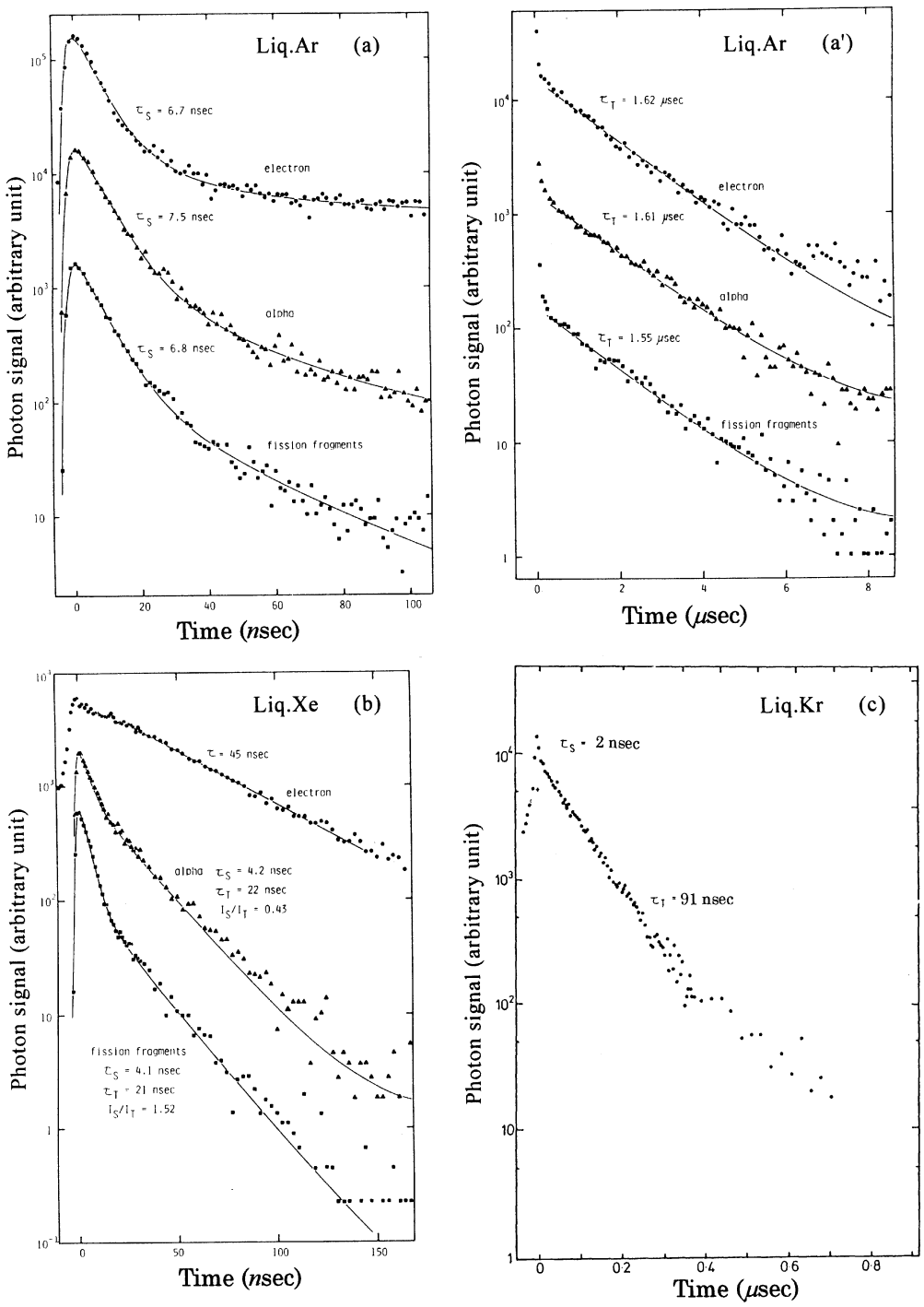

Figure 4.5: Decay curves obtained for the scintillation light from liquid Ar (a,a'), liquid Xe (b) and liquid Kr (c) excited by electrons, by α particles and fission fragments. This figure is taken from [57].

4.6 Quenching factor for liquid xenon

For the bolometric detector, the quenching factor is 1, but this values for scintillation or ionization detectors are about 0.1-0.3. This is because, when a incident particle enters a detector, the electronic and nuclear stopping take place in the detector materials. Only the electronic stopping produces the scintillation or/and the ionization and this is dominant for electron recoils and fast ions. On the other hand, this is not dominant for nuclear recoils produced by fast neutron and WIMPs. We call this effect "nuclear quenching". Semiconductors show good agreement with nuclear quenching based on the theory of Lindhard et al[60]. However, this is not the only case for liquid noble gas scintillator[61]. Hitachi explained using the electronic quenching model[62] which is taken place in the high excitation density core. This mechanism is biexcitonic collisions,

$$Xe^{*} + Xe^{*} \quad \rightarrow \quad Xe + Xe^{+} + e^{-}(K.E) \tag{4.6}$$

only one photon is produced through Eq.4.5 and e^{-} carries away and loses its energy by elastic scattering before recombination. This explanation shows good agree with the experimental data[43, 44]. When the electric field is applied in LXe, the scintillation light yield is changed. Fig5.3 shows the light yield variation in the case of electron recoil and α particles. The variation of the light yield for electron recoils in very low electric field is described in 5.4.3, in our case, the ratio of it at no electric field to at 250 V/cm is 0.76. However, in the case of non relativistic particle and nuclear recoil, its variation is negligible because of its high ionization density. If we take 0.2 for the quenching factor for LXe at no electric field, it gives 0.263 at 250 V/cm. In this experiment, this value is used in our analysis.

Chapter 5

Double phase Xe detector with PTFE reflector

The low energy threshold is very important for WIMPs direct search, to collect LXe scintillation light effectively, we tested PTFE reflector. Furthermore, a prototype double phase Xe detector with PTFE reflector for this search has been constructed and tested. Basic properties of the detector is described.

5.1 PTFE reflector

5.1.1 Reflector for LXe scintillation light

There are some difficulties to detect the scintillation light effectively, because the wavelength is in the vacuum ultra violet region. Additionally, the photon detectors such as photomultiplier (PMT) have to operate at low temperatures around 170K. The light collection efficiency of a scintillator is generally worsened because of the decrease in solid angle coverage of photon detectors in large volumes. To reduce this deterioration, one of the most practical and efficient ways is to fully surround the scintillator with a good reflector. M. Chen et al. [63] obtained a reflection coefficient in the range 85-90% by coating an aluminum mirror with MgF_2. However, it is very difficult to use such electrically conductive reflector when an electric field is applied in the LXe for the charge collection. The measurement of the Teflon® reflectance of LXe scintillation light was already reported by several groups [64, 65, 66], and the best result (82.6%) was obtained by M. Miyajima et al.. This satisfies the requirements for LXe detector. The reflectance properties of PTFE were well investigated by V.R. Weidner and J.J. Hsia [67]. Precise measurements of the reflection properties for a wide spectral range of 200-2500 nm were reported by them. The diffuse reflectance is 99% or higher over a spectral range of 350-1800 nm and slightly decreasing from 350 nm down to 200 nm. A reflectance of 95% at 174 nm, the peak of the Xe scintillation emission, is expected from a simple extrapolation. This attractive result encourages the use of PTFE in LXe.

5.1.2 Reflection coefficient of PTFE

Fig.5.1 shows the schematic view of the chamber. This chamber has wire sets to collect the charge from LXe. However, in this experiment, no electric field was applied. A 175 mm long chamber is surrounded by two PTFE walls shaped as a frustum of a cone. An anode set is placed in the middle of the chamber and two UV quartz windows with an effective diameter of 44 mm and 5mm thickness are fixed on both ends of the chamber. The optical transmission of the anode set is 97% and the inside surface of the wire frames corresponds to 3% of the PTFE surface. Nickel meshes, with 90% optical transmission were evaporated on the inner surface of the UV quartz windows as cathodes on ground potential. A nickel coated copper wire of 0.5 mm diameter, carrying a 122 keV gamma source (^{57}Co) on its tip was fixed on the PTFE wall. The source is positioned on the chamber central axis. The distance between the source and the chamber center was changed in each test. The emitted scintillation light was detected by two UV sensitive PMT (Philips XP2020Q) mounted outside the windows and coupled through 1.5 mm vacuum. The PMT output signal can be described as follows:

$$P = \frac{E}{W_{ph}} \times f \times QE \times G, \tag{5.1}$$

where P is the PMT signal, E is the energy deposited by the particle, W_{ph} is the energy to produce a scintillation photon (21.6 eV), f is the light collection efficiency at the PMT photocathode, QE is the PMT photocathode quantum efficiency and G is the gain of the PMT. One measurement was performed with a 122keV gamma ray source deposited on the tip of a wire fixed in the chamber center. The two PMTs should have equal f values since the chamber is completely symmetric with respect to its center. This means that the value for the two PMTs in Eq.5.1 are equal. Therefore, the ratio of P and f is a constant, independently of the source position, for both PMTs.

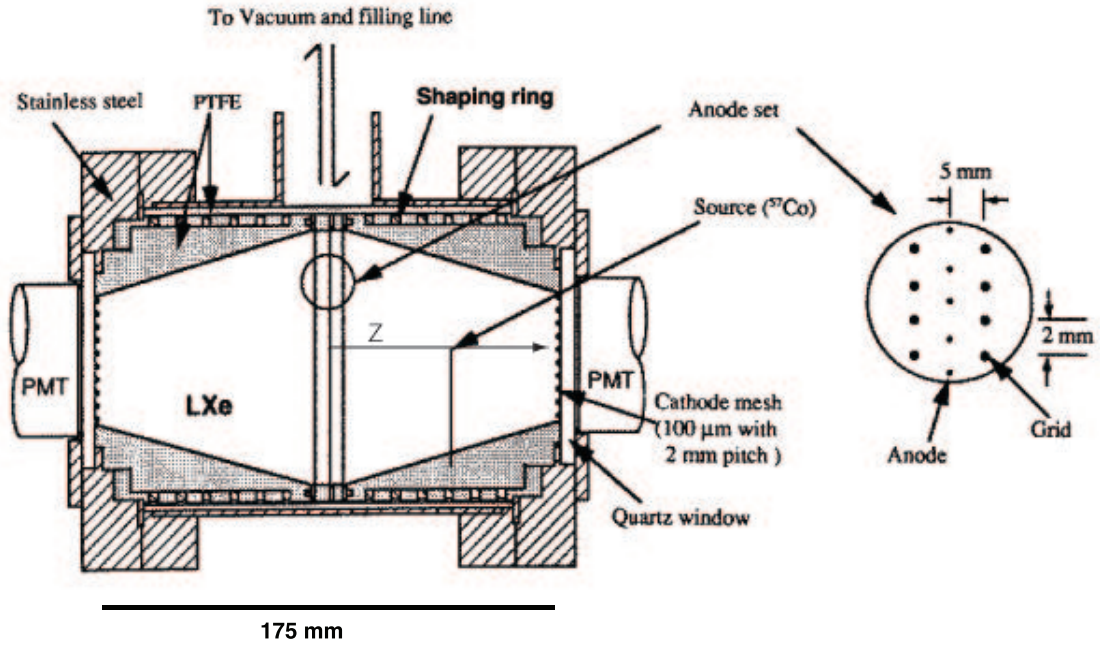

Figure 5.1: Schematic view of the chamber for measuring the reflectance of PTFE.

5.1.3 Monte Carlo simulation for the light collection efficiency

For measuring the reflectance coefficient of PTFE, a Monte Carlo simulation was performed to calculate the light collection efficiency on the PMT photocathode, which depends on the position of light emission in the LXe. The variable f is defined as the ratio of the number of incident photons on the photocathode to the photons generated. Each photon was traced through the whole detector until it hit the PMT photocathode or was absorbed by a material surface or by the LXe possibly due to photo-absorption by impurities. The reflection and absorption on the surface of the PTFE reflector and the wire, the reflection and refraction on the boundary with other media like LXe, the MgF_2 window, the vacuum and the windows of PMTs were taken into account. The reflections on the PTFE surface were treated as perfect diffuse reflections which follow the Lambert law and those on the boundary of other media were simulated as a regular reflection. The refractive index used for LXe was 1.61 [48] while a value of 1.45 was used for the MgF_2 windows. The optical transmissions of the wire set, meshes on the MgF_2 windows and MgF_2 windows were also included. Fig.5.6 shows the optical transmission of MgF_2 window as a function of wave length with the spectrum of LXe scintillation light. We take 90% for the optical transmission of MgF_2. The value of Rayleigh scattering in LXe was already measured [52] and calculated [53]. A Rayleigh scattering length of 30cm was assumed in this simulation, however the effect of this length was negligible to the result in this simulation. Each photon was reflected on the reflective surface with R_f, where

R_f is the reflectance of PTFE, otherwise it was considered as absorbed and the total path length of photon track is described as the light absorption length (λ) in LXe.

5.1.4 Result of reflectance of PTFE measurement

Measurements were made at three different source position, z = 20, 50, 74 mm. The reflectance R_f of the PTFE wall for LXe scintillation light can be determined by fitting the MC simulation to the experimental data. The results are shown in Fig.5.2 together with several possible solutions of the MC simulation for different combinations of R_f and λ. The vertical axis is lined with two scales, the left is f for the MC simulation and the right is the number of the collected photoelectrons N_{pe} for the experimental data. Three MC simulation parameters (R_f,λ); (0.95, 1.0),(0.92, 1.5),(0.88, ∞) are used , where λ is in meter. The result of three parameters are almost same and overlapped. It is reasonable to limit the maximum value of R_f to 0.95 for which a minimum value of λ = 1 m is estimated by the fit. The lower limit of R_f 0.88 can be obtained when λ goes to infinite.

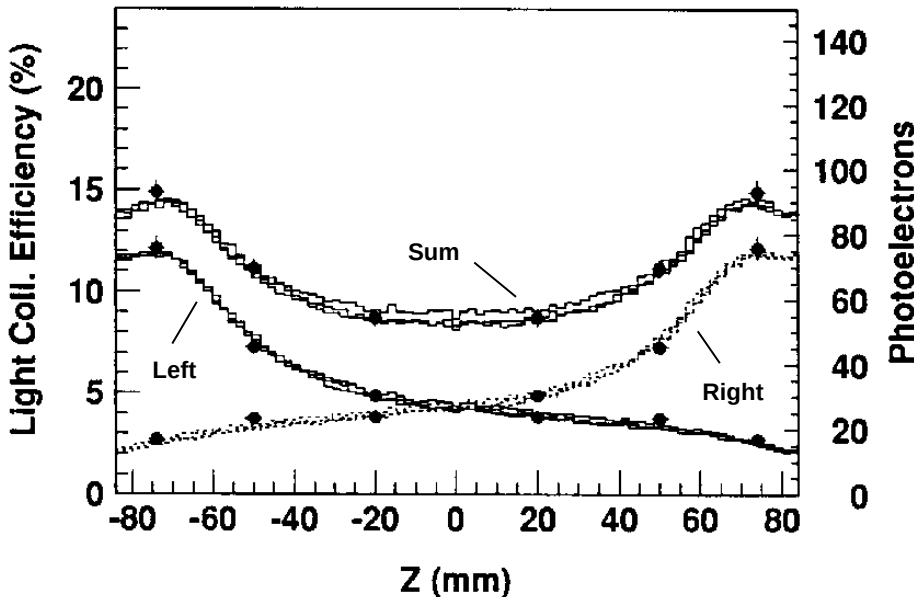

Figure 5.2: Experimental data (z = 20, 50, 74 mm) of light output N_{ph} and the light collection efficiency f for MC simulations as a function of z. Sum of the two PMT, a single PMT of left and right are plotted. Three MC simulation parameters (R_f,λ); (0.95, 1.0), (0.92, 1.5), (0.88, ∞) are used, where λ is in meter.

5.2 Background rejection method

Many direct detection experiments of Weakly Interacting Massive Particles (WIMPs) as cold dark matter candidates in the universe are under going or proposed (see eg. [19, 70]). The direct search, by means of nuclear recoil with low energy, is limited by the radioactive background from detector materials as well as the sensitivity of a detector (low energy threshold). Identification of nuclear recoil from electron recoil due to the background gamma or beta rays is great advantage for the search, because it is impossible to avoid the background from the detector itself and the surrounding materials including radiation shields. A progress of cryogenics detectors is remarkable in these days[71], this identifying technique have been developed by bolometric detectors combining with observations of ionization or scintillation signal [28, 72, 73]. Recent results to a WIMP-nucleon cross section in spin independent case are limited by CDMS, EDELWEISS and ZEPLIN I[70] experiments which are excluding DAMA allowed region[20]. For further search like the annual modulation, a large mass detector will be required to explore $<10^{-1}$ count/day/kg/keV event rate region for a statistic, while the mass of these bolometers are a few hundreds g per one module.

5.2.1 Prototype double phase LXe detector

From such a point of view, we introduce a double phase Xe detector for WIMPs direct search. Liquid Xe (LXe) is one of the excellent scintillator whose photon yield is close to that of NaI(Tl)[57]. Although special technique are required due to its short wave length (174 nm) and low operation temperature ($\sim$ 180 K) , it is possible that energy threshold can be set down to a few keV. Previously a simple method to reject of ionization events by electrons has been proposed and demonstrated by the simultaneous observation of ionization and scintillation signals in LXe[68]. In the case of Xe recoil (due to WIMP or neutron) the fraction of ionization to scintillation is much smaller than that of electrons under an ordinary electric field applied in LXe, because non relativistic heavy ions produce higher density of ionization than that of electrons, and ion-electron pairs recombine easily. Particle identification is achieved like this,

$$(\frac{\mathrm{Q}}{\mathrm{L}})_{\mathrm{electron}} >> (\frac{\mathrm{Q}}{\mathrm{L}})_{\mathrm{recoil}} \sim 0, \tag{5.2}$$

where S_c and S_s are the charge and the scintillation yield from the LXe, respectively.

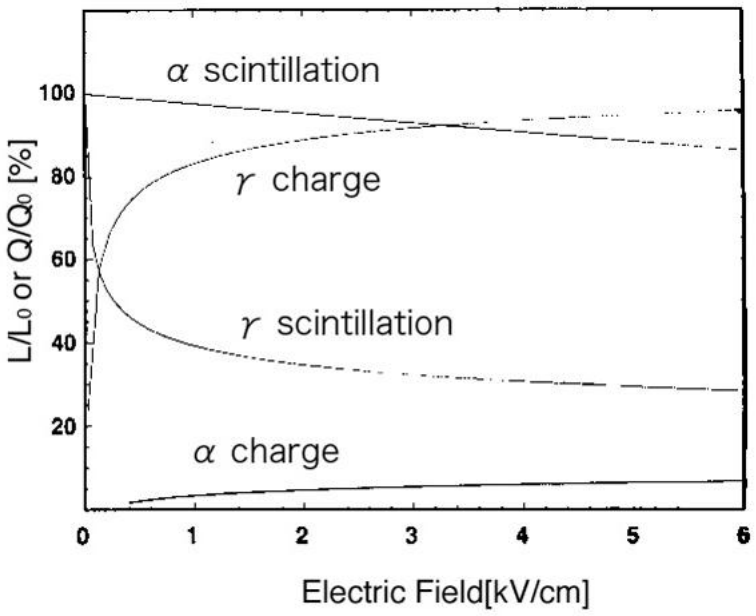

Figure 5.3: Variation of the relative luminescence intensity (L) and collected charge (Q) in LXe with the applied electric field strength for alpha particle and 1 MeV electron.

Proportional scintillation signal, instead of the primary ionization signal, produced by the extremely strong electric field near the thin anode wires was observed for low energy gamma rays. In liquid, the use of thin wires less than 10 μm in diameter is usually required but it is very difficult to handle such thin wires. Furthermore, they are easily discharged due to bad surface conditions. The lifetime of anode wires was only in few months even under low voltage in our experience. On the contrary, to improve a identification of recoil signals from background gamma rays, it is required to increase an intensity of proportional scintillation. To solve such problems, an idea of double phase detector was proposed [75]. Fig.5.4 illustrates the mechanism of the double phase detector. Liquid phase works for active region and proportional scintillation is generated in gas phase. For ionization electrons, the electric field of higher than 3 kV/cm is enough to cross the potential barrier (about 0.6 eV) between liquid and gas phase [76]. Proportional scintillation in gas phase was beginning to occur from two orders lower electric field than in liquid phase. Consequently, thicker wires are available for anode and larger number of photons can be produced in gas phase; more than 100 photons per electron compared with a few photons per electron in liquid phase. Recently a prototype double phase detector with 0.3 *l* active volume was constructed and tested in Waseda University. The scintillation response of LXe for gamma rays, basic performances and background rejections are described here.

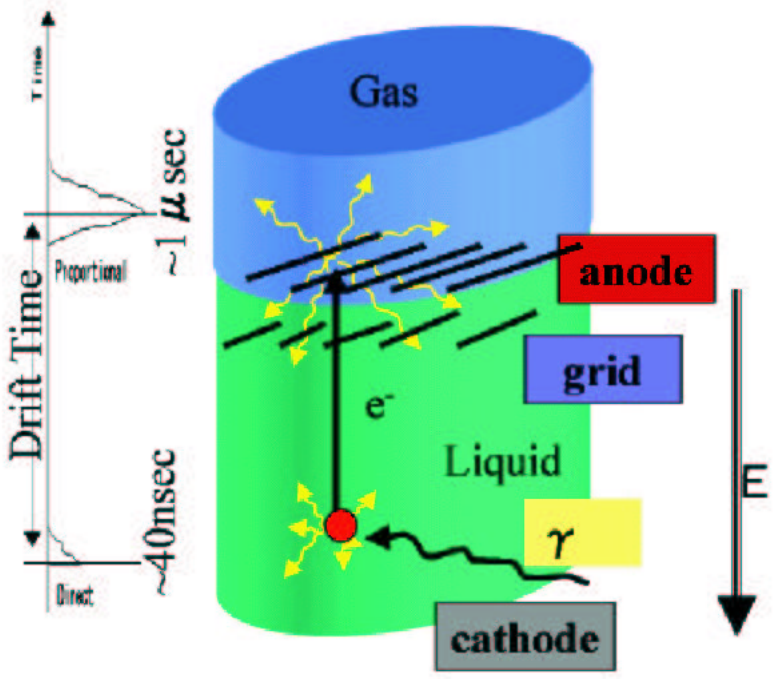

Figure 5.4: Ionized electrons drifted to grid wires, these electrons are extracted from liquid to gas phase by the strong electric field (7 kV/cm). Proportional scintillation take place at the vicinity of anode wires.

5.3 Experiments

5.3.1 Prototype design

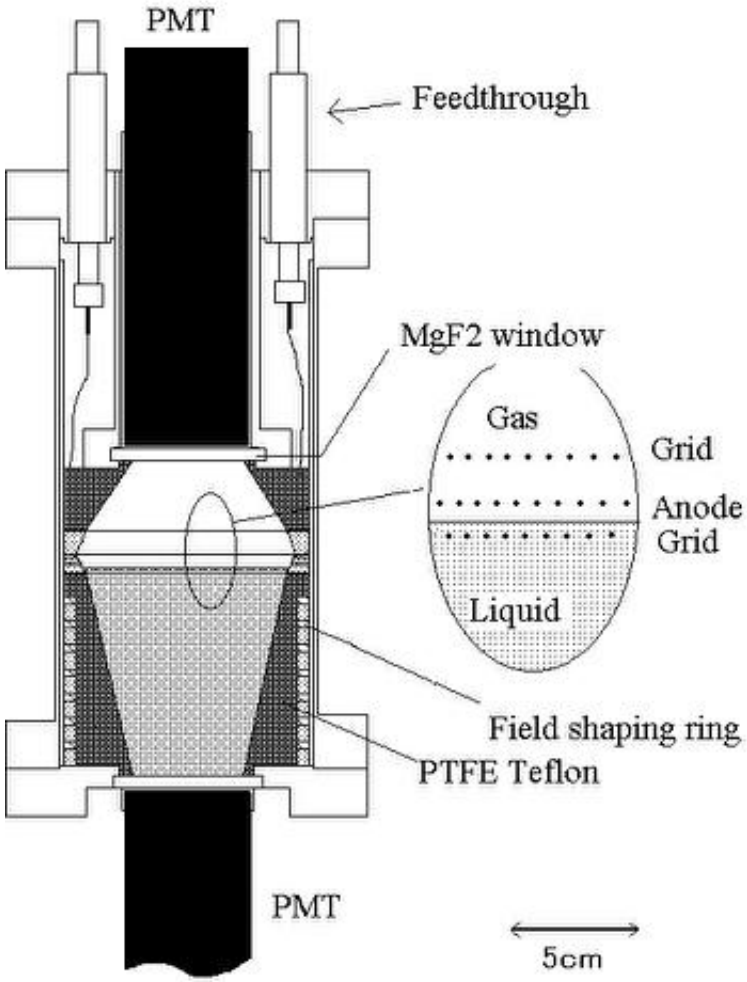

Figure 5.5: Schematic drawing of the prototype double phase detector.

A schematic drawing of the prototype double phase detector is shown in Fig.5.5. The objects of the detector design were the following[68, 69],

1) to have no dead region for either ionization and scintillation,

2) to prevent any disturbance of the drifting electrons,

3) to control separately the electron drift field and the proportional scintillation field by a grid.

A frustum of circular cone with a 0.3 *l* active volume(LXe) is formed by a longer PTFE wall and Xe vapor stays in a shorter cone. They are separated by an anode structure which consists of two sets of grid placed 15 mm apart and one set of anode wires placed in 5 mm above the bottom grid. The liquid surface stays between the bottom grid and the anode wires. The cone-shaped PTFE wall is required for high efficiency of charge collection. The anode and the cathode diameter and their distance are 84 mm, 46 mm and 85 mm, respectively. Both anode and grid wires are 30 μm in diameter and placed at 2 mm pitches. Seven field-shaping rings with 1 cm intervals are placed outside the bottom PTFE frustum in order to form a uniform drift field. A MgF_2 window is placed at each end of the PTFE. Grounded cathode meshes with 90% optical transmission are evaporated on the inner surface of the MgF_2 windows. Two UV sensitive PMTs (Electron tubes 9426B) are mounted outside the windows. For this experiment, gamma ray sources are located in an outer vessel near the detector. The following sources were used for this experiment: ^{241}Am (59.5 keV), ^{57}Co (122 keV), ^{51}Cr(320 keV), ^{85}Sr (514 keV), ^{137}Cs (662 keV), ^{54}Mn (835 keV), ^{88}Y (898,1836 keV) and Am-Be (4.43 MeV).

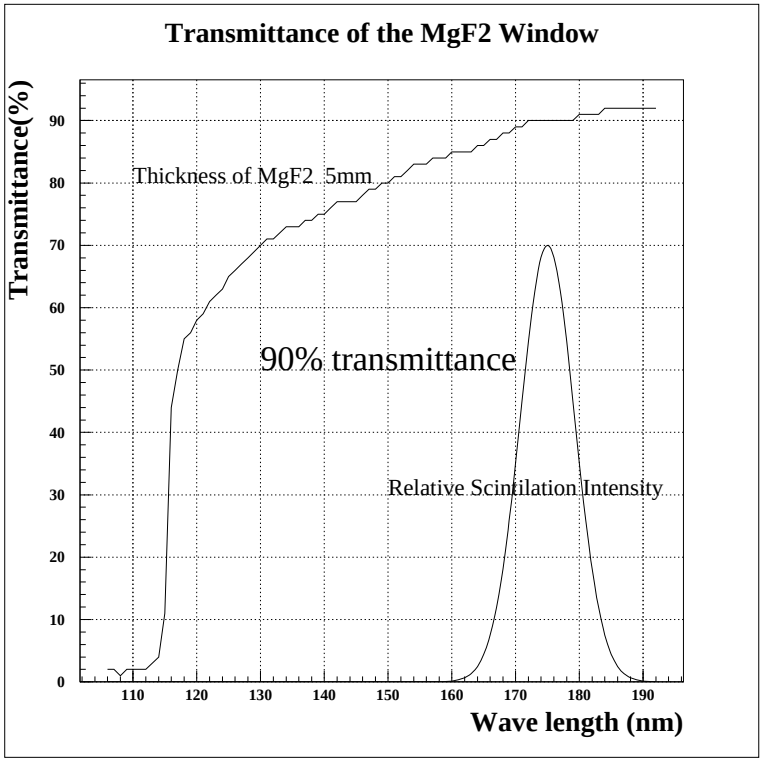

Figure 5.6: Transparency of MgF_2 at LXe scintillation wave length.

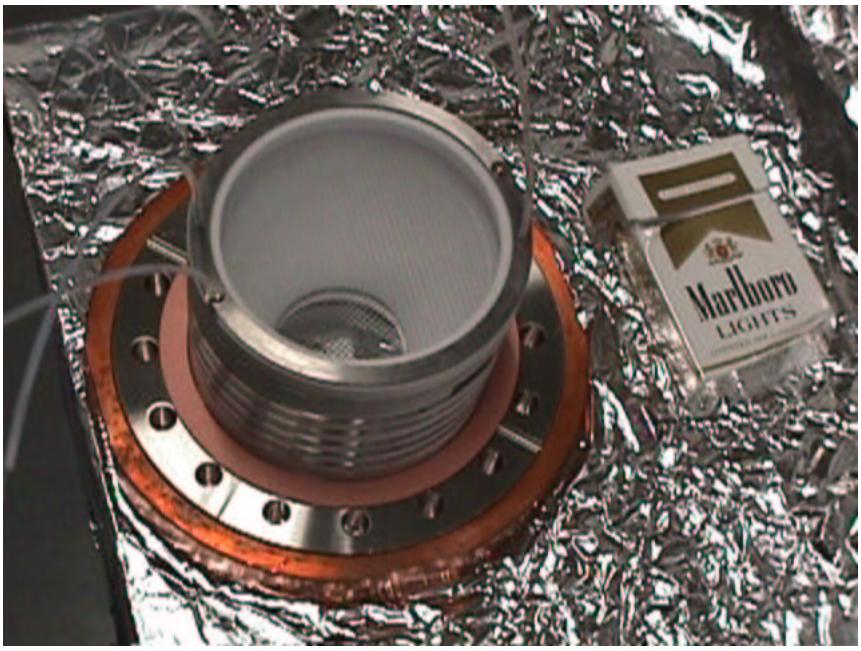

Figure 5.7: PTFE reflector and wire structure.

5.3.2 Gas line, cryogenics and purification

The detector and the gas line were evacuated and baked out for about 3 weeks at 120 °C (the detector) and 200 °C (the gas line). The vacuum pressure before experiments was smaller than 10^{-5} Pa. Xenon gas passed the Oxisorb (Messer Grieshein, 3.3 *l* volume) before filling detector with LXe. The purification was described else where in detail [69]. Fig.5.8(right) shows a schematic view of the cryogenics. 40 *l* liquid nitrogen bath installed on top and the vacuum for the thermal insulation was kept by turbomolucular pump. The detector was cooled and kept by 'Cold Finger' system, that consists of copper plates which were contacted to liquid N_2, touched the detector. The temperature of the chamber was adjusted by heaters which were mounted on copper plates and kept at 180 K.

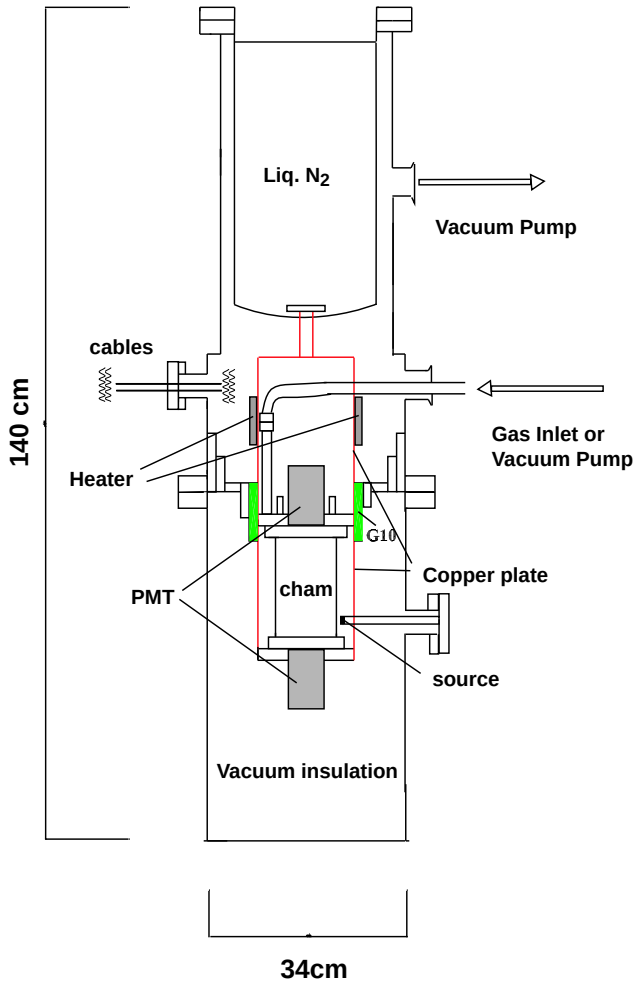

Figure 5.8: Cold finger system and the source port.

Figure 5.9: Liquid N_2 cooling system

5.3.3 Electronics and data acquisition system

The data acquisition system needs to treat two kinds of signals, direct scintillation (S1) and proportional scintillation (S2) because of its difference of time scale. Energy information from S1 was taken by CAMAC charge sensitive ADC (REPIC RPC-022). The wave forms of S1 and S2 were recorded by two digital oscilloscopes (osci-1,osci-2)in each channel. The osci-1 was set to 50 nsec/div time rage and focused to S1 which has fast decay time constant. The wave forms from osci-1 was used to identify useful signals from a dark current noise and accidental triggered by S2. The summed signal was connected to osci-2 after a shaping amplifier (EG&G ORTEC 450 Research amplifier) with 2 μsec shaping time constant. The osci-2 was set to 5 μsec/div and recorded from S1 for 50 μsec, because S2 appears within $\sim$ 45 μsec after S1 (Fig.5.14). The pulse height of S2 and the time interval between S1 and S2 were derived from osci-2. The data from oscilloscopes were transfered to PC by GPIB (IEEE-488) interface.

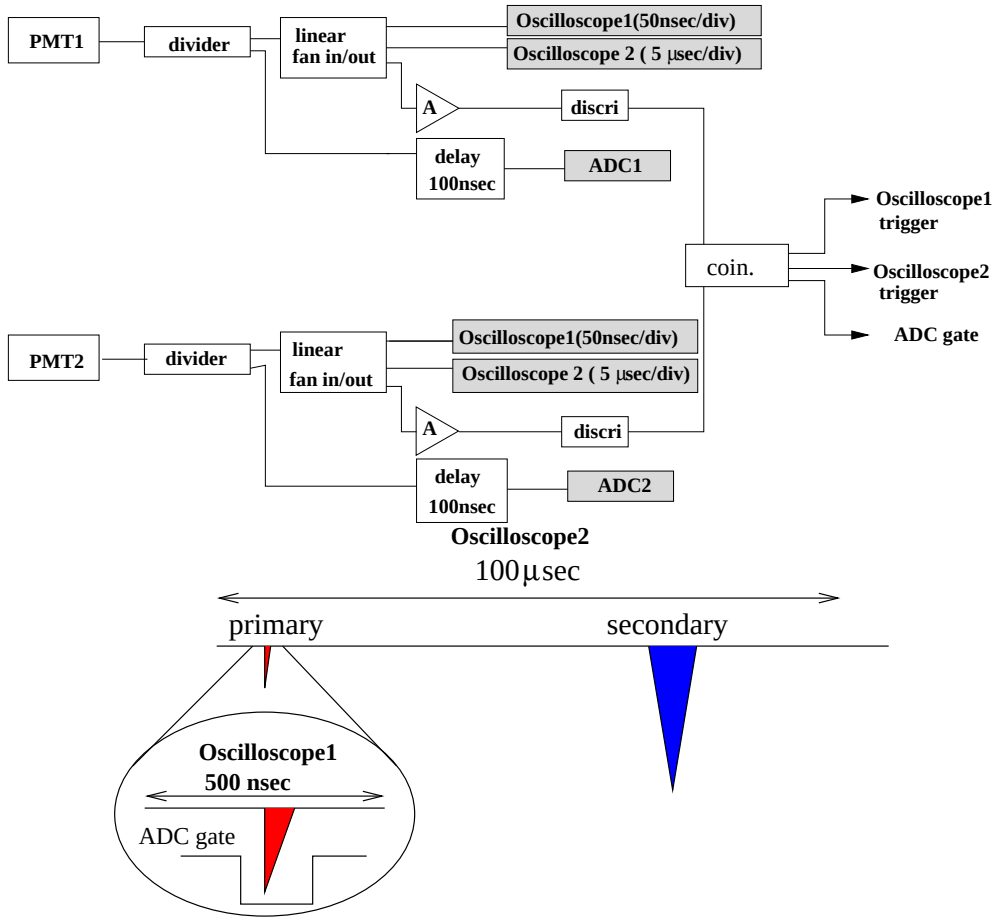

Figure 5.10: The schematic view of the electronics

5.4 Results

5.4.1 Energy resolution

The energy spectrum for LXe exposed to 59.5 keV, 662 keV, 898 keV and 1836 keV is shown in Fig.5.11. The escape X ray peak is also shown in Fig.5.11(a). The energy resolution (σ/E) for 59.5 keV, 662 keV and 1836keV are 16.7%, 7.1 % and 5.0%, respectively. The 59.5 keV, 122 keV, and the X ray escape peak were fitted by Gaussian distributions, the other energies were fitted by Gaussian distributions plus 2nd order polynomial function. Fig.5.12 shows the energy resolution for several gamma rays sources. The energy peak at 4.43 MeV from Am-Be was not clearly distinguishable from the two escape line at 3.92 and 3.41 MeV. The best fits to the data is $\sigma/E = 118/\sqrt{E} + 2.2[\%]$ as shown in Fig.5.12. Energy resolution are summarized in Table5.1.

gamma source	Energy[keV]	Energy resolution(σ/E)[%]
^{246}Am	59.5	16.7
^{57}Co	122	12.1
^{51}Cr	320	8.7
^{85}Sr	514	7.5
^{137}Cs	662	7.1
^{54}Mn	835	6.3
^{88}Y	898	6.5
^{88}Y	1836	5.0

Table 5.1: Energy resolution by Double phase detector.

(a)

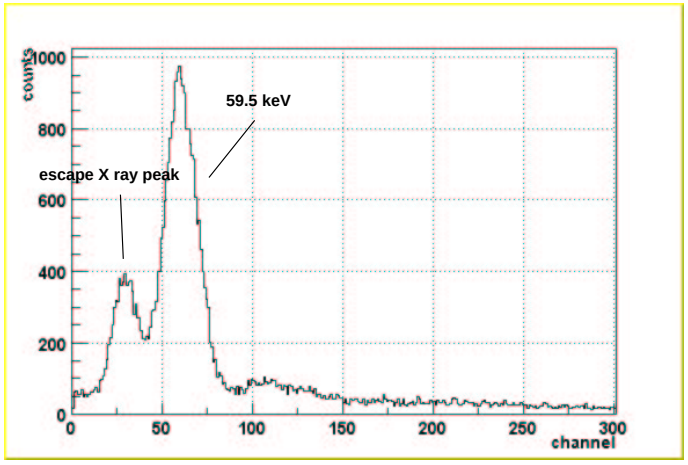

(b)

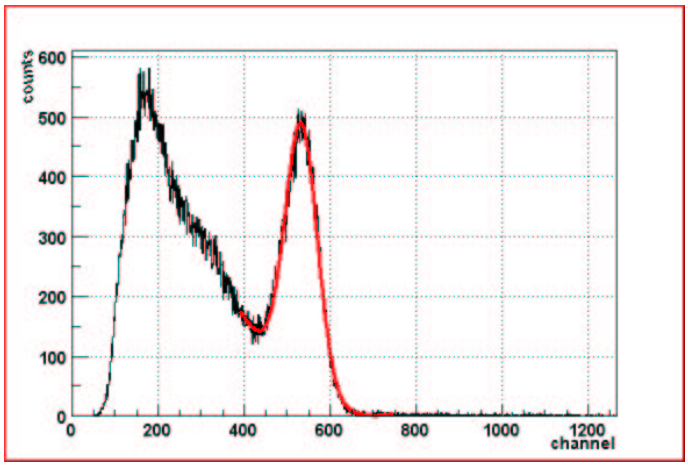

(c)

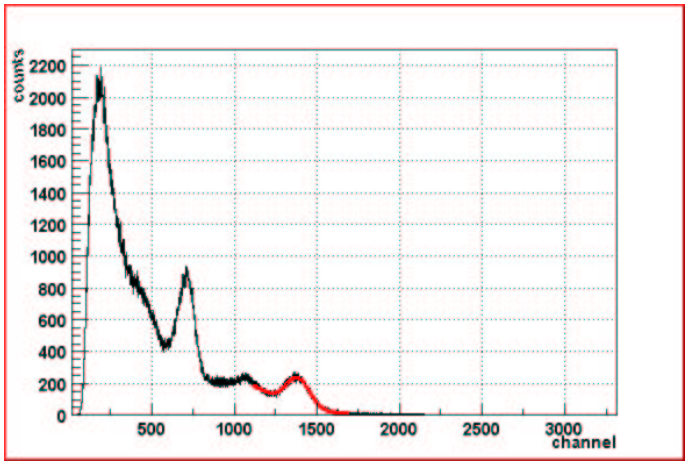

Figure 5.11: Energy spectrum for ^{241}Am(59.5keV) gamma rays (a) , ^{137}Cs(662keV) (b), ^{88}Y (898,1836keV) (c). Escape X ray peak is also shown in (a).

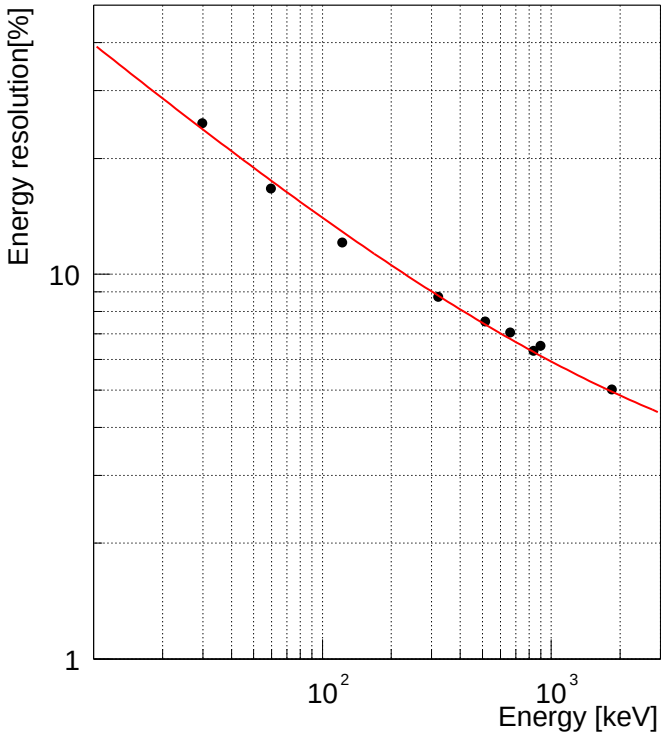

Figure 5.12: Energy resolution as a function of gamma ray energy. The fitted function is $\sigma/E = 118/\sqrt{E} + 2.2[\%]$

5.4.2 Scintillation efficiency for LXe

Fig.5.13 shows the scintillation efficiency L of LXe normalized at 662 keV. It was highest at 59.5keV, decreasing with increasing energy, and limited to 0.9 above 2000 keV. L for the two-escape lines at 3.92 and 3.41 MeV are plotted peak value instead of fitting with Gaussian, but 4.43 MeV was not seen clearly.

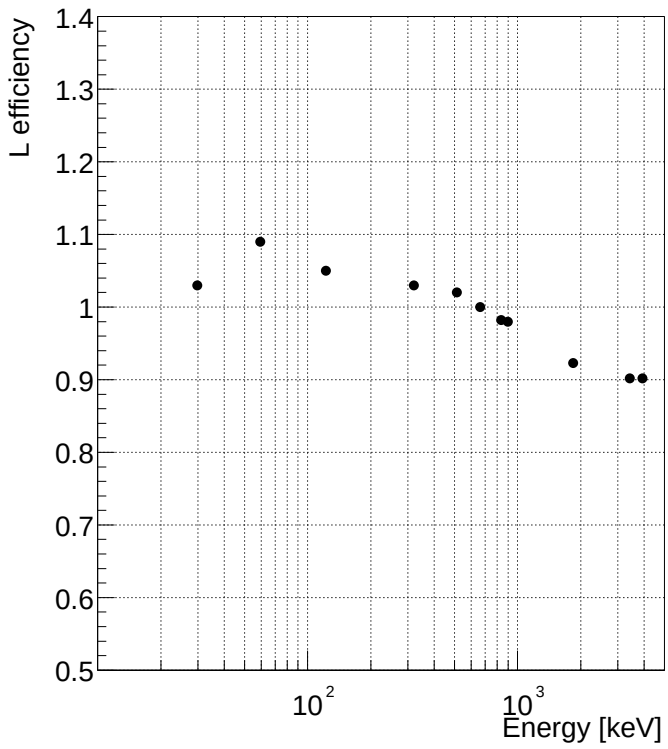

Figure 5.13: Scintillation efficiency (L) as a function of gamma ray energy. L is normalized at 662keV.

5.4.3 Basic performance

Typical scintillation signals of gamma rays from the sum of the two PMTs are shown in Fig.5.14. The first, small and narrow pulse(30-40 nsec decay time) corresponds to S1 and the following huge signal(around 1 μsec pulse width) to S2. Here drifting(cathode-grid) electric field is E_d = 250 V/cm and anode-grid electric field is E_{ag}= 7 kV/cm. The time intervals between S1 and S2 correspond to the electron drifting time from the ionizing point to the anode wires. The energy is estimated around 50 keV by S1 intensity. Events in gas phase are easily distinguishable because of their longer decay time(more than 100 nsec) of S1.

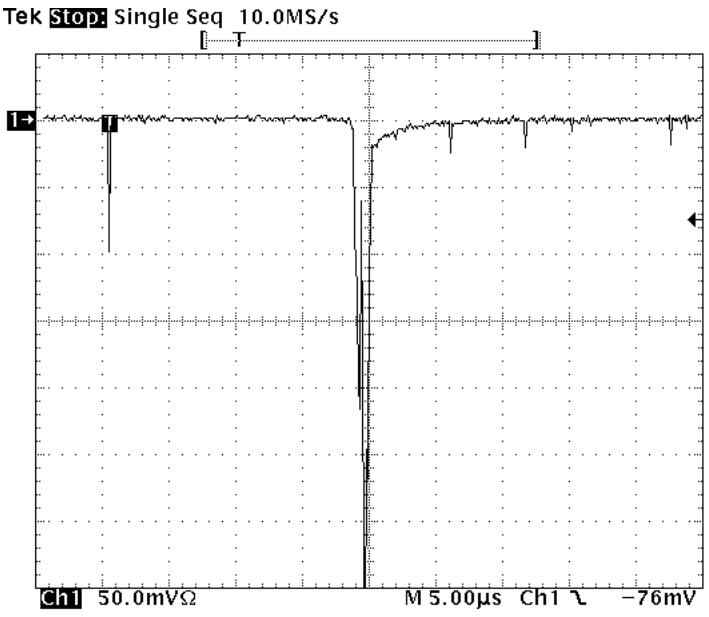

Figure 5.14: Typical scintillation signals from two PMTs for low energy gamma ray at E_d = 250 V/cm and E_{ag}= 7 kV/cm.

Variations of scintillation intensity for electric field were measured. 59.5 keV gamma rays from ^{241}Am source are exposed to the detector from outside for energy calibration. Fig.5.11(a) shows energy spectrum under no electric field. The energy resolution (σ/E) was 16.7% at 59.5 keV. Full absorption and escape X-ray peaks were observed. Fig.5.15 and Fig.5.16 show the variation of S1 and S2 intensities as a function of E_d at E_{ag}= 7 kV/cm, respectively. S1 decreases with E_d and was not affected by E_{ag}. On the other hand, S2 increases with E_d and is similar to the electric field dependence of direct charge collection [80]. Fig.5.17 shows the variation of S2 intensity as a function of E_{ag} at E_d= 250 V/cm. Multiplication gain of S2 increases with E_{ag} for all region in this figure. S2 was observed even at lower electric field($<$ 4 kV/cm) but unstable, because of electric field should not be enough to extract electrons from liquid to gas phase. The ratio of S2/S1 can be maintained to be at least greater than 10 by adjusting E_{ag}.

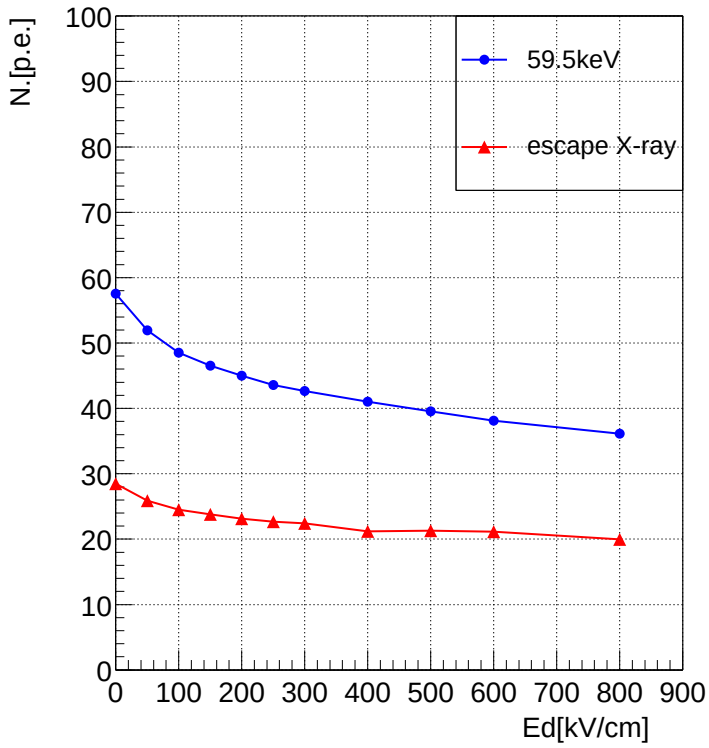

Figure 5.15: Variations of direct scintillation intensities for 59.5 keV gamma rays and escape X-ray , as a function of E_d.

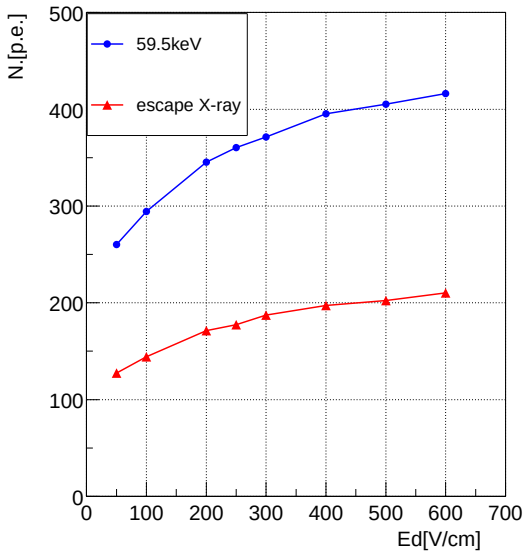

Figure 5.16: Variations of proportional scintillation intensities at E_{ag}= 7 kV/cm for 59.5 keV gamma rays and escape X-ray as a function of E_d.

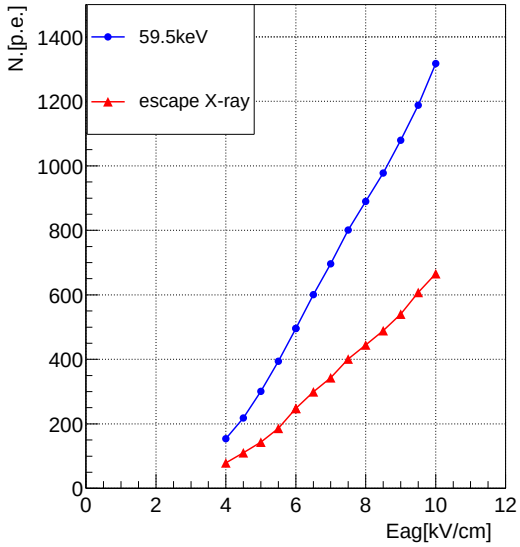

Figure 5.17: Variations of proportional scintillation intensity for 59.5 keV gamma rays and escape X-ray as a function of E_{ag}.

5.4.4 Electron lifetime

In order to operate properly this kind of detector, high transparencies for drifting electrons and scintillation light are extremely required. A light attenuation length of more than 1m in LXe were successfully achieved by a special purification process and a stable cryogenic technique [69]. Two thousands events of low energy background gamma rays, which were discriminated between 10 and 100 keV by S1, were sampled. The averaged number of photoelectrons from S2 for every 5 μsec interval of electrons drifting time is shown in Fig.5.18. On the horizontal axis of the figure, time zero and 45 μsec correspond to the position of anode and cathode, respectively. The charge collection between the anode and the grid is higher than that of drift region. The component of background around the cathode region must be different from the other. Except both regions averaged photon number slightly decrease with increase of electrons drift time. It should be mainly caused by electron attachment due to electronegative impurities. The lifetime of drifting electrons was estimated 3 msec, which was corresponds to about 5 m attenuation length, by assuming that averaged absorption energy from background gamma rays is uniform in the LXe (Fig.5.18). The detector was maintained for three months and no significant change was observed without additional purifications during that time.

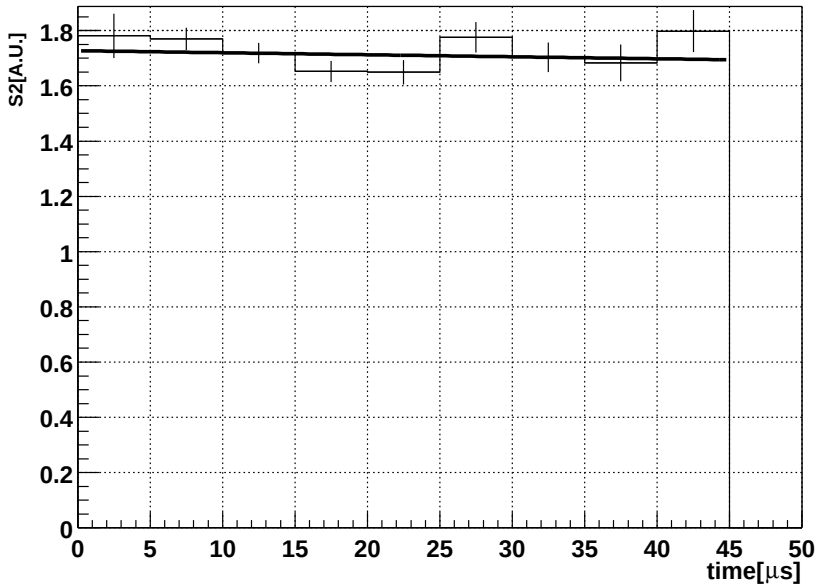

Figure 5.18: Electron life time attenuation in LXe is 3 msec. Solid line correspond to 5 m attenuation length.

5.4.5 Background rejection

Fig.5.19(left) shows the correlation between S1 and S2 obtained from two thousands of low energy events which are selected by S1. Applied electric fields are E_d = 250 V/cm and E_{ag}= 7 kV/cm. It is obviously separated in two groups; about 99 % events have enough big proportional scintillation (S1 $<<$ S2) and S2 are small or zero for the rest. We made a test by exposing a low active Am-Be neutron source (about 200 cps for 4 π direction). The result is shown in Fig.5.19(right). The number of small S2 events were clearly increased. Mean event rate of low energy gamma rays by the detector was around 3.5 Hz and neutron background was about 0.2 Hz in the laboratory, which was estimated by a well-calibrated neutron counter. Taking account of these all facts, the rejection efficiency of the detector for background gamma and beta rays is much better than 99 %.

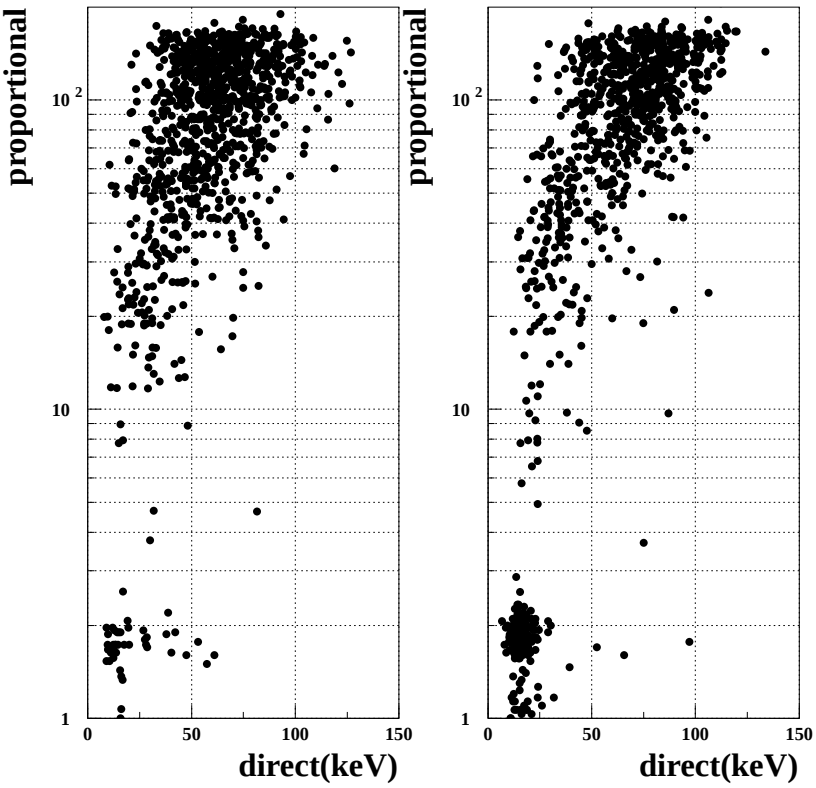

Figure 5.19: Correlation between direct and proportional scintillation. Each event is presented by plot; only background on surface laboratory(left), background plus Am-Be neutron source(right).

5.5 Discussion

5.5.1 Monte Carlo simulation and energy resolution

Fig.5.20 shows the distribution of the light collection efficiency f_{dp} for the double phase detector. In this Monte Carlo simulation, photons are generated everywhere in the LXe. The parameters used in this simulation are listed in Table9.1. The fluctuation of the light collection (σ/f_{dp}) due to changing position is 2.5 %. In case of low energy gamma rays, the positions of photon emission are well localized. For energies of higher than a few hundred keV, they are spread over the full detector volume. In fact, the data from Barabanov et al. showed that the energy resolution for 662 keV was the same as for 122 keV or even slightly worse, but in the present data, the energy resolution becomes better and better with increasing gamma rays energy as shown in Fig.5.12.

Parameter	Value
Refractive index MgF_2	1.45
Reflective index PTFE	95% (diffuse)
Absorption length in LXe	1m
Rayleigh scatter	30cm

Table 5.2: Parameters for the Monte Calro simulation.

5.5.2 Scintillation efficiency

L in Fig.5.13 continuously decreases with increasing energy in the range of 59.5 keV-3.92 MeV. Its variation is about 20%. Barabanov et al. reported a 30% variation, although they got a similar curve shape as in the present work. One of the reasons might be the non-uniformity of light collection. They also used a Teflon® reflector, but its reflection coefficient was estimated to only 60%. Also their actual energy resolution was much worse than in this work. The reason of non-linearity in scintillation yield, in particular, in the region where the scintillation yield decreases with the energy of gamma-rays is simply explained as follows by the so-called ”escape electrons” effect. The scintillation light emission is produced by two processes of excitation and recombination and the main part of the scintillation is produced through recombination process. In such a case, a fraction of electron escapes from recombination when the electron-ion density is low as in relativistic electron and as a result the scintillation yield is reduced. The variation of *L* between 30 keV and 59.5 keV is consistent with that of Ospanov and Obodovoski[77]. In such a low energy region, Tojo [78] explained for NaI(Tl) that *L* is changed by the contribution of photoelectrons from the K or L-shell of an atom, and this is also as valid for LXe. For electrons over 2000 keV, *L* is constant almost 0.9. In this region, it is assumed that the part of high ionization density at the end of a track is negligible and does not significantly contribute to the total energy deposited in LXe.

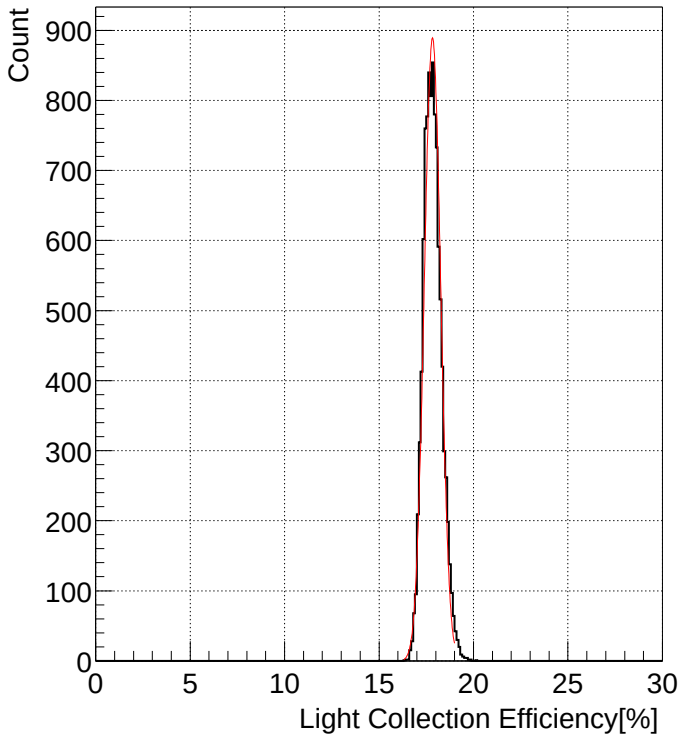

Figure 5.20: Distribution of the light collection efficiency (f_{dp}) for the double phase detector. The fluctuation (σ / f_{dp}) is 2.5%.

Chapter 6

Experiment in a deep underground laboratory

We constructed the new detector for the underground experiment. In this chapter, the experiment in Kamioka mine are described.

Figure 6.1: Location of Kamioka Observatory.

6.1 XMASS experiment at Kamioka

There are many interesting physics in the underground physics. XMASS project [84, 85, 86] has three goals for

- Xenon MASsive detector for Solar neutrinos,
  (pp, ^{7}Be neutrino experiment)
- Xenon detector for weakly interacting MASSive particles,
  (Dark Matter experiment)
- Xenon neutrino MASS detector.
  (Double Beta decay experiment)

As a part of this project at Kamioka mine, the double phase Xe detector was constructed for WIMPs dark matter experiment. The depth and the muon flux of this deep underground laboratory is about 1000 m (2700m.w.e.) and about 10^{-7} cm^{-2}/sec, respectively. In this section, double phase Xe detector at Kamioka mine is described.

site	muon flux [cm^{-2}/s]
surface	1.1×10^{-2}
Kamioka	$\sim10^{-7}$

Table 6.1: The muon flux of surface laboratory and Kamioka mine.

6.2 Detector set up

1 kg Kr-free LXe (Kr 10 ppb) was surrounded by frustum of cones made from PTFE Teflon and MgF_2 windows completely. LXe stay in a bottom cone, a largest diameter is ϕ 80 mm. Thickness of gas and liquid are 25 mm and 95 mm. They are separated by an anode structure (gold coated ϕ 30 μm tungsten wires) which consists of two set of grids placed at 5 mm (liquid part, G1) and 15 mm (gas part, G2) from the anode wires. Two MgF_2 windows (an effective diameter of 46 mm and 5mm thickness) are fixed on both end of the detector. Nickel meshes (cathode), whose optical transmission is $\sim$ 90 %, were evaporated on the inner surface of them. 9 field-shaping rings with 1 cm intervals are placed outside the bottom Teflon in order to form a uniform drift field.They are chained with nine 20MΩ resistors from G1 to the grounded cathode. The inner vessel is made of 5cm thickness of OFHC copper. The vacuum or gas filling stainless steel of CONFLAT flange is welded to the inner vessel. The detector was evacuated and baked out for about 3 weeks at 120 $^{\circ}$C (the detector). The vacuum pressure before experiments was smaller than 10^{-5} Pa. Two PMT with Quartz window was coupled to windows through 1mm thickness of vacuum. Electric field between cathode and G1 was 250 V/cm and between G1 and anode was 7 kV/cm. The detector was thermally insulated by vacuum and cooled by liquid nitrogen through the copper plates (cold finger system). Temperature of the detector was kept by the cold finger system with heater at 180K.

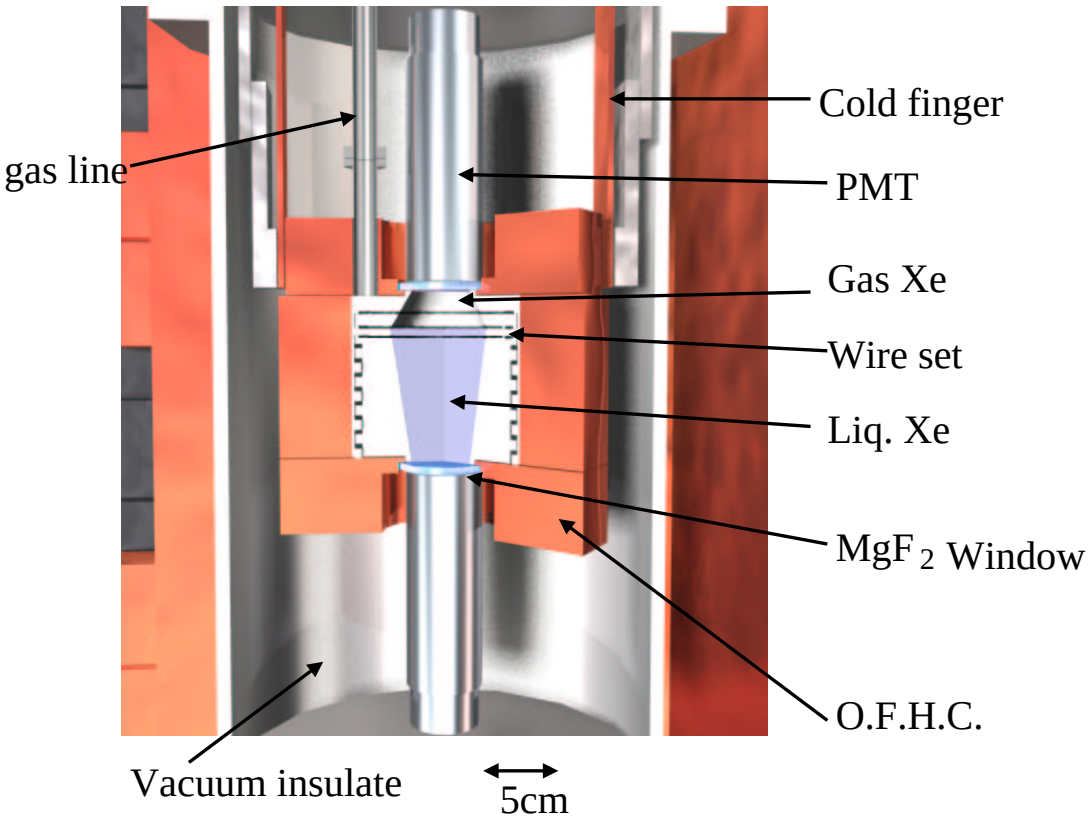

Figure 6.2: Schematic view of the detector.

Figure 6.3: Installation of Teflon

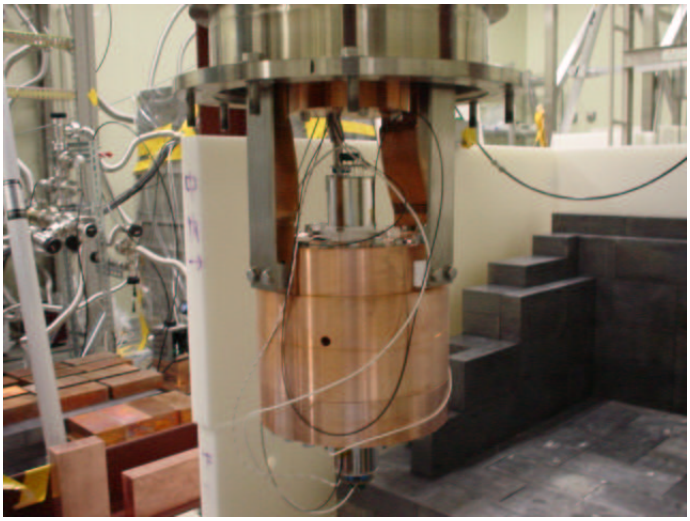

Figure 6.4: Picture of the detector.

6.3 Gas line

All of parts (SUS304 tubes, materials of the detector ...) were carefully cleaned by ultrasound with acetone and ethanol before fabricating the gas line system. The detector and the gas line were evacuated and baked out for about 3 weeks at 120 °C and 200 °C, respectively. The vacuum pressure before experiments was the order of 10^{-5} Pa at room temperature.

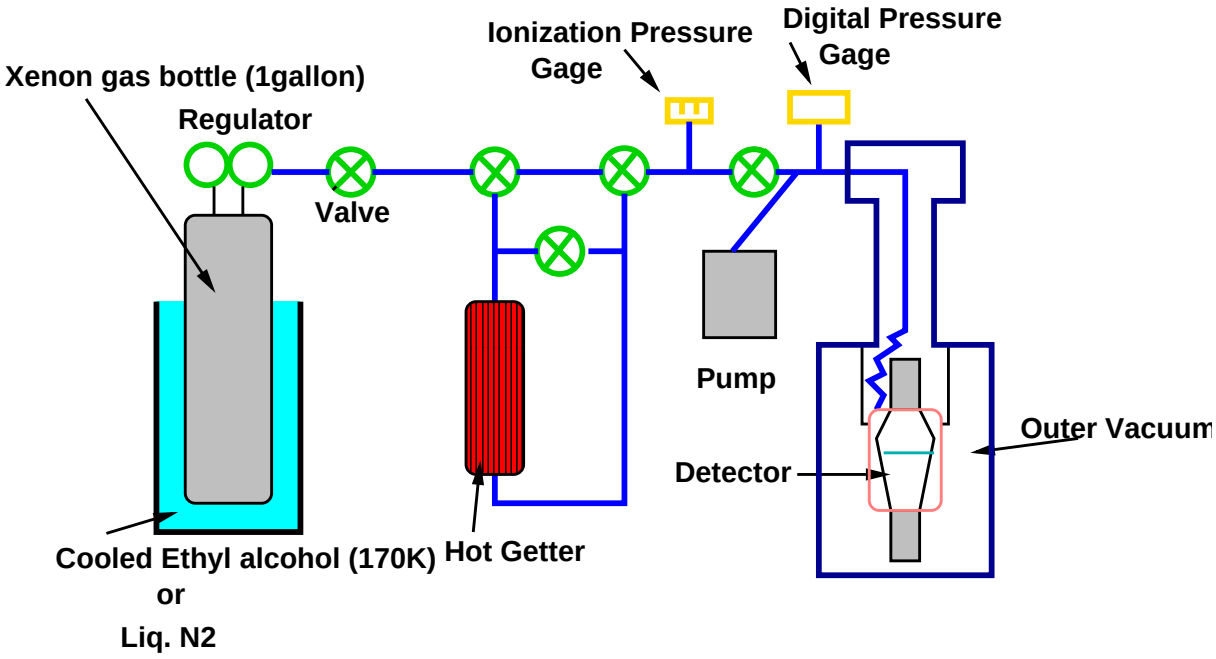

Figure 6.5: Purification and gas line system.

6.4 Purification of gas Xe

In R&D stage, Xenon gas passed the Oxisorb before filling detector with LXe and this method results for the long life time of electron as described in Section 5.4.4. However, we found that Oxisorb has a large amount of the radioactive material and gas Xe was contaminated by them during liquefaction of Xe. Fig.6.6 shows background spectrum without shield. Assuming alpha particles only come from inside the detector, the radioimpurity of gas Xe was tuned out by counting its rate. From Fig.6.6, clearly seen in higher than a few MeV energy range, Oxisorb have much radioactive materials than SAES getter.

For this reason, SAES getters [89] was used for purification. The radioactivities of these purifier was reported in [90].

Purifier	^{238}U[ppb]	^{232}Th[ppb]	K[ppm]
Oxisorb	298±33	431±9	24±5
SAES	<25	<10	<7

Inlet Impurity	H_2O	O_2	CO	CO_2	N_2	H_2	CH_4
Outlet	<1ppb	<1ppb	<1ppb	<1ppb	<1ppb	<1ppb	<1ppb

Table 6.2: The radioactivity in Oxisorb and SAES getters[90] and Performance Guarantee of SAES getters.

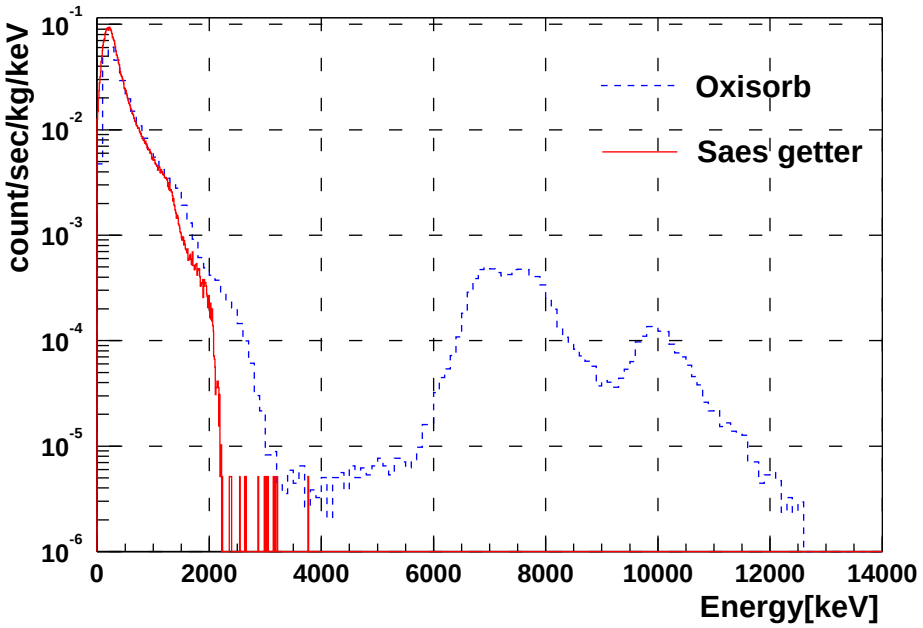

Figure 6.6: Purification and gas line system.

6.5 Cryogenics

Fig.6.7 shows a schematic view of the cryogenics. 100 liter liquid N_2 bath installed on top. The detector was cooled and kept by 'Cold Finger' system, that consists of copper plates and a long copper rod from liquid N_2 to the detector. The vacuum for the thermal insulation was kept by turbomolucular pump. The temperature of the detector was adjusted by a heater which were mounted near the Liq. N_2 bash and kept at 180 K.

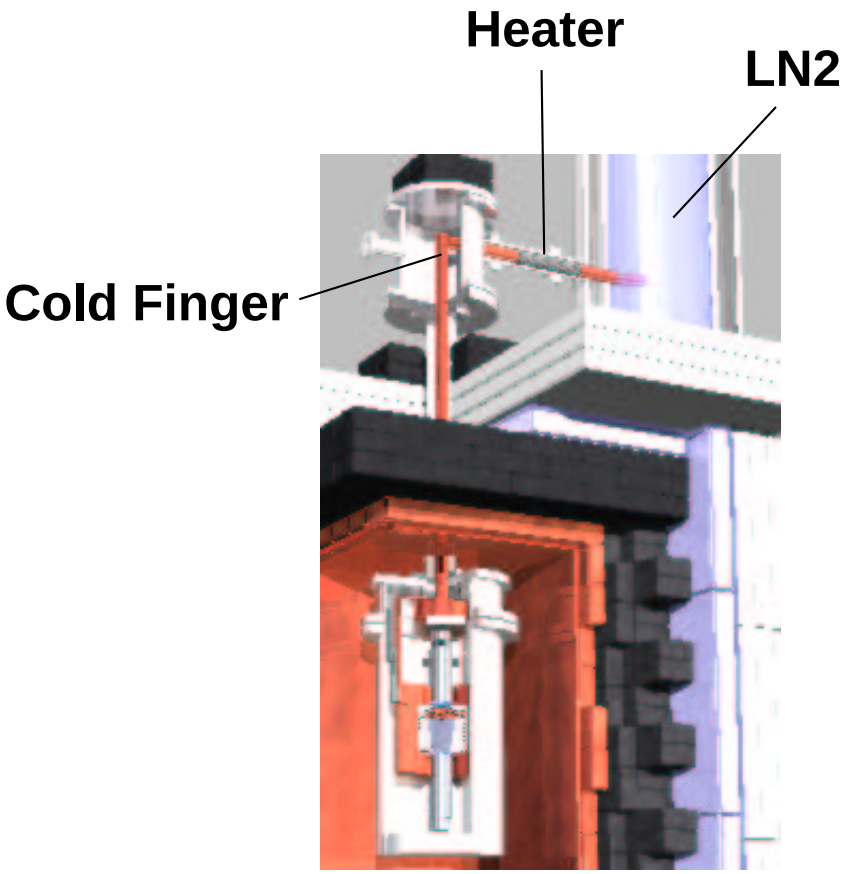

Figure 6.7: Schematic of Cryogenics.

6.5.1 Low background PMT

The PMTs, R8778Q(Hamamatsu, Quartz window), were used to detect LXe scintillation light. This PMT has high quantum efficiency ∼30% at 174nm. Fig.6.9 is the schematic view of R8778Q. The quartz window and metal tube are used in this PMT with plus high voltage. The voltage divider of R8778Q is shown in Fig.6.10.

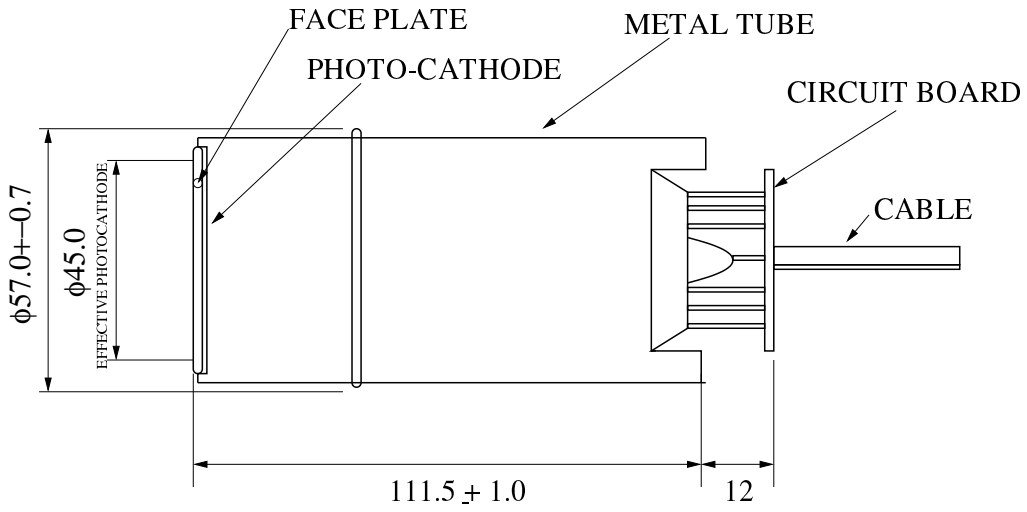

Figure 6.8: Schematic view of R8778Q.

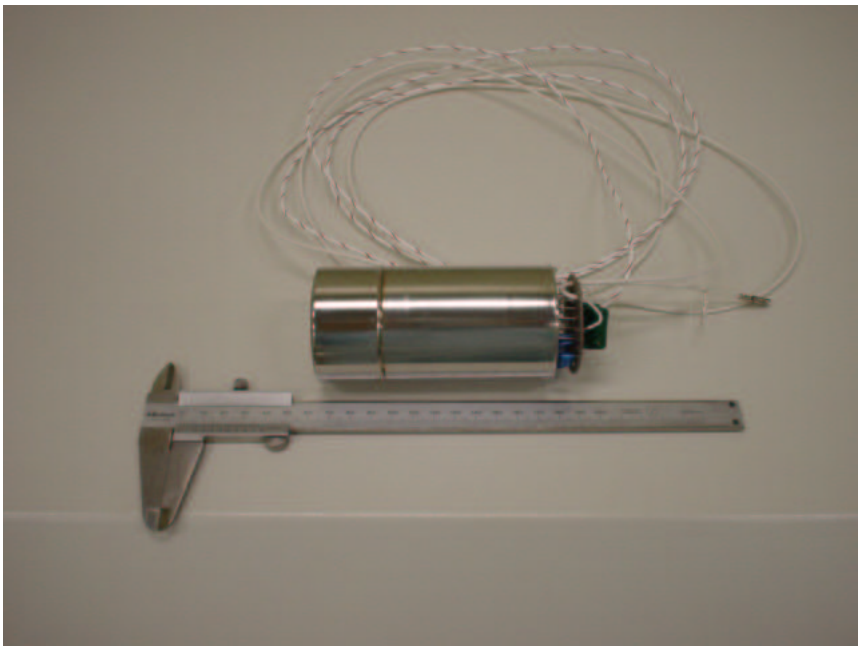

Figure 6.9: Picture view of R8778Q.

For low background experiments such as WIMPs direct search, the radioactivity of PMT is one of the most important things in scintillation detectors. Usually, PMTs are enveloped by glass, but glass has high radioactivities. This PMT was enveloped by metal tube and the circuit elements (capacitors, resistor, including PCB) were selected by the HPGe detector to reduce radioactive components[87]. Table6.3 shows the radioactivities of PMT. The contribution of this background is discussed in Section 8.2

	U chain [Bq/PMT]	Th chain [Bq/PMT]	^{40}K[Bq/PMT]	^{60}Co [Bq/PMT]
ZK0667	5.0×10^{-2}	1.3×10^{-2}	6.1×10^{-1}	$\langle 1.8 \times 10^{-3}$
Base	1.1×10^{-1}	2.7×10^{-2}	4.1×10^{-2}	$\langle 3.5 \times 10^{-4}$
R8778Q	$1.8 \pm 0.2 \times 10^{-2}$	$6.9 \pm 1.3 \times 10^{-3}$	$1.4 \pm 0.2 \times 10^{-1}$	$5.5 \pm 0.9 \times 10^{-3}$
Base	1.5×10^{-3}	1.8×10^{-3}	1.0×10^{-4}	-

Table 6.3: The radioactivities of PMT and its Base.

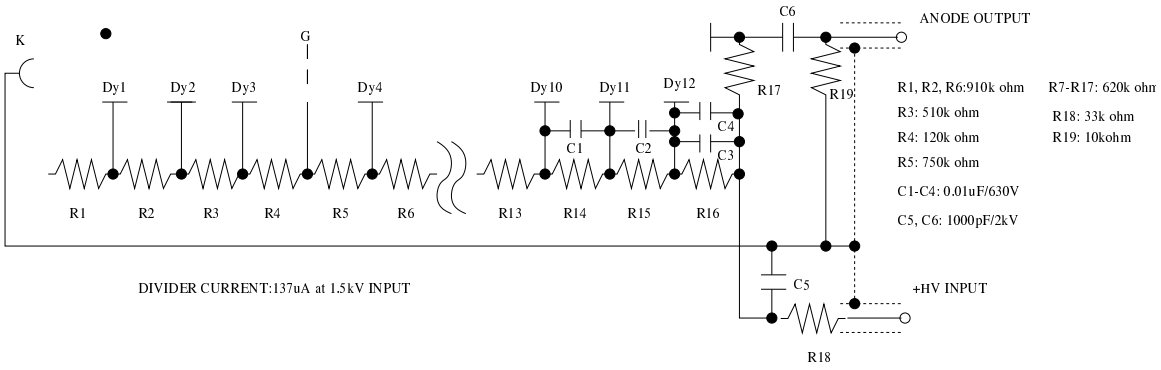

Figure 6.10: Voltage divider of R8778Q.

6.6 Shield set up

The detector is shielded against gamma rays and neutron from environment. 5 cm of OFHC copper vessel itself, 5 cm of OFHC copper and 15 cm of lead are set for gamma rays, 5 cm of Boric Acid(1g/cm^3) and 15 cm of Polyethylene are for neutron.

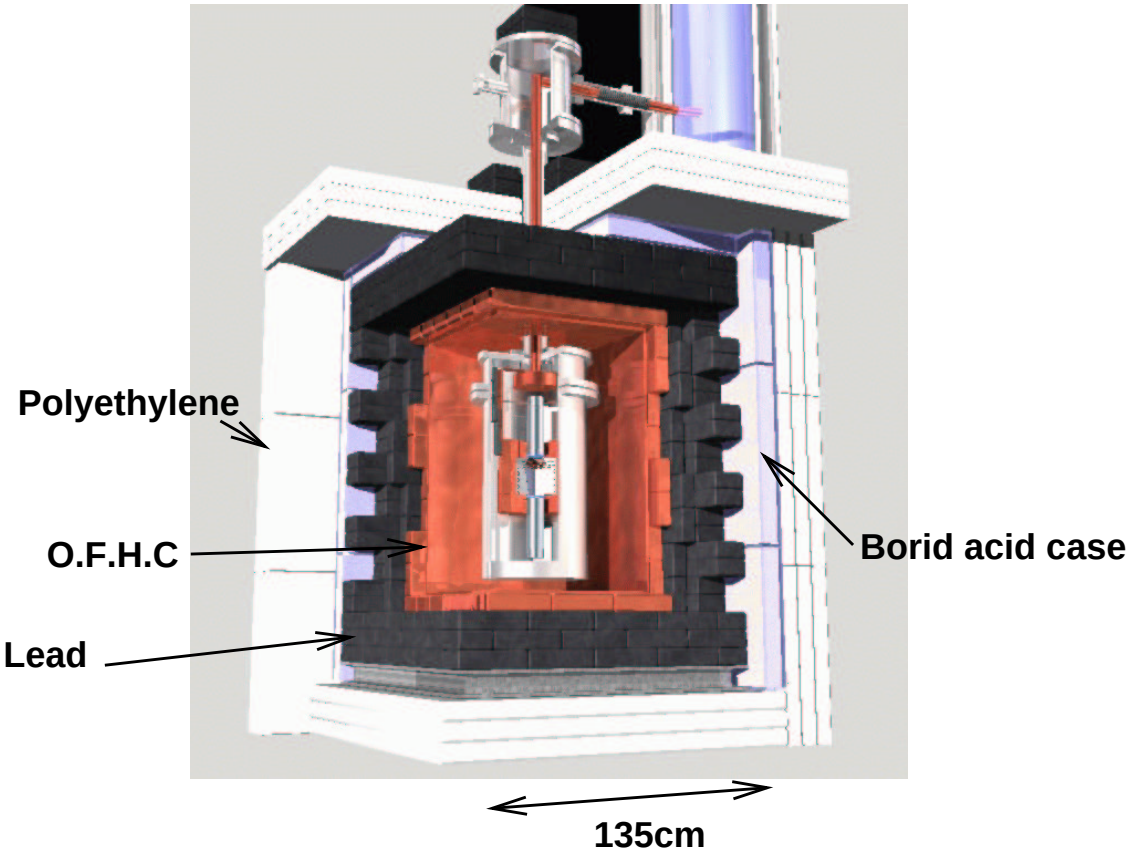

Figure 6.11: Schematic view of the radiation shield.

Figure 6.12: Picture of the radiation shield.

6.6.1 Shields for gamma rays

Lead is very effective for shielding gamma rays because of its high Z. But it has a radioactive isotope ^{210}Pb with half life time of 22.3 years. Fig.6.13 shows decay scheme of ^{210}Pb. β decay occurs from ^{210}Bi to ^{210}Po with Q value = 1163 keV and the bremsstrahlung is taken place. To avoid this effect, The OFHC copper is located inside of lead and we selected the lead itself from sample of several companies because the radioactivity of lead depends on when it was fabricated. The radioactivity of the lead blocks are measured by HPGe detector. The measurement of the radioactivity is shown in Fig.6.14 We selected lead D from various samples and results is shown in Table 6.4. The contribution of this background is discussed in Section 8.2

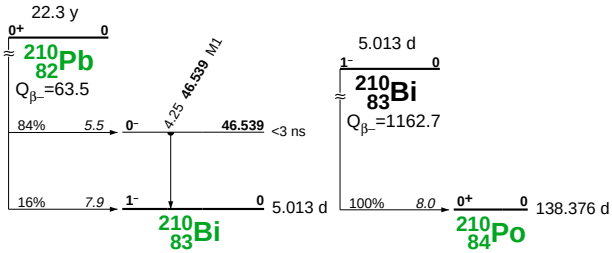

Figure 6.13: Decay scheme of ^{210}Pb[88].

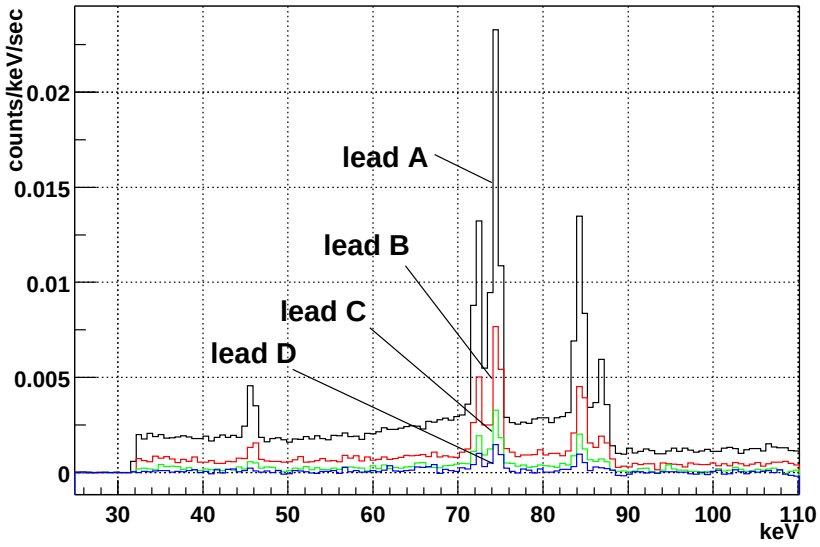

Figure 6.14: Measurement of various lead samples by HPGe .

	U chain [Bq/kg]	Th chain [Bq/kg]	^{40}K[Bq/kg]	^{60}Co [Bq/kg]	^{210}Pb[Bq/kg]
Lead D	$<4.1\times10^{-3}$	$<6.5\times10^{-3}$	$<2.9\times10^{-2}$	$<1.6\times10^{-4}$	$(2.6\pm0.4)\times10^{2}$

Table 6.4: The radioactivities of lead D.

6.6.2 Shields for neutrons

15cm thickness of polyethylene plates and Boric Acid act as the moderator and absorber for neutrons. shielding for fast and thermal neutron, respectively.

^{10}B have a large cross section for thermal neutron. We fabricated 5cm thickness of Boric acid powder with acrylic cases. Density of Boric acid is 1g/cm^3.

	abundance	cross section[barn]
$^{10}_{5}$B	19.8%	3840

Table 6.5: Cross section of thermal neutron for$^{10}_{5}$B.

6.7 Radon purge

A radon, which exists in the air, can contribute to background. The radon concentration in Kamioka mine air has a seasonal variation, its concentration is 2000-3000Bq/m^3 during the warm season, from May until October, while the 100-300 Bq/m^3 from November to April in the cold season [91] Because of its high concentration of the radon in the air, it is necessary to reduce this concentration by flowing purified (Rn-reduced), a super radon free air (SRFA) $\sim$ a few mBq/m^3 [91], around the detector.

Fig6.15 shows the comparison of the background spectrum, without the lead and copper shield, with them and with SRFA. From this result, because of the high concentration of the radon in Kamioka, the air around the detector should be keep with the low concentration of the radon air.

6.8 Data acquisition system and monitor

Fig.6.16 shows the block diagram of the data acquisition system for this experiment. The wave forms of direct scintillation light were recorded by 250 MHz flash ADC (FADC) (BASTIAN STR7515) through the VME system. Two channels of FADC were chained for digitize 500 MHz sampling rate in each PMT signal. The 12 bits charge sensitive ADC (LeCroy 1182) with through the VME system was used for the energy information. The proportional scintillation light were recorded by 10 MHz flash ADC (Rinei RPC-081) through CAMAC system in each channel.

500 MHz FADC was operated presampling mode with 8 bits. At the same timing of the ADC gate, it stops the presampling and starts to digitize for 2μsec. The length of presampling data is also 2μsec.

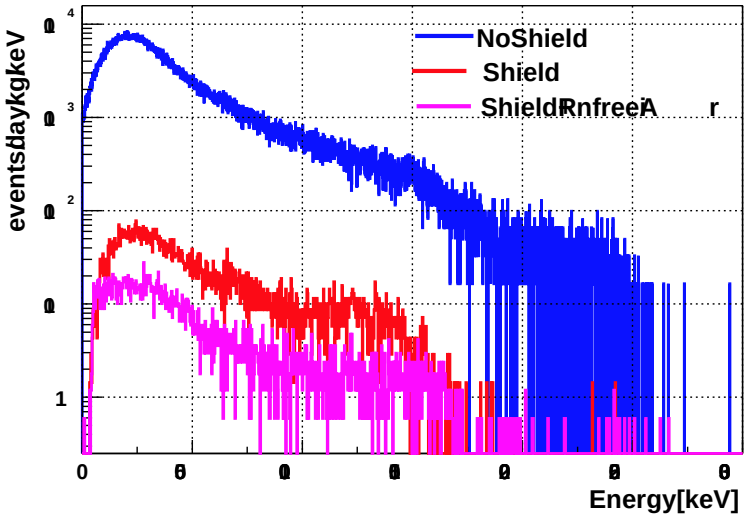

Figure 6.15: The comparison of the background spectrum, without the lead and copper shield (blue), with the shield (red) and with SRFA(pink). The typical radon concentration of SRFA is a few mBq/m^3.

100 MHz FADC was also operated presampling mode and it digitize for 100μsec and stops after 80μsec from the gate signal.

The temperature of the detector and Cold Finger were measured by using platinum sensor (PT100). These temperature and the pressure of the inner detector and vacuum insulate are monitored by the multi channel digital meter (KEITHLEY 2700). This digital meter was connected to PC by GPIB(IEEE488) interface.

As the measurement is performed in the mine, these housekeeping data are sent Web server machine the minute by minute, and the collaborator can see the status of the detector in Web site and also by a cellular phone [92]. Fig6.17 shows the housekeeping status display. DAQ and monitor system were controlled by PC with Linux operating system.

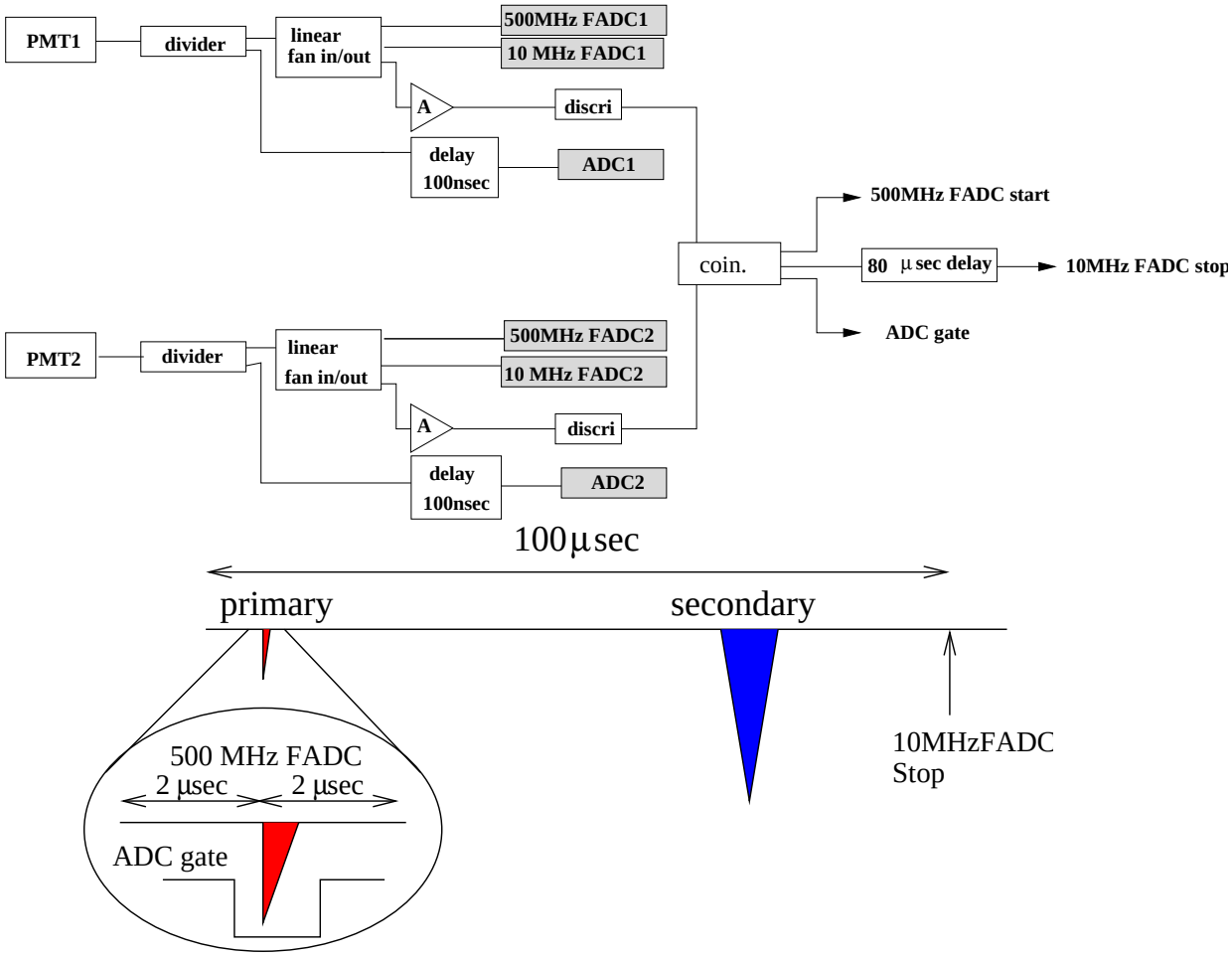

Figure 6.16: Schematic of Daq diagram .

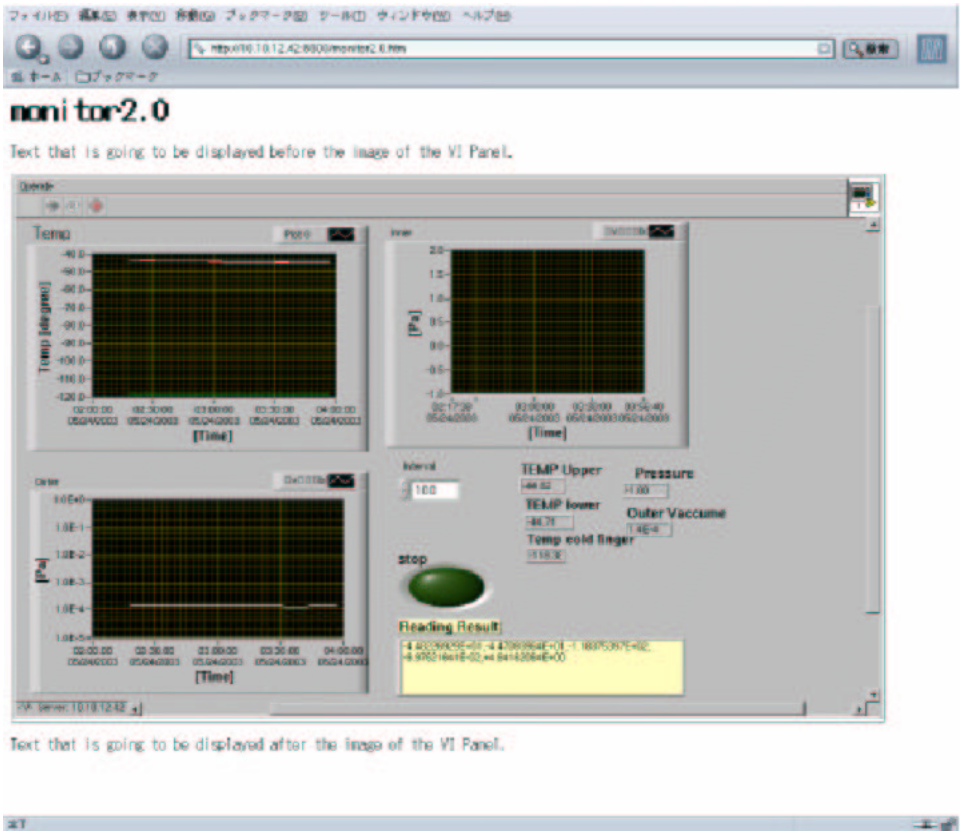

Figure 6.17: Display of the housekeeping data on the Web site.

6.9 Calibration

6.9.1 PMT gain

The gain of PMT were measured by using LED light from optical fibers during the experiment. Fig6.18 illustrates the PMT gain calibration system. The optical fiber were fixed on beside both top and bottom of the PMTs. The spectra of photoelectron is shown in Fig6.20. In this case, the gain of PMT is $1.91 \pm 0.02 \times 10^7$. The Poisson distribution smeared with the Gaussian distribution was used to derive the single photoelectron peak.

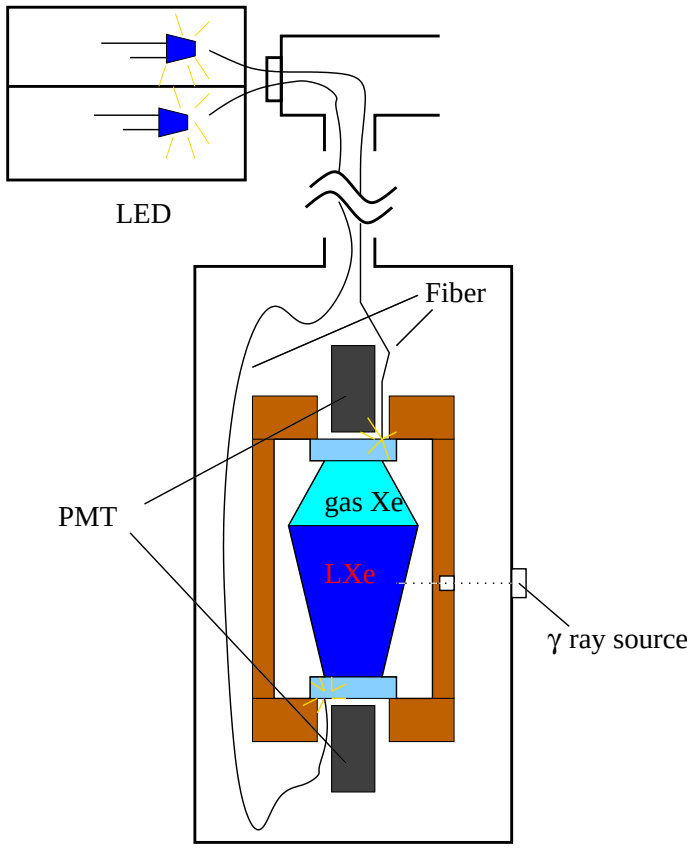

Figure 6.18: PMT gain calibration using LED light.

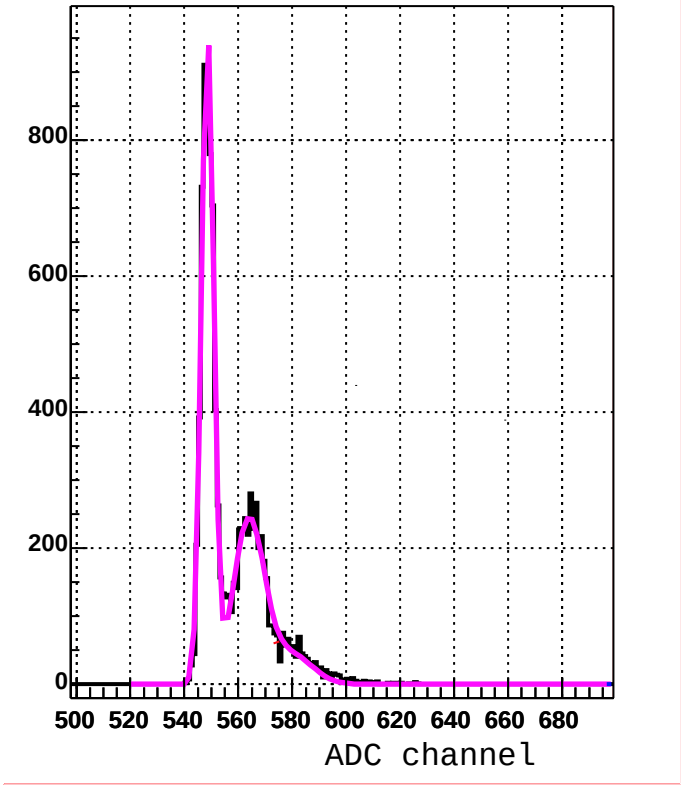

Figure 6.19: PMT gain calibration using LED light. The single photoelectron distribution is shown. The Poisson distribution smeared with the Gaussian distribution was used to fit the spectra. The gain of PMT was $1.91 \pm 0.02 \times 10^7$.

6.9.2 Energy calibration

The energy calibration of the detector was carried out by using ^{57}Co gamma ray source at 250V/cm electric field. The detector was exposed by gamma rays from the outside of the detector, the location of the source was illustrated in Fig6.18. Energy resolution σ/E is 13.8$\pm$0.16%. The photoelectron yield of the detector is 2.05$\pm$0.02 phe/keV.

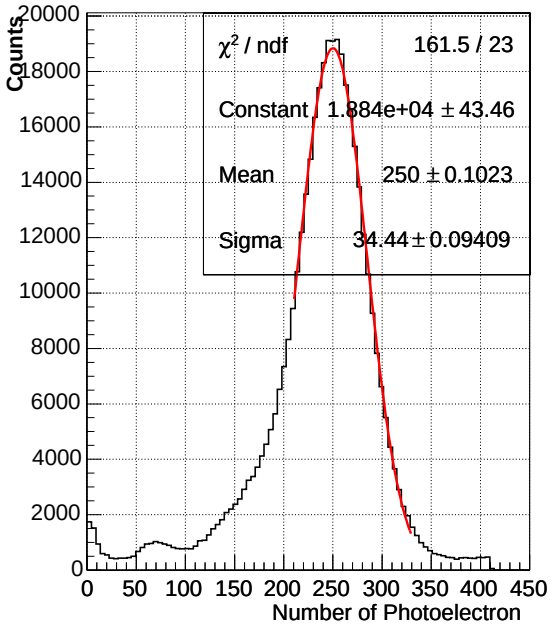

Figure 6.20: Energy calibration with ^{57}Co gamma ray source. The photoelectron yield of the detector was 2.05 ± 0.02.

Chapter 7

Results

7.1 Event selection

7.1.1 Noise rejection

In the case of the low background experiments, the event in the low energy region are dominated by the noise event. For the scintillation detector with PMTs, the noise events commonly come from,

- the PMTs with fast photoelectron pulses,
- the PMT windows and MgF_2 windows as Cerenkov light.

To select real events, the partial gate method was carried out for each PMT. Fig.7.1 shows the typical pulse shape recorded by the 500MHz FADC. In this analysis, the ratio $R(40:90)$ of the integration of 40nsec (F(40nsec)) to 90nsec (F(90nsec)) was used. The R(40:90) plotted as a function of energy is shown in Fig.7.2. The upper one was the measurement of the background run in Kamioka mine and the lower one is the irradiated gamma rays by ^{57}Co source. The noise pulse is clearly seen around the $R(40:90) \sim 0.9$.

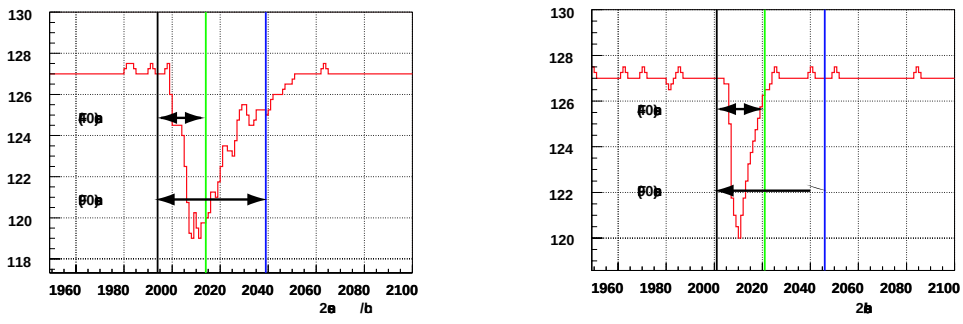

Figure 7.1: Typical signal from PMT. The real signal (left) and the noise one (right) are distinguished by the partial gate method.

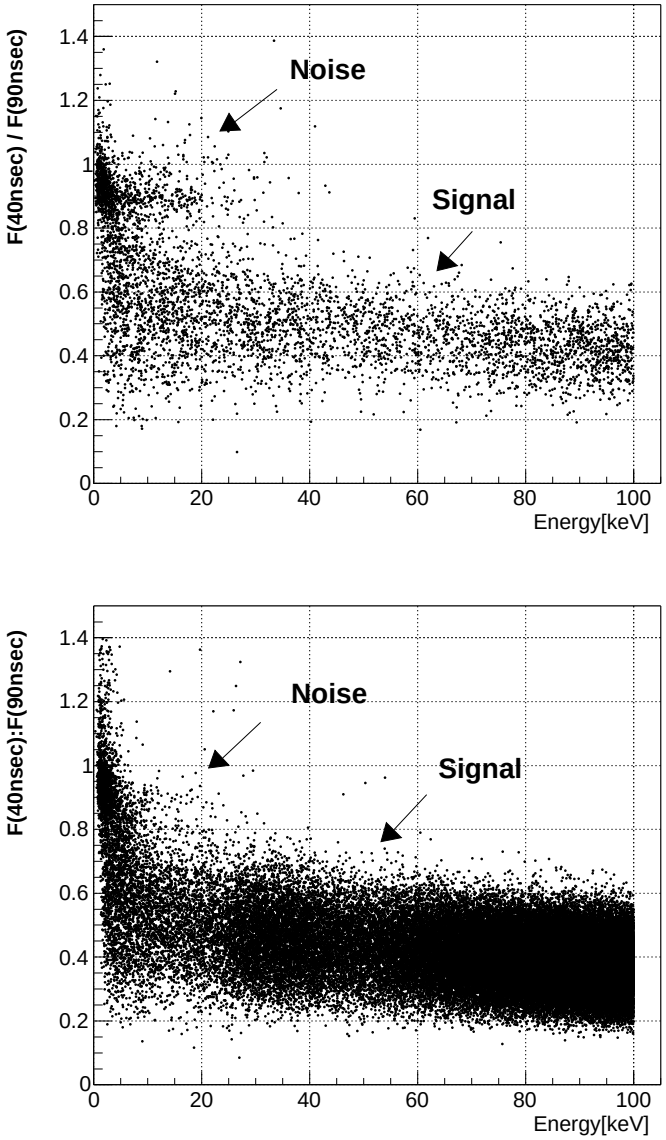

Figure 7.2: Ratio of F(40nsec)/F(90nsec) as a function of energy. The upper distribution was obtained by the measurement of the background run in Kamioka mine, the lower one by irradiating ^{57}Co gamma ray source from outside the detector.

To evaluate the detection efficiency due to a cut using this method, the reference pulse data from ^{57}Co source run was used in each energy bin for each PMT. Fig7.4 shows the $R(40:90)$ distribution in each energy bin from 0 to 11 keV. The distribution of $R(40:90)$ from the background is normalized to the source run in this figure. These efficiencies are summarized in Fig7.5. Fig.7.6 shows the energy spectrum of the raw data and the noise cut data.

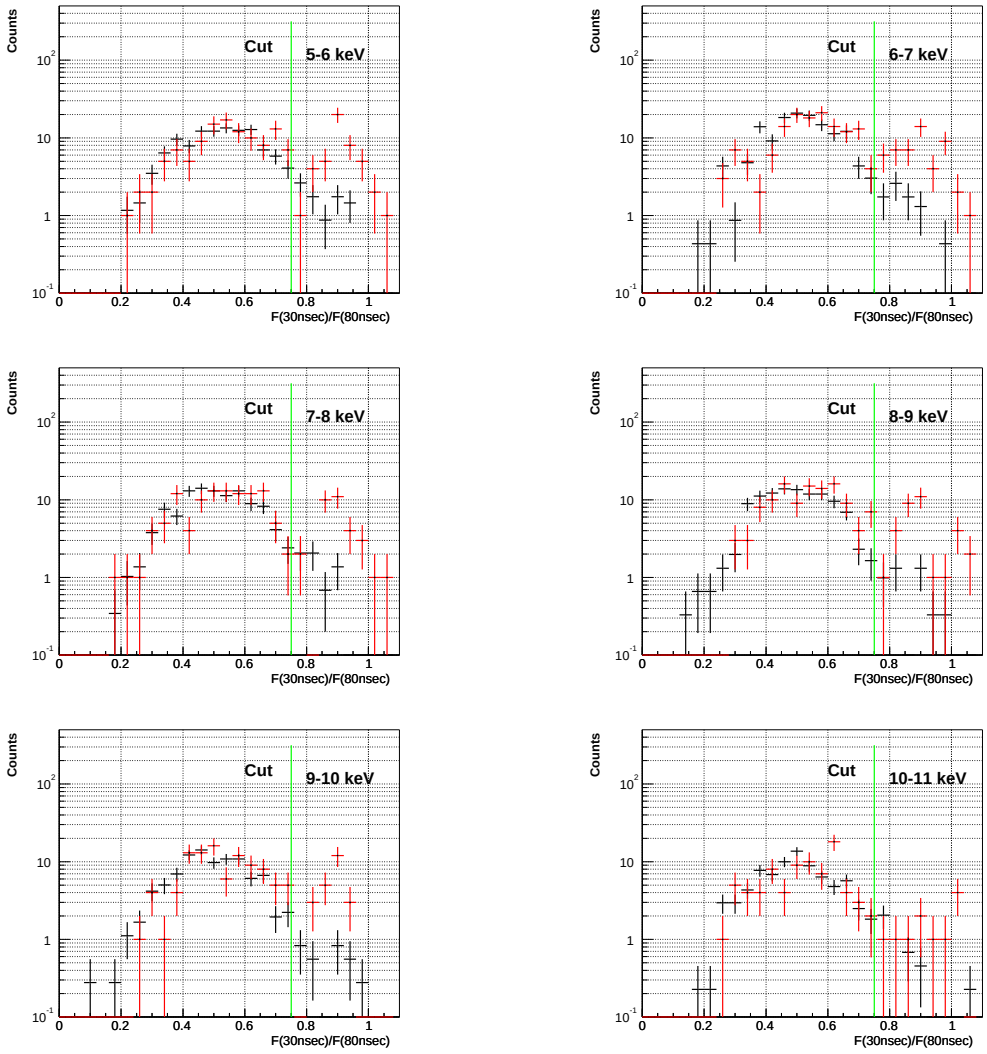

Figure 7.3: Ratio of F(40 nsec) to F(80 nsec) for PMT(U) in each energy bin. Both background run (red line) and source run (black line) are plotted. In this analysis, the event below green line are selected.

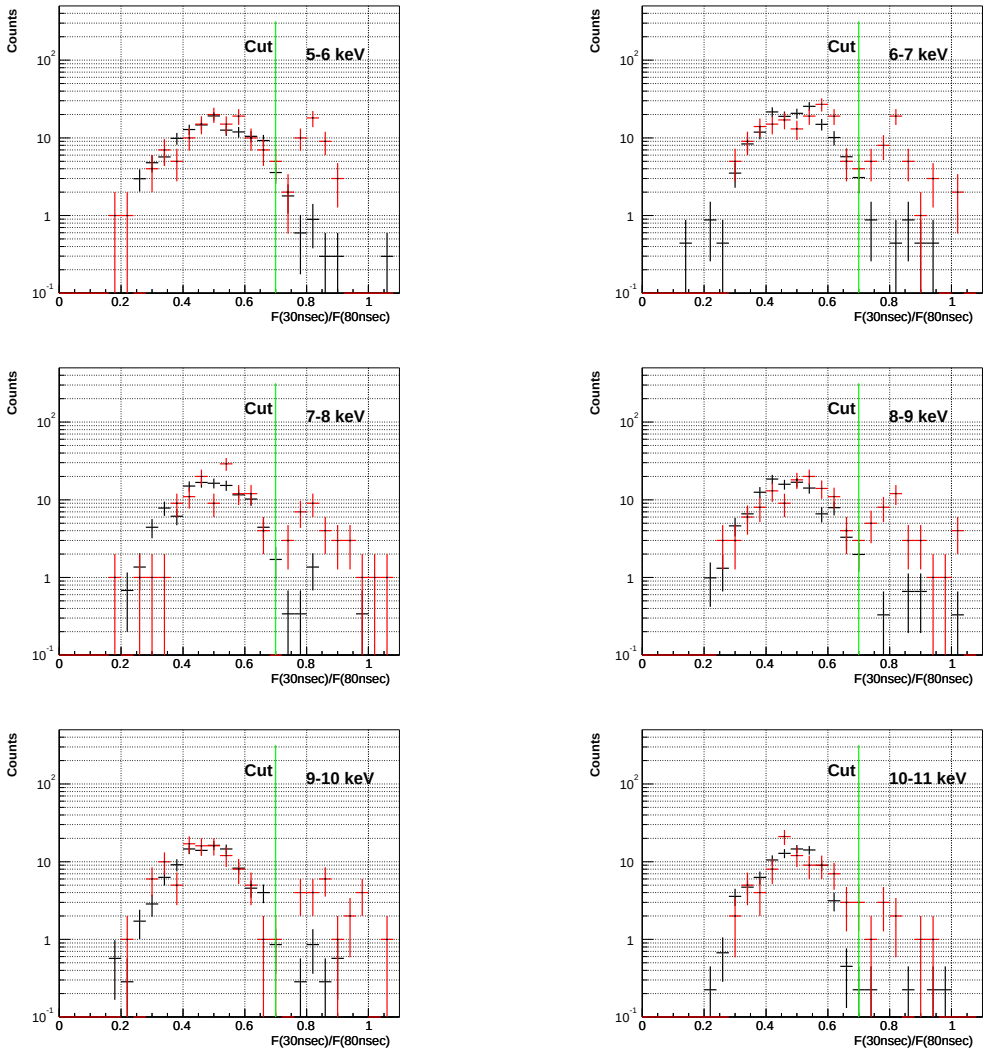

Figure 7.4: Ratio of F(40 nsec) to F(90 nsec) for PMT(U) in each energy bin. Both background run (red line) and source run (black line) are plotted. In this analysis, the event below green line are selected.

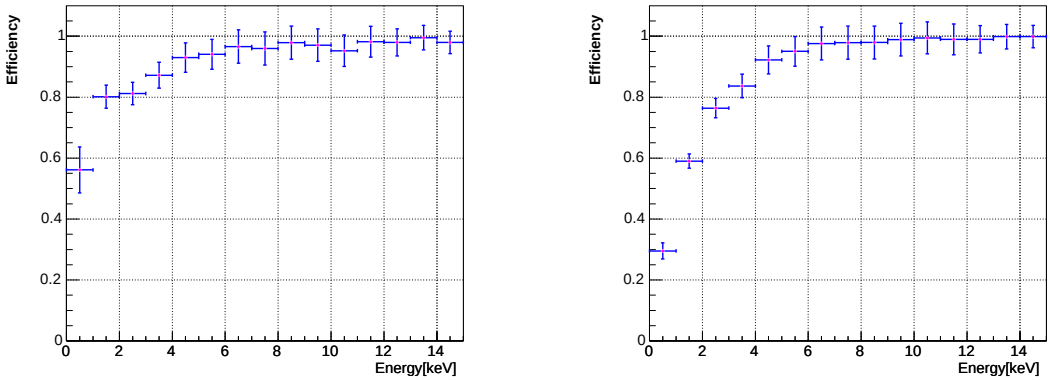

Figure 7.5: Ratio of F(40 nsec) to F(80 nsec) for PMT(U) in each energy bin. Both background run (red line) and source run (black line) are plotted. In this analysis, the event below green line are selected.

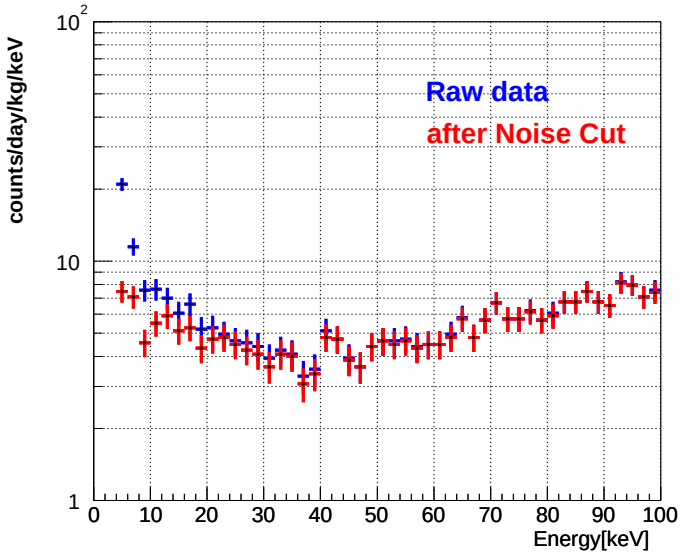

Figure 7.6: The energy spectrum of the raw data (blue) and the noise cut data (red).

7.1.2 Background rejection

Fig.7.7 shows S2 plots as a function of the energy S1. The black dot is the events that both top and bottom PMT have S2 signal and the red one is the rest. The projection to energy axis of these plots are shown in Fig.7.8.

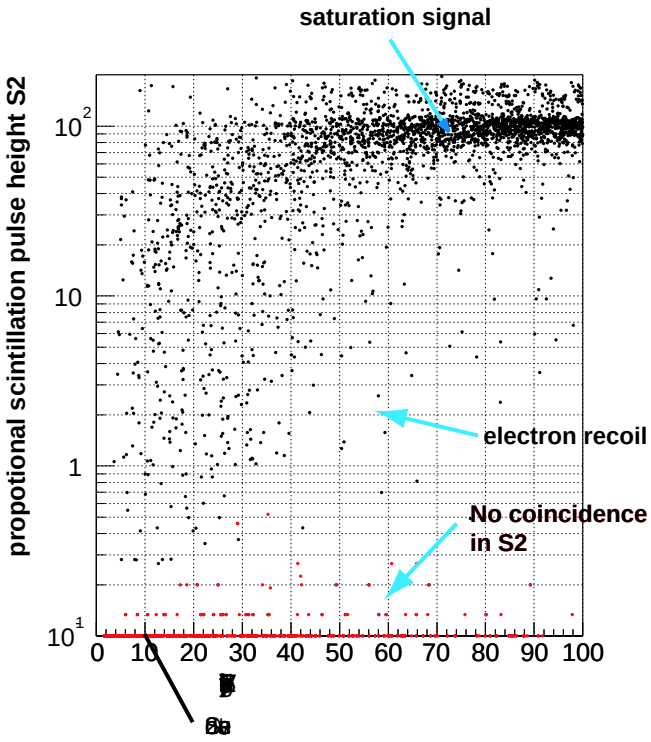

Figure 7.7: Proportional scintillation (S2) signal as a function of direct scintillation (S1) signal. 6.35 days live time and 3349 plots.

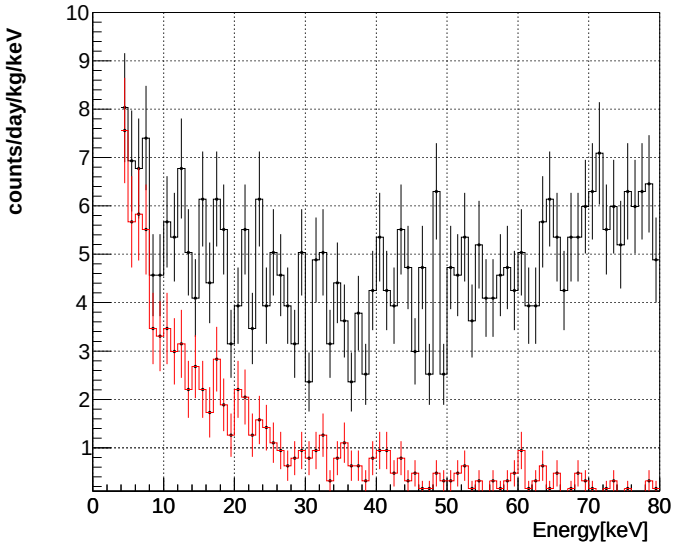

Figure 7.8: The energy spectrum of this experiment with the double phase Xe detector at Kamioka mine. This is projection to the direct scintillation axis of Fig.7.7.

7.2 WIMP-nucleon limits

The limits of the WIMP-nucleon cross section $\sigma_{\chi-p}$ as described in Section3.3 with the astrophysical and nuclear parameters listed in Table 7.1.

In these results, the same manner as presented in Ref.[32, 20] was used. We conservatively assumed that all the signals are caused by the neutralino and compared the obtained spectra shown in Fig.7.8 to the spectra expressed as Eq. 3.19 smeared with the resolution of the detector for a given WIMP mass M_χ and nucleus component $N(=\mathrm{Xe})$. The spectrum smeared with the resolution σ is written as

$$\frac{dR(\sigma)}{dE_R} = \int_0^{\inf} g(E_R - E)\frac{dR}{dE}dE, \tag{7.1}$$

$$g(x) = \frac{1}{\sqrt{2\pi}\sigma}\exp(-\frac{x^2}{2\sigma^2}) \tag{7.2}$$

where $g(x)$ is the Gaussian distribution. The 90% confidence level upper limit count rate of each energy bin of the spectra, $S_{n,k}$ is obtained by

$$S_{n,k}^{90\%\mathrm{CL}} = N_{n,k}^{90\%CL}/t/\Delta E/m/\mathrm{eff}(\mathrm{E_R}) \tag{7.3}$$

where $n(=1)$ denotes the detector number, k does the energy bin number, $S_{n,k}^{90\%\mathrm{CL}}$ is the 90% confidence level upper limit count rate, $N_{n,k}^{90\%\mathrm{CL}}$ is the 90% confidence level upper limit of the observed number of events. $N_{n,k}^{90\%\mathrm{CL}}$ is defined by the observed events $N_{n,k}$ as

$$N_{n,k}^{90\%\mathrm{CL}} = N_{n,k} + 1.28\cdot\sqrt{N_{n,k}} \tag{7.4}$$

for $N_{n,k} > 10$. For $N_{n,k} \leq 10$, the Poisson upper limits listed in Table 7.2 were used. Then,

$$S_{n,k}^{90\%\mathrm{CL}}\Delta E = \int_{\Delta E}\frac{dR(\sigma)}{dE_R}f_N F^2(E_R)dE_R \tag{7.5}$$

was used to derive the upper limit of the cross section of the WIMP-nucleus interaction, where f_N is the mass fraction of the nucleus. The lowest value among the obtained limits all n,k for a given WIMP mass M_χ and nucleus N is adopted as the combined limit $\sigma_{\chi-N}$. Fig.7.9 shows the calculated trigger efficiency for this experiment in this simulation. The detail of this simulation was described in Section5. The refractive index of the Quartz is 1.56.To evaluate this efficiency, the number of photons, which follow the Poisson distribution, are produced in the whole of detector. The threshold is set to one photoelectron in each PMTs.

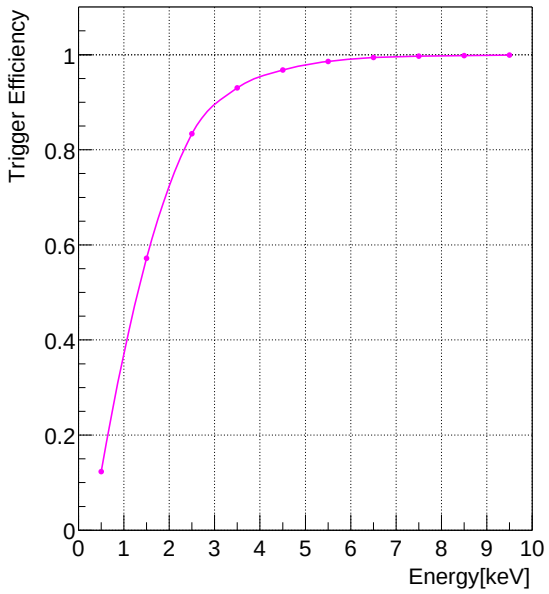

Figure 7.9: Trigger efficiency as a function of energy for this experiment. The thresholds are set to 1 photoelectron in each PMT in this simulation.

Dark Matter density ρ_D	0.3 GeV/c^{-2}
Dispersion of Dark Matter velocity v_0	220km/s
Earth(Target) velocity v_E	232km/s
Local Galactic escape velocityv_{esc}	650km/s
Quenching Factor	0.263
$\lambda^2_{p,Z}J(J+1)(^{129}\mathrm{Xe})$	0.232
$\lambda^2_{p,Z}J(J+1)(^{131}\mathrm{Xe})$	0.057

Table 7.1: Astrophysical and nuclear parameters used to calculate the limit.

N	ν_{upper} 90% CL
0	2.30
1	3.89
2	5.32
3	6.68
4	7.99
5	9.27
6	10.53
7	11.77
8	12.99
9	14.21
10	15.41

Table 7.2: Upper limits for the mean ν of a Poisson variable given N observed events in the absence of background, for confidence levels of 90%.[102]

7.2.1 $\sigma_{\chi-\text{p}}$ Limits

To compare with the results of other experiments, which used different target materials, the WIMP-nucleus cross section limits are normalized to the limits for a single proton and this manner to evaluate the limits was described in Section3.3. Fig7.10 and Fig7.11 shows the WIMP-nucleus cross section with other experiments in the spin independent case and in the spin dependent, respectively. The results of LiF and NaF experiment by Tokyo group were derived from Ref.[103].

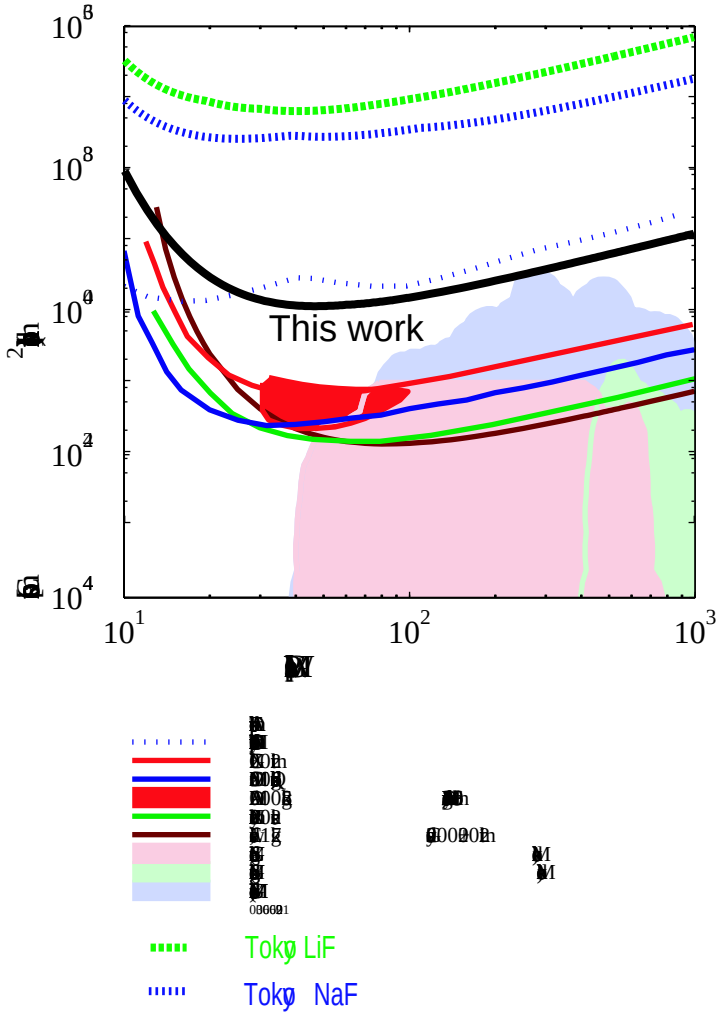

Figure 7.10: $\sigma^{\mathrm{SI}}_{\chi-\mathrm{p}}$ limits as a function of M_χ. The region above the curves are excluded. The result at 90% C.L. from this experiment is shown in black line together with other experiments. This figure was taken from Ref.[31].

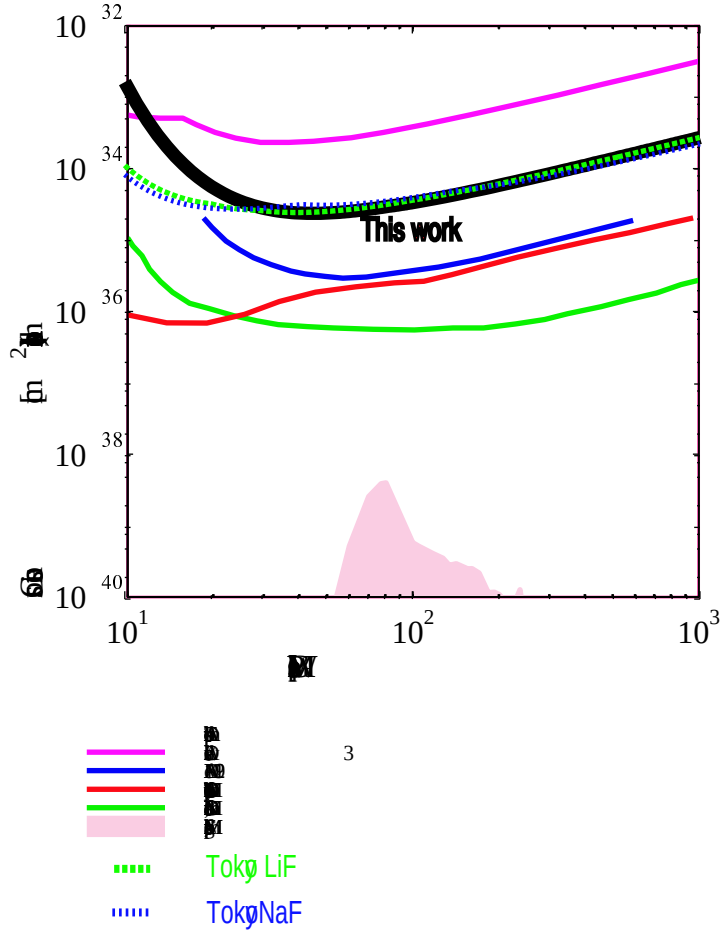

Figure 7.11: $\sigma^{SD}_{\chi-p}$ limits as a function of M_χ. The region above the curves are excluded. The result at 90% C.L. from this experiment is shown in black line together with other experiments. This figure was taken from Ref.[31].

Chapter 8

Discussion

To understand the background component is very important to find the origin of the background and to reduce it. This understanding is also very useful the designing of the next phase detector. In this chapter, the component of the background was estimated by using the radioactive value measured by HPGe and Monte Calro simulation.

8.1 Ambient gamma rays

The ambient gamma flux at Kamioka Observatory is reported as 0.71 gamma/sec/cm^{-2} in 500 - 3000 keV range[95]. The effect of lead shield are calculated by GEANT3 simulation tool.

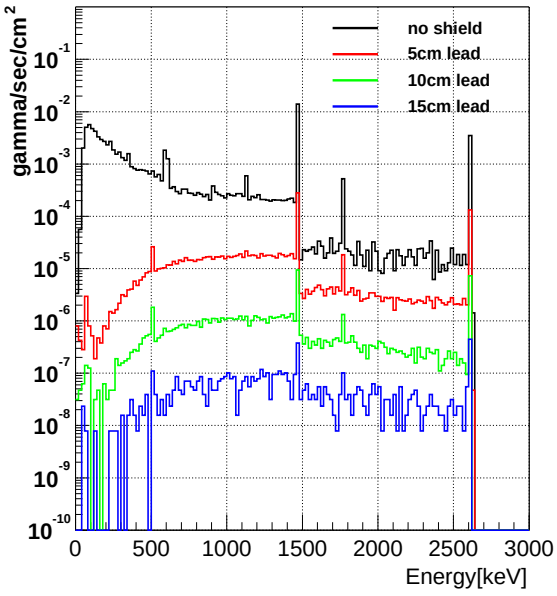

Figure 8.1: The effect of lead shield as a function of thickness .

Fig.8.1 shows gamma ray spectrum without shield(corresponding to ambient gamma flux), 5cm thickness of lead, 10cm and 15cm. From this result, the gamma flux is reduced 3 orders of magnitude in the 500-3000keV energy range. The contribution of ambient gamma to the detector is estimated less than 200 count/day and is negligible to our current result.

8.2 Background from materials

The contribution of the detector materials to the result is discussed here. High radioactive materials, for instance a glass, a ceramic ..., are not used or located far from the detector. To understand the background quantitatively, the radioactivities of the detector materials were measured by HPGe detector in Kamioka mine (see Appendix A). The values of PMT and its base are listed again here in Table8.1 and that of all materials near the detector, O.F.H.C copper and lead which are mainly used for the shields are listed in Table8.2 and Table8.3. Fig.8.2 shows the location of each materials. Indium and O-ring are used for the vacuum sealing, Acrylic for PMT holder. Nine resistors divide the high voltage for shaping rings. In this simulation, "DECAY4" is used for event generator[93]. The energy resolution is smeared by the calibration data. In this simulation, the value of activities were assumed to be the center values or the upper limits.

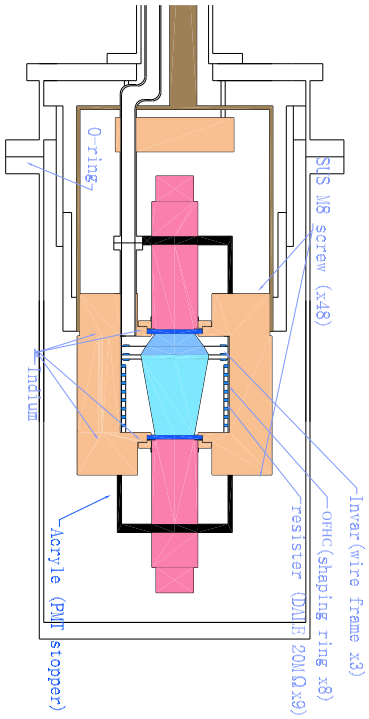

Figure 8.2: The location of materials.

	U chain [Bq/PMT]	Th chain [Bq/PMT]	^{40}K[Bq/PMT]	^{60}Co [Bq/PMT]
ZK0667	5.0×10^{-2}	1.3×10^{-2}	6.1×10^{-1}	$\langle 1.8 \times 10^{-3}$
Base	1.1×10^{-1}	2.7×10^{-2}	4.1×10^{-2}	$\langle 3.5 \times 10^{-4}$
R8778Q	$1.8 \pm 0.2 \times 10^{-2}$	$6.9 \pm 1.3 \times 10^{-3}$	$1.4 \pm 0.2 \times 10^{-1}$	$5.5 \pm 0.9 \times 10^{-3}$
Base	1.5×10^{-3}	1.8×10^{-3}	1.0×10^{-4}	-

Table 8.1: The radioactivities of PMT and its Base.

	U chain [Bq/kg]	Th chain [Bq/kg]	^{40}K[Bq/kg]	^{60}Co [Bq/kg]
SUS (outer)	$<7.6\times10^{-3}$	$<1.0\times10^{-2}$	$<6.9\times10^{-2}$	$1.5\pm0.63\times10^{-2}$
Resistor (Shaping Ring)	1.2 ± 0.24	1.1 ± 0.53	2.6 ± 0.16	$<8.9\times10^{-2}$
PTFE Teflon	$<4.1\times10^{-3}$	$<6.5\times10^{-3}$	$<3.9\times10^{-2}$	$<2.5\times10^{-3}$
Acrylic	$<6.4\times10^{-2}$	$<9.0\times10^{-2}$	$(5.9\pm5.6)\times10^{-1}$	$<3.6\times10^{-2}$
O-ring	$(8.4\pm0.8)\times10^{-1}$	$<7.5\times10^{-2}$	2.0 ± 0.4	$<1.6\times10^{-2}$
Indium	$7.5\pm4.4\times10^{-2}$	$7.1\pm6.7\times10^{-2}$	$<4.0\times10^{-1}$	$<2.5\times10^{-2}$
Invar	$<9.3\times10^{-3}$	$<1.6\times10^{-2}$	$1.4\pm1.2\times10^{-1}$	$<6.7\times10^{-3}$

Table 8.2: The radioactivities of materials.

	U chain [Bq/kg]	Th chain [Bq/kg]	^{40}K[Bq/kg]	^{60}Co [Bq/kg]	^{210}Pb[Bq/kg]
O.F.H.C	$<3.2\times10^{-4}$	$<8.3\times10^{-4}$	$<6.1\times10^{-3}$	$<2.5\times10^{-4}$	-
Lead	$<4.1\times10^{-3}$	$<6.5\times10^{-3}$	$<2.9\times10^{-2}$	$<1.6\times10^{-4}$	$(2.6\pm0.4)\times10^{2}$

Table 8.3: The radioactivities of O.F.H.C and lead. They are used for the vessel of LXe and the shields.

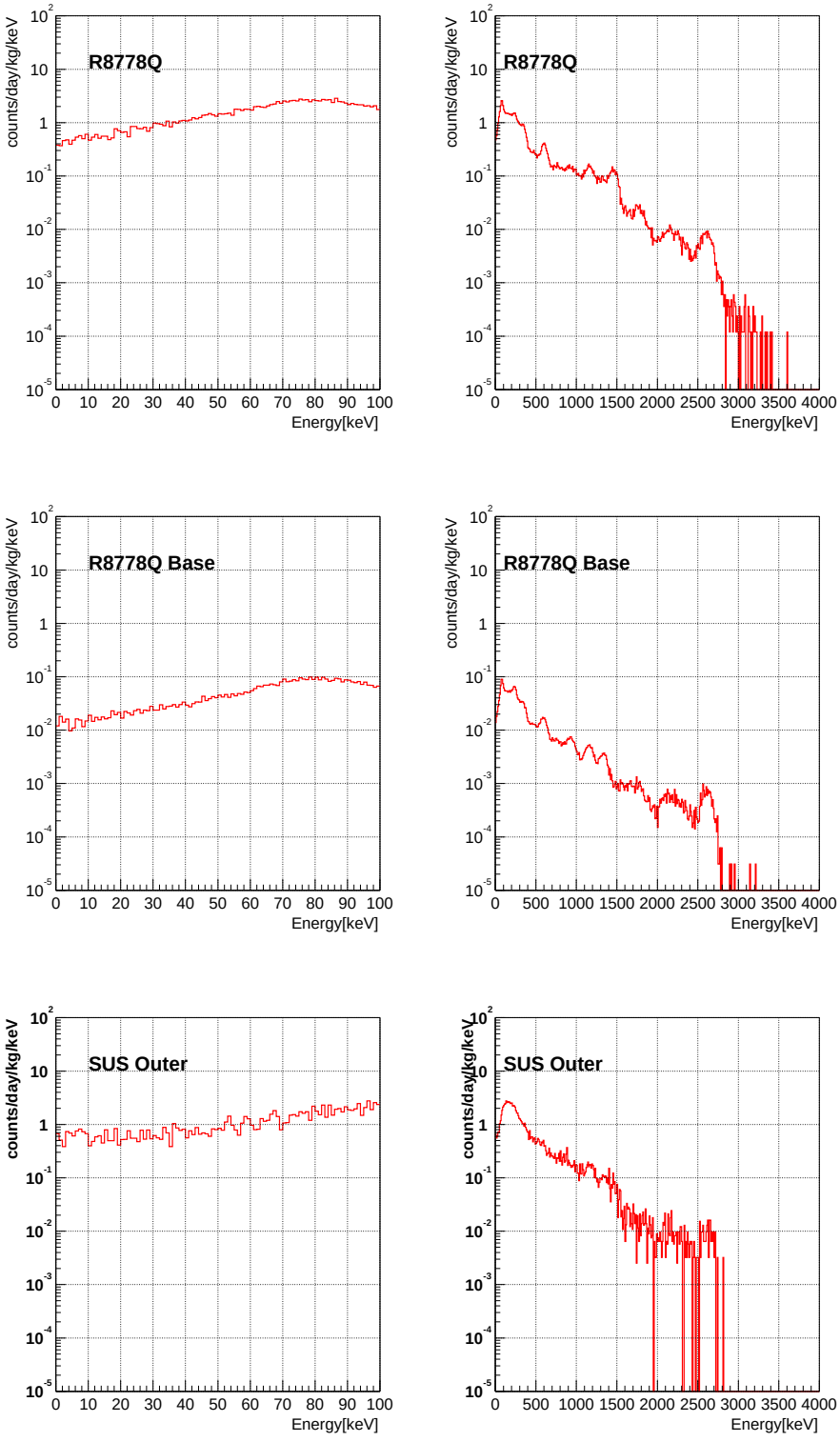

Figure 8.3: Background estimated by Monte Calro Simulation

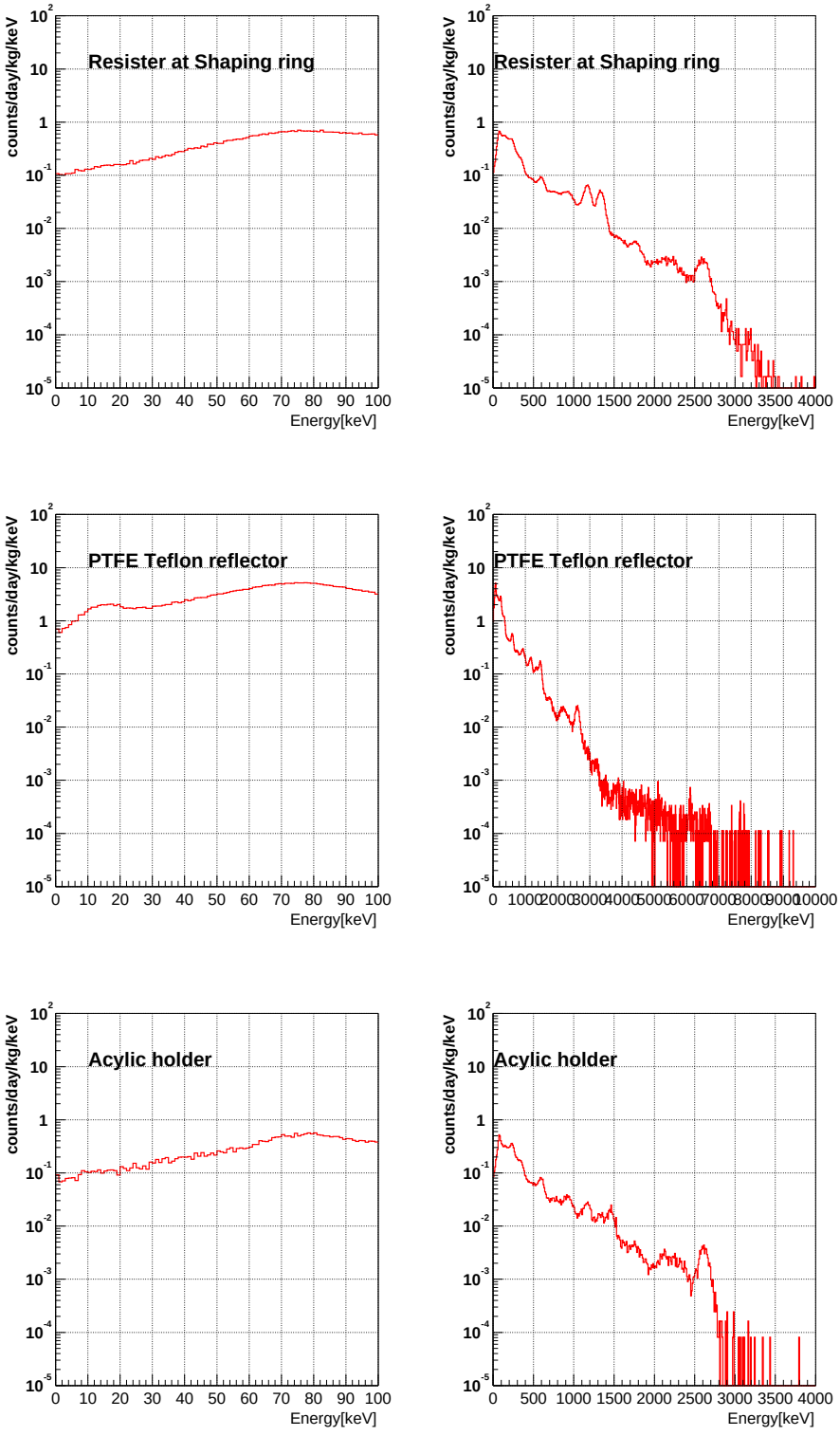

Figure 8.4: Background estimate by Monte Calro Simulation

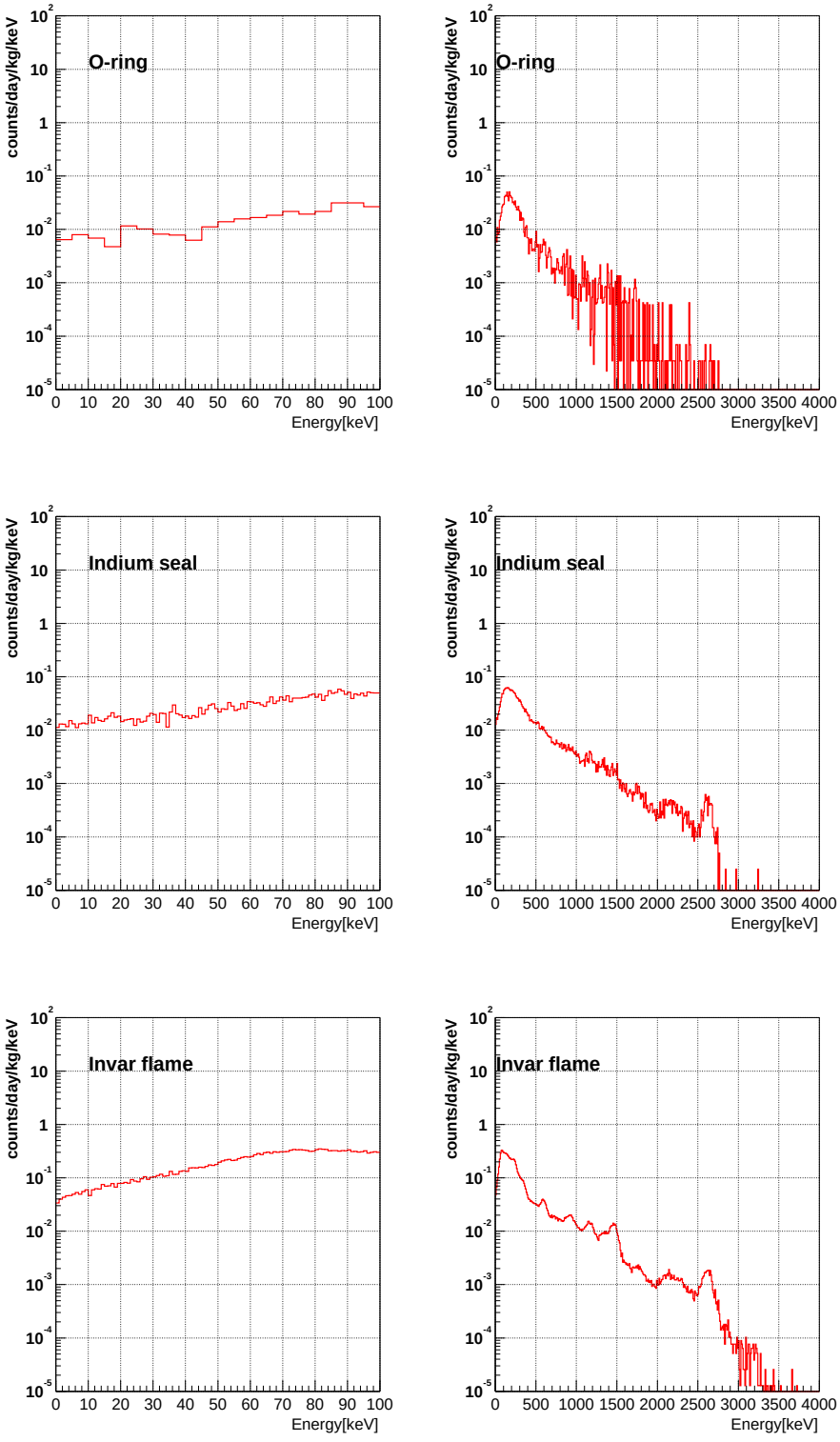

Figure 8.5: Background estimate by Monte Calro Simulation

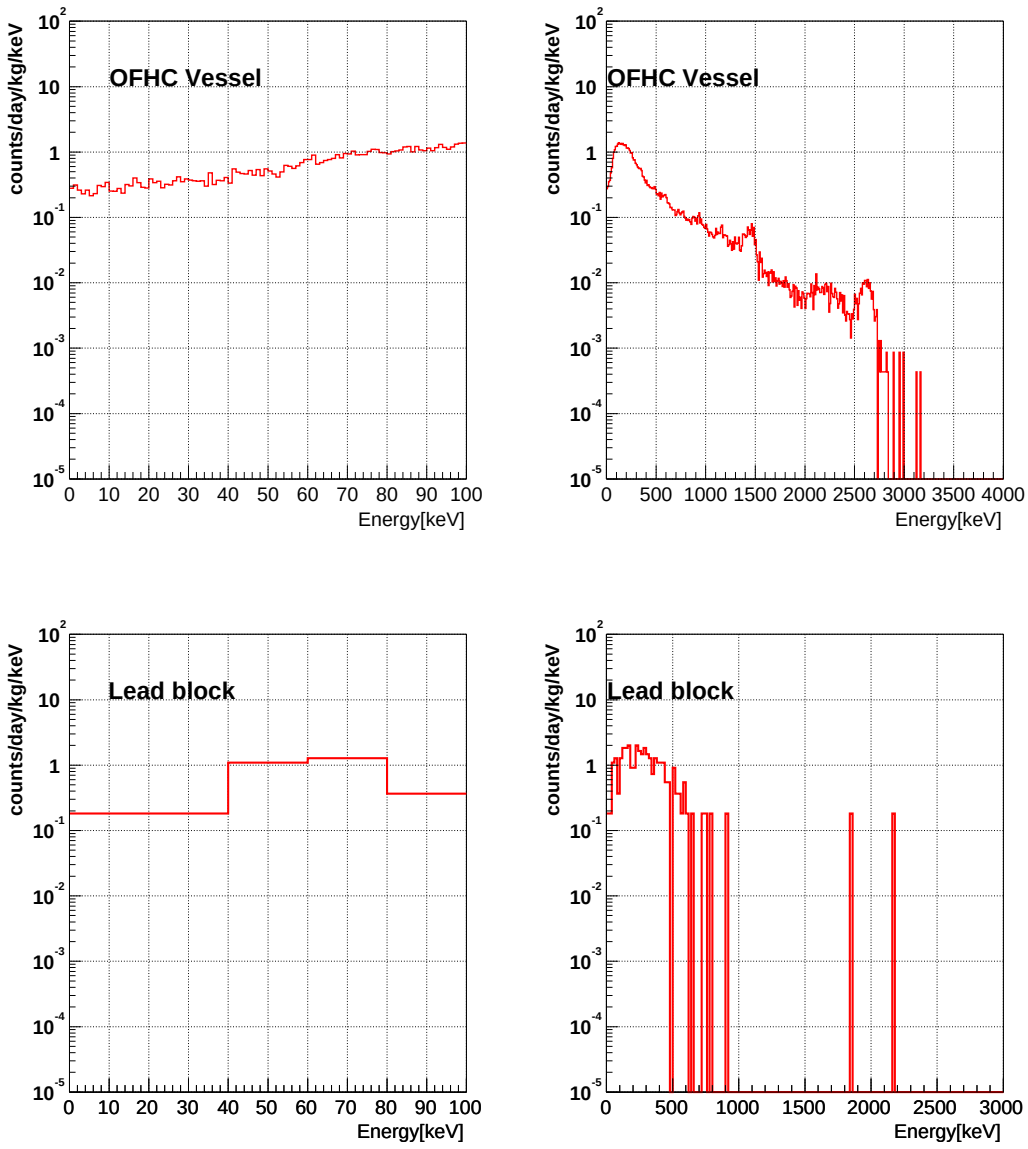

Figure 8.6: Background estimate by Monte Calro Simulation

8.3 Background from ^{39}Ar, ^{42}Ar and ^{85}Kr

Normally, Ar and Kr remain in a commercial gas Xe. The radioactive isotopes of noble gases are discussed here. ^{39}Ar and ^{42}Ar are produced in spallation reactions, electromagnetic interactions with cosmic muons, or nuclear weapon test, ^{85}Kr is formed in a nuclear reactor as a waste product of the fission process. As listed in Table 8.4, because of the very long half lives, decay energies and decay modes of these nuclide, they can be can be important sources of background in a large volume a noble gas based detector. For ^{42}Ar, the beta decay of the ^{42}K daughter isotope ($T_{1/2}$ = 12.36h) has a maximum electron energy of 3.52 MeV (Fig.8.7). The ^{39}Ar concentration of ^{39}Ar in atmospheric argon is measured, and the results are ^{39}Ar/Ar = 8.1×10^{-16}[96], that of ^{42}Ar is ^{42}Ar/Ar $< 6\times10^{-21}$[97]. The atmospheric ^{85}Kr concentration was monitored since 1979 at University Gent in Belgium[98] and since 1995 at MRI in Japan[99]. They reported that ^{85}Kr concentration is $\sim$ 1 Bq/m^3 in the end of 1900, this is equivalent to ^{85}Kr/Kr = 1.8×10^{-11}. Ar and Kr usually remain about 10 ppm in gas Xe which give about 5 ^{85}Kr decays/(1kg Xe), 3.1×10^{-6} ^{39}Ar decays/(1kg Xe) and 1.8 ^{42}Ar decays/(1kg Xe). From these estimates, ^{85}Kr can be problem for background, we used Kr free Xe (10ppb) in this experiments. Fig8.8 shows the energy spectrum from 85Kr in the cases of 10ppm and 10 ppb Kr in Xe.

Isotope	half life[years]	Q value[keV]	abundance
^{39}Ar	269	565	8.1×10^{-16} ^{39}Ar/Ar
^{42}Ar	32.9	600	$< 6\times10^{-21}$ ^{42}Ar/Ar
^{85}Kr	10.7	687	$\sim 1.8\times10^{-11}$ ^{85}Kr/Kr
			1.1×10^{-11} ^{85}Kr/Kr [100]

Table 8.4: ^{85}Kr, ^{42}Ar and ^{39}Ar.

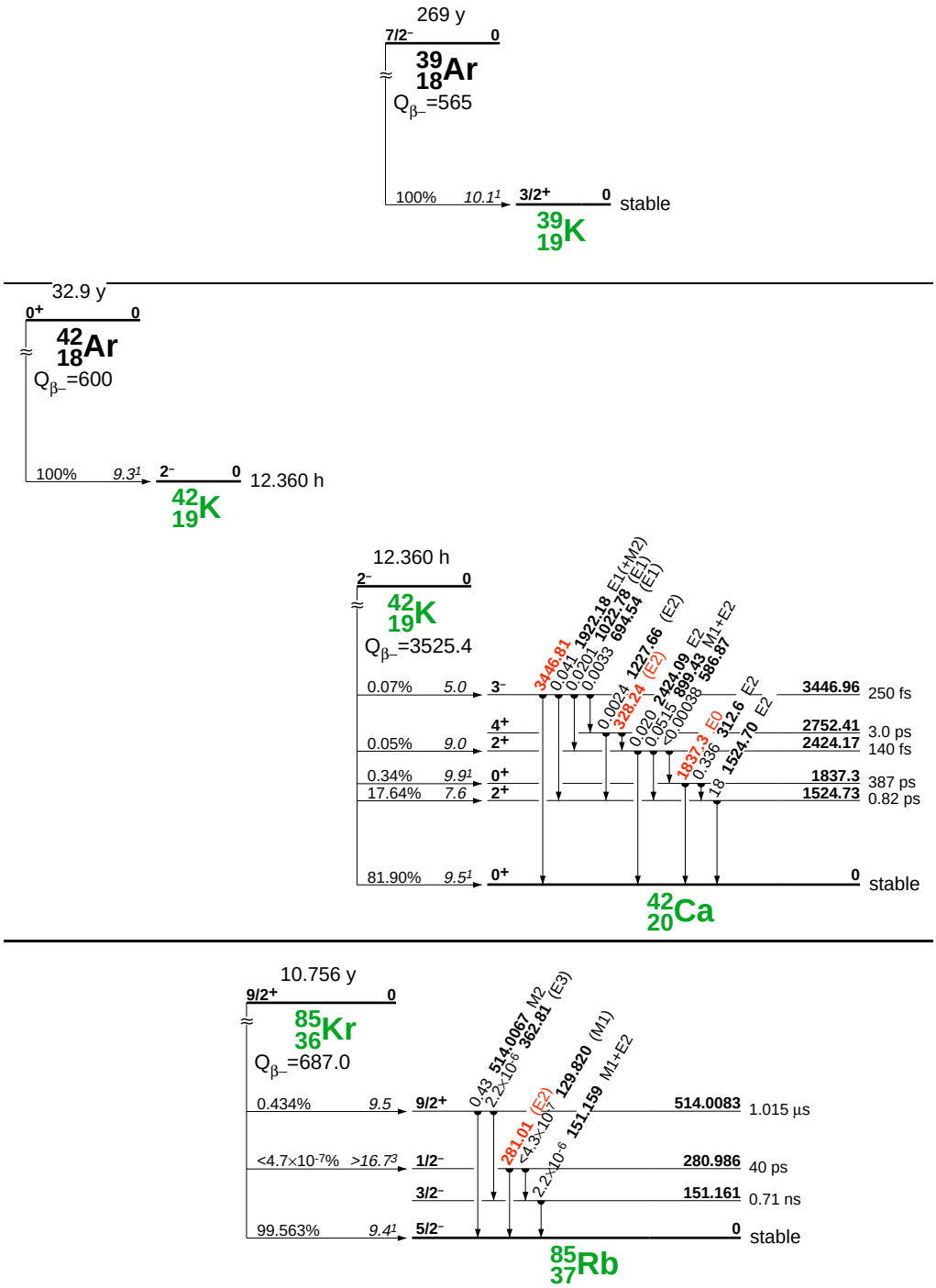

Figure 8.7: The decay scheme of ^{39}Ar, 42Ar and ^{85}Kr[88].

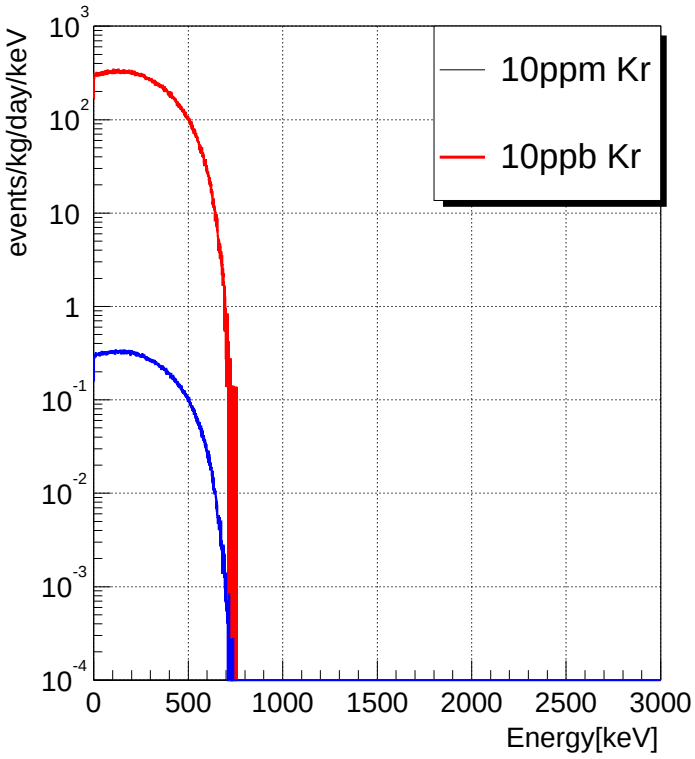

Figure 8.8: The calculated energy spectrum of ^{85}Kr in the case of 10ppm and 10ppb Kr.

8.4 Background from neutron

8.4.1 ^{3}He proportional counter

The neutron flux was measured using ^{3}He proportional counter at Kamioka Observatory. Neutron classification by energy is followings:

- Thermal neutron
  $E_p < 0.5$ eV
- Epi-thermal neutron
  0.5 eV $< E_p <$ 500 keV
- Fast neutron
  $E_p >$500 keV

For the energy spectrum of neutron, $1/E$-law [94] was assuming as,

$$N(E) = \frac{A}{E} \tag{8.1}$$

where E is neutron energy, N is neutron flux and A is constant.

The spec of this counter is listed in Table8.5. The applied high voltage is +1159[V].

Diameter	5.16cm
Length	43.5cm
Pressure of ^{3}He	3 atm
Thermal neutron sensitivity	102cps/(n cm^{-2}s^{-1})

Table 8.5: Spec of ^{3}He counter

8.4.2 Measurement and results

Fig.8.10 shows the energy spectrum of the ^{3}He counter in Kamioka mine. 0.764 MeV peak was clearly seen in this figure. Table 8.6 shows the measurement result of the neutron flux in Kamioka mine. In the case with shield, the value of the thermal and fast neutron flux was less than $\langle\ 2.55\times10^{-7}$ and $\langle\ 6.40\times10^{-7}$, respectively.

	Thermal[n cm^{-2}s^{-1}]	Epi[n cm^{-2}s^{-1}]	Fast[n cm^{-2}s^{-1}]
Ambient	$8.32\pm0.90\times10^{-6}$	$1.66\pm0.38\times10^{-5}$	$3.60\pm0.83\times10^{-6}$
with shield	$\langle\ 2.55\times10^{-7}$	$\langle\ 2.95\times10^{-6}$	$\langle\ 6.40\times10^{-7}$

Table 8.6: The neutron flux in Kamioka mine and inside the shield.

Figure 8.9: ^{3}He proportional counter.

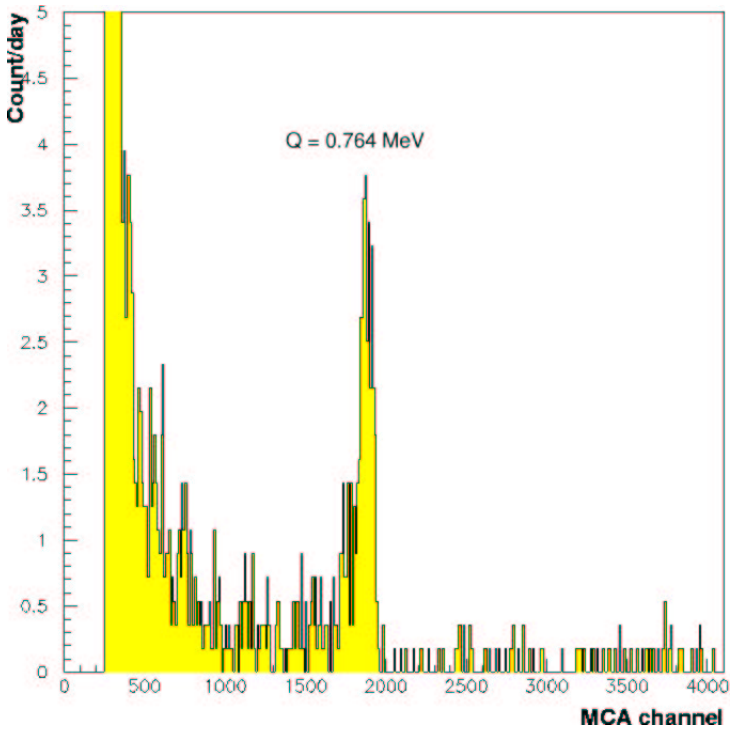

Figure 8.10: The thermal neutron background spectrum by the^{3}He proportional counter.

8.4.3 Fast neutron

The background from the elastic scattering of fast neutron was calculated. Fig.8.11 shows the cross section of elastic scattering n-^{129}Xe, ^{131}Xe, ^{132}Xe[101]. In this calculation, Eq.8.1 was assumed.

The background spectrum with or without shield are shown in Fig.8.12. The fast neutron is the one of the most dangerous background for WIMPs direct search. This background is negligible to the current results, in the future, for further search, we must reduce this background by i.e. Huge Water Tank.

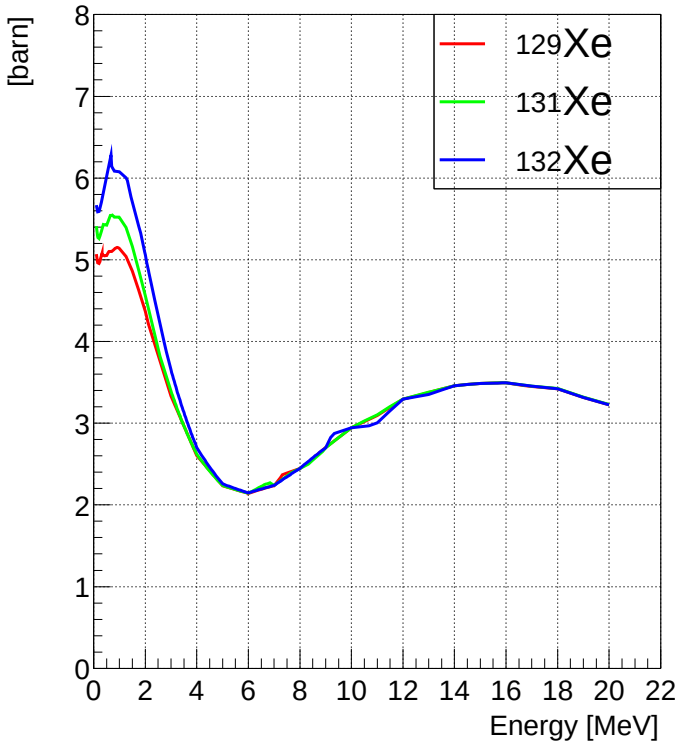

Figure 8.11: The elastic scattering cross section for Xe[101].

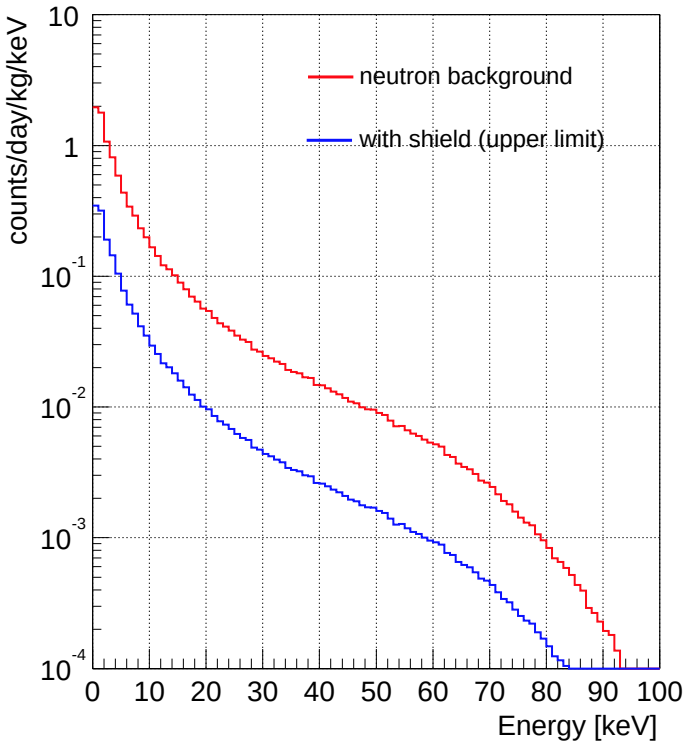

Figure 8.12: Estimated fast neutron background, (red:neutron background , blue:with shield)(q = 0.263)

8.4.4 Thermal neutron

Thermal neutrons are captured by Xe isotopes. Neutron captured Xe isotopes are listed in Table8.7. The longest half life of radioisotope is $\sim$ 36 days. This short half life is advantage to underground physics for low background.

Background produced by thermal neutrons was calculated using the flux in Table.8.5. Fig.8.13 shows the estimated background spectrum from various Xe isotopes (red is total) and Fig.8.14 shows sum of these spectrum with or without shield.

Isotope	cross section[barn]	half life	disintegration mode	Energy(keV)
^{125m}Xe	28	57.0 sec	IT	140.8(γ) 111.8(γ)
^{125}Xe	165	16.9 hour	EC	243.4(γ) 188.4(γ)
^{127m}Xe	0.45	69.2 sec	IT	124.7(γ) 172.4(γ)
^{127}Xe	3.5	36.4 day	EC	375.0(γ) 202.9(γ)
^{129m}Xe	0.48	8.88 day	IT	39.58(γ) 196.6(γ)
^{131m}Xe	0.45	11.8 day	IT	163.9(γ)
^{133m}Xe	0.05	2.19 day	IT	233.2(γ)
^{133}Xe	0.45	5.24 day	β^-	346(β) 81.0(γ)
^{135m}Xe	0.003	15.3 min	IT	526.6(γ)
^{135}Xe	0.265	9.14 hour	β^-	910(β) 249.8(γ)
^{137}Xe	0.26	3.8 min	β^-	4170(β) 3720(β) 455.5(γ)

Table 8.7: The cross section of neutron capture for Xe Isotopes.

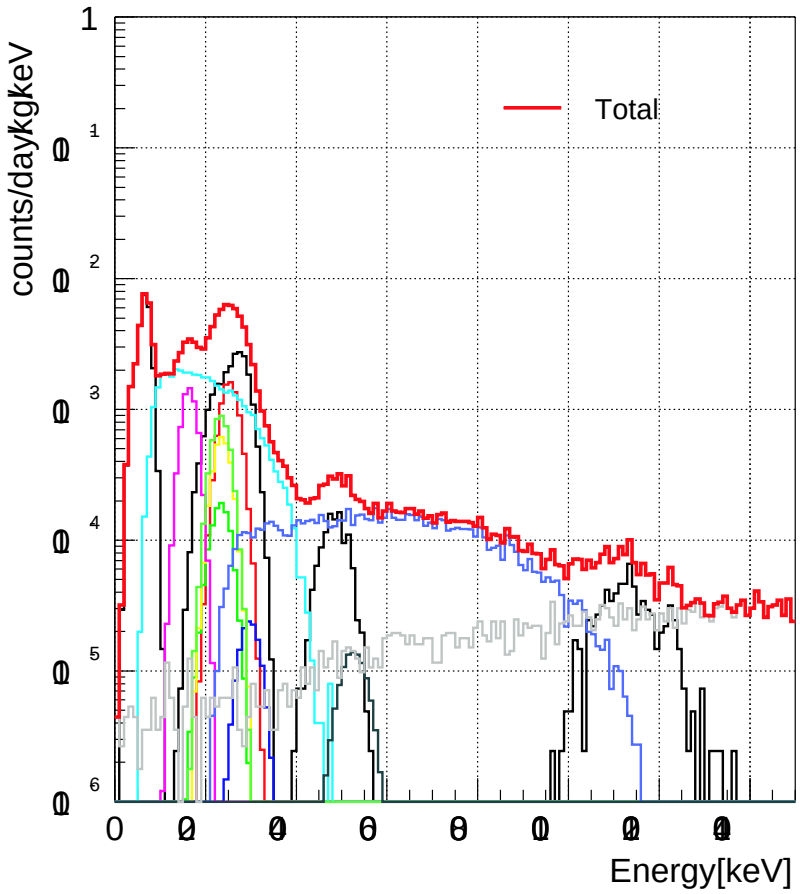

Figure 8.13: Estimated background from thermal neutron. The red line is correspond to the total spectra from , blue:with shield)

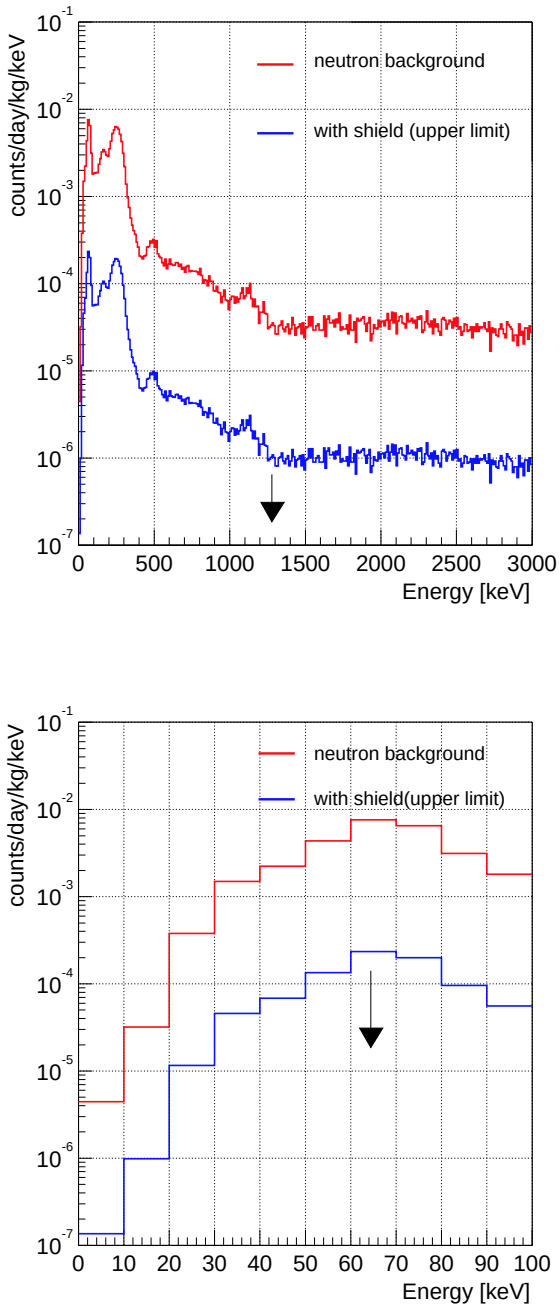

Figure 8.14: Estimated fast neutron background, (red:neutron background , blue:with shield)

8.5 Summary of the Monte Carlo simulation

The results of the background studies are shown in Table8.8. PMT and stainless steel used for the outer vessel, were main component to our data. The stainless steel should be replaced O.F.H.C copper. For the PMT, we will reselect the parts of PMT in the future. The differences of count rate in the low energy region is discussed in Sec.8.5.1.

Source	Rate(10-30keV)[counts/day/kg/keV]	Total events[counts/day/kg]
PMT(R8778Q)	$\mathbf{7.3\times10^{-1}}$	**736**
PMT Base	1.8×10^{-2}	23.6
SUS(outer)	$\mathbf{7.3\times10^{-1}}$	**928**
Resister	1.7×10^{-1}	211
PTFE Teflon	< 1.9	$<$1217
Acrylic	1.2×10^{-2}	144
O-ring	8.9×10^{-3}	12
Indium	1.7×10^{-2}	23
Invar	8.2×10^{-2}	94
O.F.H.C. Copper	$<3.4\times10^{-1}$	$<$473
Lead	$\sim \mathbf{2\times10^{-1}}$	$\sim$ **600**
^{85}Kr	$<3.2\times10^{-2}$	< 138
Radon	$<6.5\times10^{-2}$	< 87
Fast neutron	$<1.4\times10^{-2}$	$<$1.7
Thermal neutron	$<6.3\times10^{-6}$	$<1.2\times10^{-2}$
Simulation total	$\sim$1.2	$\sim$2600

Table 8.8: Summary of the background evaluation compared to the measurement result. The averaged count rate from 10 keV to 30keV and total count rate are shown.

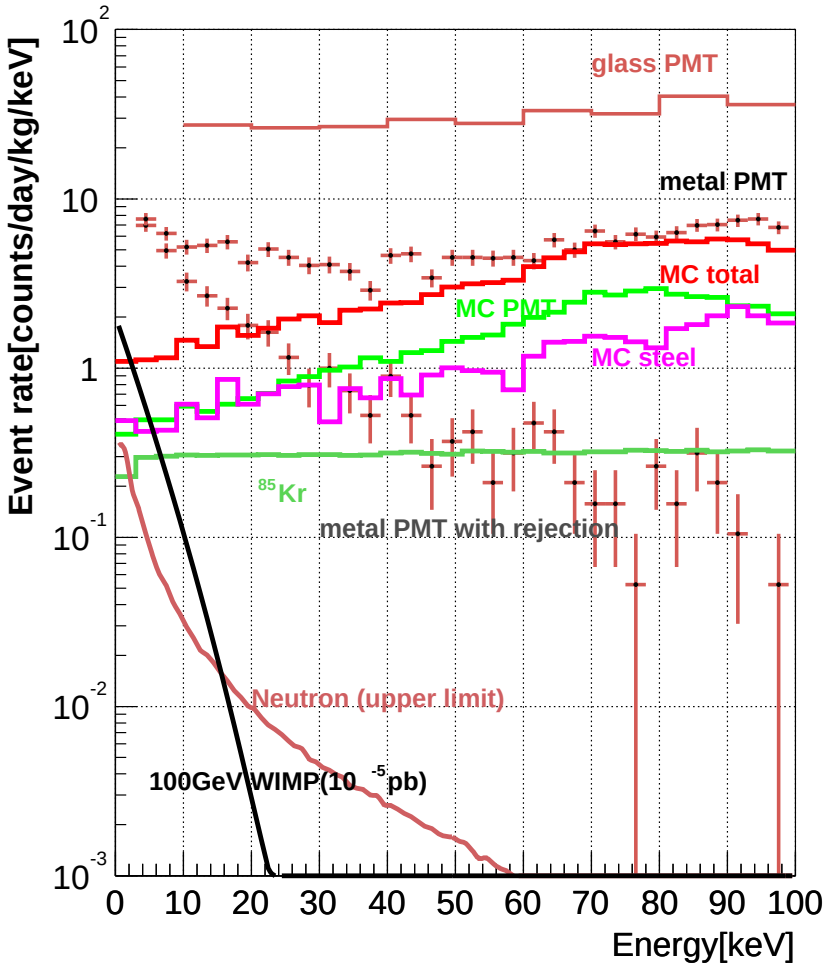

Figure 8.15: Summary of the Monte Calro simulation and experimental data and spectra from WIMP (black). For the spectra for WIMP, $\sigma^{\mathrm{SI}}_{\chi-\mathrm{p}} = 1\times10^{-5}$ pb was assumed.

8.5.1 Anomalous event in low energy region

From Fig.8.15, the simulation and experimental data was consistent in the energy range higher than 40keV, but the low energy region was not. Fig.8.5.1 The rejected event, which have the S2 signal, was consistent with the simulation in the full range. The events 'not-rejected', which did not have the S2 signal, was not also explained by the neutron flux in Kamioka mine. This result was assumed that the low energy events from the experimental data didn't mainly come from the outside the detector except events form ^{85}Kr but from inside. This kinds of anomalous events was also observed by the UK group in their inorganic scintillator [104, 105]. They explained these events come from the surface of the detector due to ^{214}Po implanted by Rn in the air and they estimated that the material

which was exposed in the air for 1000 hours was enough for them. They reported about the surface of the scintillator, but in our case, the surface of the wires and the PTFE reflector which were exposed in the air should be the main component of the anomalous event. Taking into account the high Rn concentration in Kamioka mine, it is enough for our case. Additionally, it is assumed that the electrons which ionized at the surface would sufficiently collected because they could be trapped by the surface. The UK group succeeded to reduce the anomalous events by polishing the surface of the scintillator less than 10^{-1} times in the low energy region. If we succeed to reduce anomalous events to clean up the wire and the PTFE, the result will be much improved.

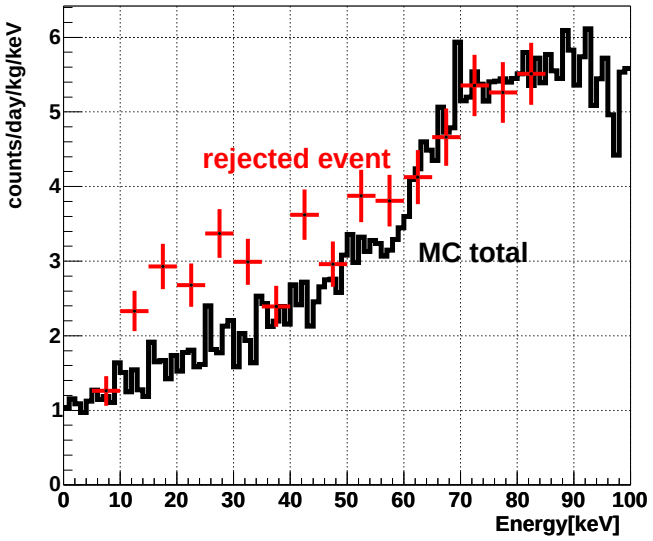

Chapter 9

Future detector

9.1 The design of large Liq.Xe detector

This long electron life time makes it possible to construct a large detector with long drift length ($>$ 1m) and implies realistically to scale up to ton order of detector. Fig.9.1.

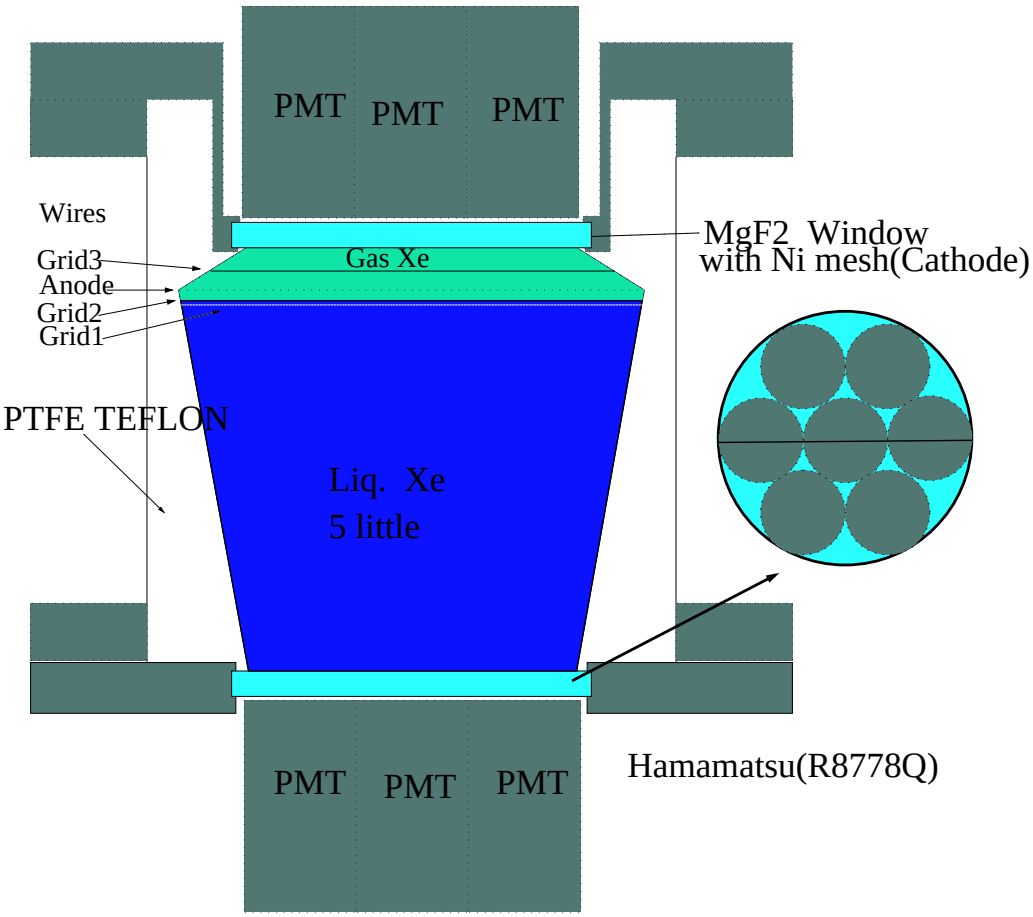

Figure 9.1: 15kg Xe detector

The concepts of design are same as the small prototype. LXe and gas Xe are surrounded by two large MgF_2 windows which are evaporated with Ni meshes and PTFE Teflon. 7 PMTs are mounted on top and bottom sides (total 14 PMTs). Fiducial volumes is 5 liter LXe (15kg). This detector will improve not only statistic of events but also background rate. From the small detector results, the backgrounds come from outside the detector, it is expected that the volume-surface ratio of the detector and using more radioactive clean PMTs lead to reduce the background more than one order of magnitude. The light collection efficiency for this large one was calculated using the same parameter in Section5.5. From this result, the mean light collection efficiency is 15.4%. This value is almost same as the small one.

Parameter	Value
Refractive index MgF_2	1.45
Refractive index Quartz	1.56
Reflective index PTFE Teflon	95% (diffuse)
Absorption length in LXe	1m
Rayleigh scatter	30cm

Table 9.1: Parameters for the Monte Calro simulation.

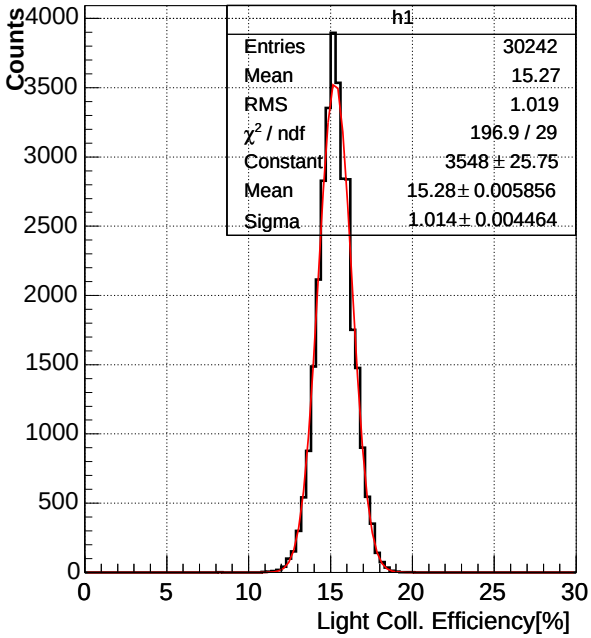

Figure 9.2: Distribution of the light collection efficiency (f_{dp}) for the large detector. The fluctuation (σ / f_{dp}) is 6.9%

9.2 Expected results

Fig.9.3 shows the WIMP-nucleus cross section as a function of WIMP Mass[GeV] with our expected results. This expected result are assumed that 3σ discovery, the anomalous events is negligible to other source (red), 99% rejection with 1kg $\times$ 1 year (green) and the 15kg second phase detector with 15kg $\times$ 1 year (blue). In the case of 15kg detector, 9×10^{-4} events/day/keg/keV background rate after rejection, 1 ppb ^{85}Kr because the number of PMTs per the detector mass is reduced and the volume-surface ratio relative to the prototype 1kg detector is included.

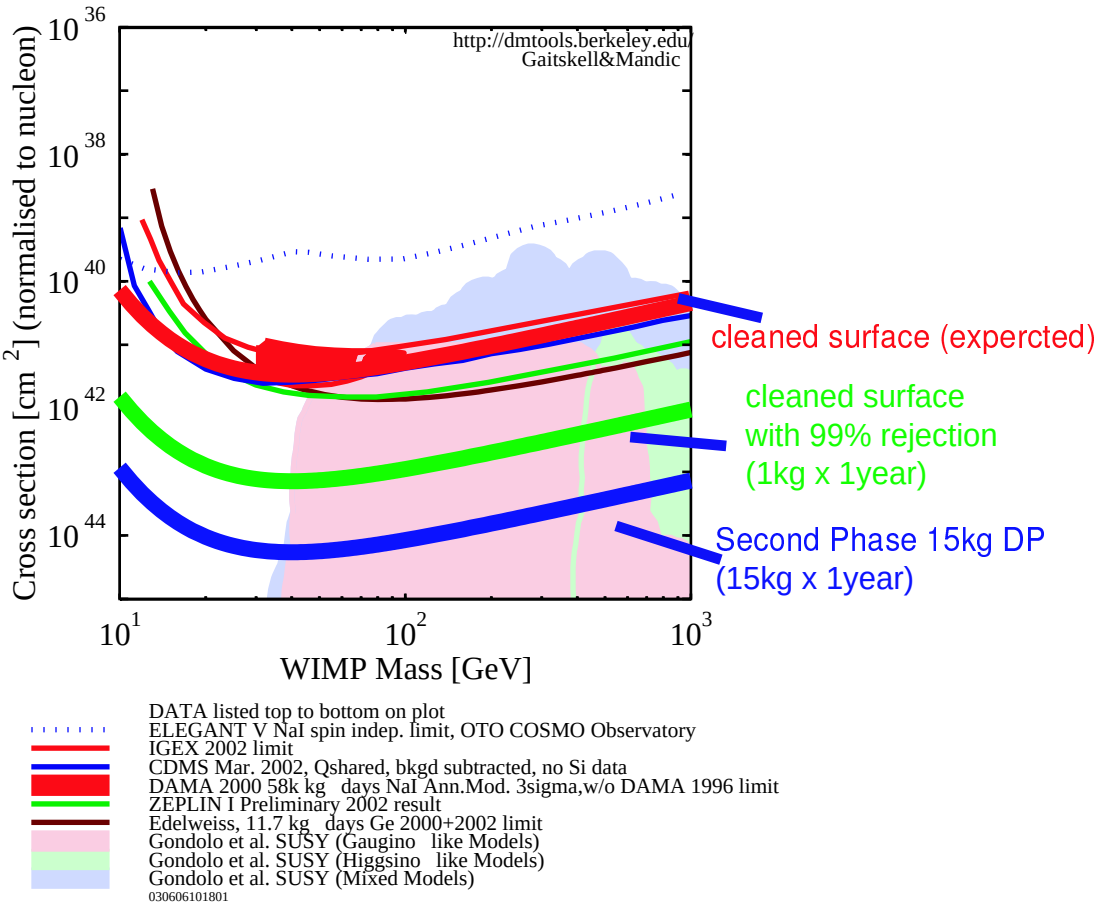

Figure 9.3: the WIMP-nucleus cross section in SI case with our expected 3σ discovery, cleaned surface by 1kg detector (red), 1kg detector with rejecton 99% (green) and the second phaes 15kg detector(bule).

9.3 The idea for other experiments

In addition to WIMPs direct search, there are interesting physics experiments by Xe target such as pp/^{7}Be solar neutrino [81] , ^{136}Xe double beta decay experiments (i.e.[82]) and

gamma ray imaging telescope[106]. Approaches to such experiments are considered using technique as below. It is possible to develop 3D position sensitive detector by setting plurality of PMTs on top using gas proportional scintillation [83]. The z position was informed by drift time like this prototype detector and x-y position by weighted center of S2. It allows us to use gamma ray imaging telescope. Additionally, electron scattering events were recognized by counting number of S2 signals event by event because, for example, one Compton scattering events should have two S2. This method is suitable for pp/^{7}Be and double beta decay experiment.

Chapter 10

Conclusion

- The reflection coefficiency, $R_f = 88 - 95\%$, for PTFE reflector for the LXe scintillation light was obtained.
- The best energy resolution for gamma rays by LXe detector was obtained by this experiment. The energy resolution for LXe with double phase detector is σ/E = 7.1% at 662keV.
- This is the only detector that can obtaine the scintillation efficiency of LXe for gamma rays in the range from 30 keV to 4000keV.
- The electron life time of our LXe detector is estimated approximately 3 msec.
- This is the first experiment that measures both direct and proportional scintillation to identify nuclear recoil from electron recoil with the double phase Xe in the underground laboratory.
- We evaluate the expected result of $\sigma^{\mathrm{SI}}_{\chi-\mathrm{p}}$ and $\sigma^{\mathrm{SD}}_{\chi-\mathrm{p}}$ limits. $\sigma^{\mathrm{SI}}_{\chi-\mathrm{p}}$ limit of $7.4\times10^{-42}\mathrm{cm}^2$ and the $\sigma^{\mathrm{SD}}_{\chi-\mathrm{p}}$ limit of $1.6\times10^{-38}\mathrm{cm}^{-2}$ by 1kg with 99% rejection and $5.6\times10^{-45}\mathrm{cm}^2$ for M_χ = 50 GeVc^{-2}. The 15 kg detector in the next phase is expected to be reached 2 order of magnitude better than the current limit. M_χ dependence of the limits are shown in Fig.9.3.

Acknowledgments

I would like to first thank my advisor Prof. J. Kikuchi for his guidance and support. I would like to thank Prof. S. Suzuki, emeritus Prof. T. Doke for having learned various things from their knowledge, especially, the detector for physics experiment. I have learned many things from Prof. S. Suzuki for his most recent world-wide view of physics and his excellent idea of detector.

I would like to thank XMASS collaborator. I want to express my gratitude to Prof. S. Suzuki, Prof. M. Nakahata, Dr. S. Moriyama, Dr. Y. Koshio, Dr. T. Namba, Dr. M. Shiozawa and Dr. Y. Takeuchi at ICRR university of Tokyo. and Prof. Y. Fukuda at Miyagi university of education. I have learned a lot of things from them, especially, the approach to the physics experiment. Prof. S. Nakamura at National Yokohama university, gave me many information about optical for LXe.

I would like to thank Minowa group in university of Tokyo, Prof. M. Minowa, Dr. K. Miuchi, Dr. A. Takeda and H. Sekiya. They allowed me to use their HPGe detector in the beginning of the experiment and I got the various information of materials and had useful discussion with them.

I would like to thank Super Kamiokande collaborator and the staff of Kamioka Observatory, T. Furuta, K. Yokokawa and M. Mizuhata. They help us to work in the mine.

I would like to thank the member of Kikuchi laboratory in Waseda university, especially, E. Moriguchi, T. Kawabata, K. Kawasaki, M. Wakabayashi and Dr. K. Terasawa. They help me a lot of things in this experiment.

I want to express my gratitude to students at Kamioka Observatory, Y. Ashie, A. Minimino, M. Ishituka, C. Mitsuda, Y. Nakajima and F. Kato. I want to thank K. Ozone and R. Sawada, ICEPP, university of Tokyo, for advising me about DAQ system.

Finally, I would like to thank my parents, T. Yamashita and A. Yamashita for their understanding, help and encouragement.

Appendix A

HP Ge detector in Kamioka mine

Before setting up the detector, the radioactivity of materials were measured by HP Ge detector in Kamioka mine. These measured values are used for selections of the materials or background estimation for the result. Fig.A.1 shows the HPGe set up. The atmosphere around HPGe is purged by Super radon free air to reduce background from the air in Kamioka mine.

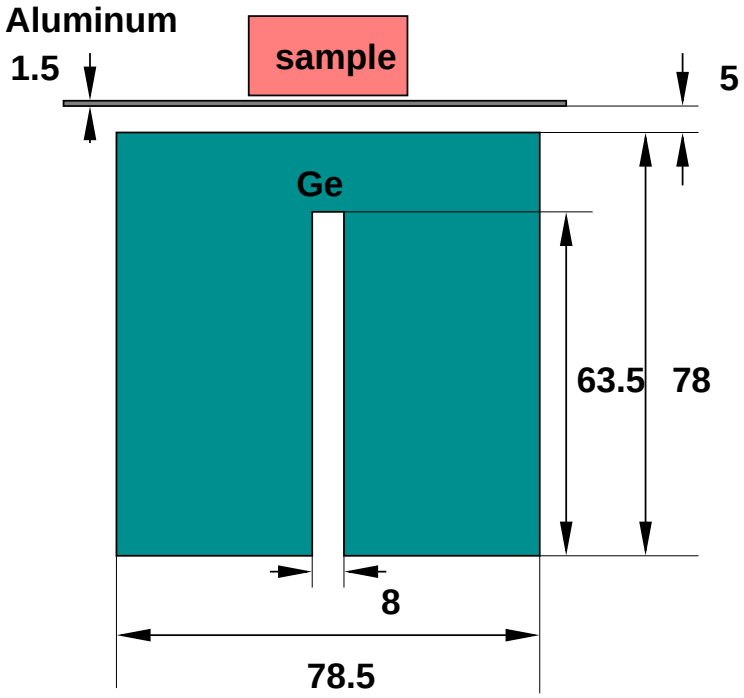

Figure A.1: The size of HPGe detector in Kamioka mine.

Fig.A.2 shows the background spectrum of HPGe. This data was accmulated for 766807 second.

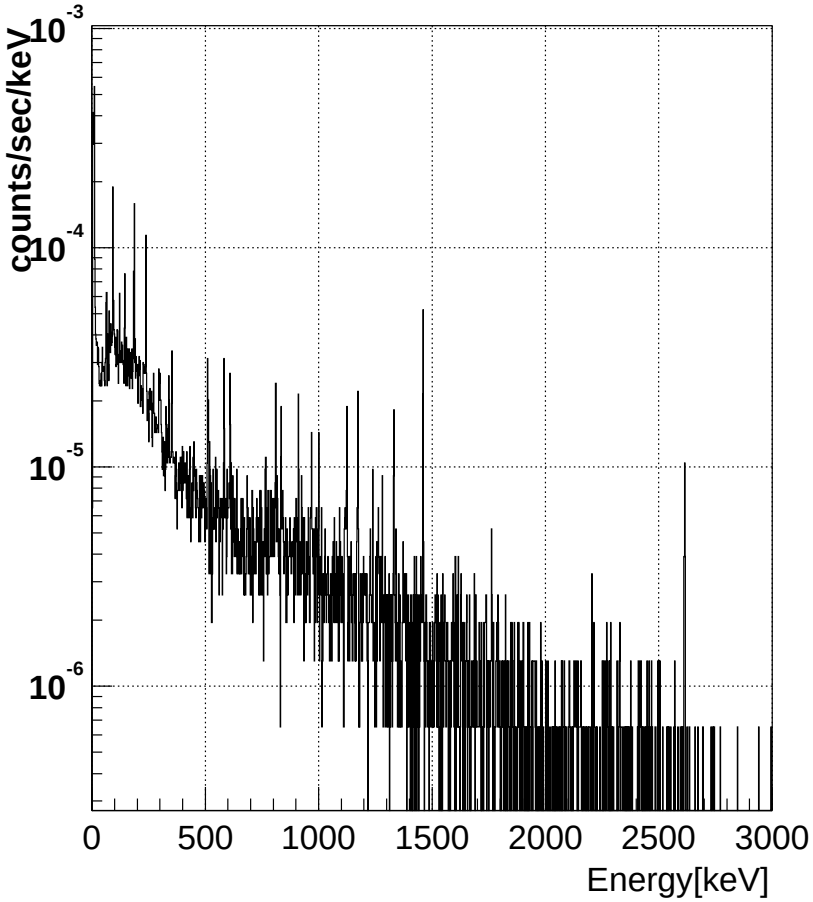

Figure A.2: The background spectrum of HPGe detector in Kamioka mine.

The detection efficiency was caluculated using GEANT3 simulation tool. Fig.A.3 shows the detection efficiency in the range of 0-3000 keV. The point source is used in this simulation, but the shape and materials of samples are included for the value of radioactivity in this thesis.

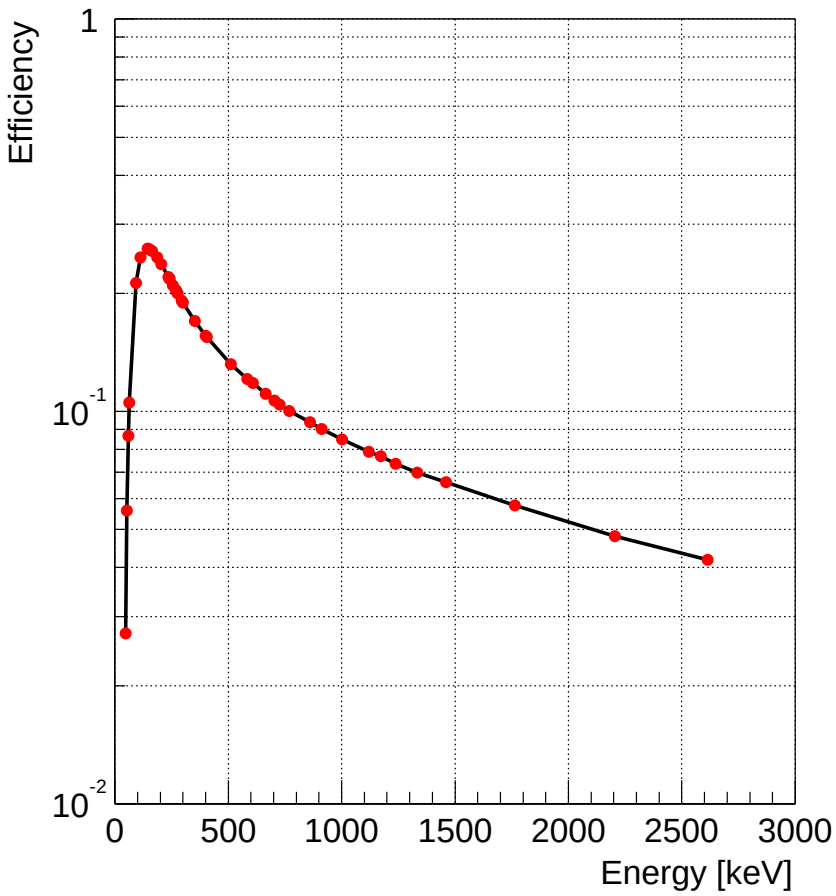

Figure A.3: The simulation of the detection efficiency for HPGe detector. Point source is used in this caluculation.

Bibliography

[1] M. S. Turner, J.A. Tyson Rev. Mod. Phys 71(1999)145.

[2] B. Sadoulet , Rev. Mod. Phys 71(1999)197.

[3] K.G. Begeman, et al.,Mon. Not. R. Astron. Soc. 249(1991)219t.

[4] C.B. Netterfield et al., Astrophys. J. 571(2002)604.

[5] C. Pryke et al., Astrophys. J. 568(2002)46.

[6] R. Stompor et al., Astrophys. J. 561(2001)L7.

[7] S. Perlmutter et al., Astrophys. J. 517(1999)565.

[8] P. DE Bernardis et al., Astrophys. J. 564(2002)559.

[9] Review of Particle physics, Particle Data Group, European Physical Journal C15(2001), URL:http://pdg.obl.gov/

[10] R. A. Flores, Phys. Lett. B215(1988)73.

[11] K. Griest, Nucl. Phys. Proc. Sup. B 91,(2001)393.

[12] Ch. Weinheimer et al., Phys. Lett. B460(1999)219.

[13] Y. Fukuda et al., Phys. Rev. Lett. 81(1998)1562.

[14] E. Daw, Proc. IDM2000 World Scientific, (York, UK,2000) p.487.

[15] K. Yamamoto et al., Proc. DARK2000 (Heidelberg, Germany,2000)

[16] OPAL:CERN-EP/99-XXX(Sept 3,1999).

[17] A. Habig et al., hep-ex/0106024

[18] G.Jungman, M.KAMIONKOWSKI, K.GRIEST, Phys.Rep.267(1996) 195.

[19] R. Bernabei et al., Phys. Lett. B 389(1996) 757.

[20] R. Bernabei et al., Phys. Lett. B 436(1998) 379.

[21] K. Fushimi, Astropart. Phys. 12(1999) 185.

[22] N. J. Spooner et al., Phys. Lett. B 473(2000) 330.

[23] N. J. Spooner et al., Proc. DM 2000, (Marina del Rey, 2000) ed. D. Cline p.365.

[24] S. Cebrián et al., Nucl. Phys. B (Proc. Suppl.) 95(2001)229.

[25] H.V. Klapdor-Kleingrothaus et al., Proc. IDM2000, World Scientific, ed. N. Spooner and V,. Kudryavtsev,(York, UK, 2000) p.415.

[26] J. Jochum et al., Nucl. Phys. B (Proc. Suppl.) 87(2000)70.

[27] A. Benoit et al., astro-ph/0206271v1.

[28] R. Abusaidi et al., Phys. Rev. Lett. 84(2000)5699.

[29] R. Bernabei et al., Phys. Lett. B 424(1998) 195.

[30] R. Bernabei, Prog. Part. and Nucl. Phys. 48(2002)263.

[31] Rick Gaitskell and Vuk Mandic, http://cdms.physics.ucsb.edu/

[32] J.D. Lewin, P.F. Smith, Astropart. Phys. 6(1996) 87.

[33] J. Engel, Phys. Lett. B264(1991) 114.

[34] M.T. Ressell and D.J. Dean, Phys. Rev. C56(1997) 535.

[35] J. Ellis and M. Karliner, Phys. Lett. B341(1995) 397.

[36] D.R. Tovey et al., Phys. Lett. B488(2000) 17.

[37] John Ellis, Andrew Ferstl, Keith A. Olive, Phys. Lett. B481(2000) 304.

[38] A. Bottino et al.,Phys. Lett. B402(1997) 113.

[39] A.F. Pacheco, D.D. Strottman, Phys. Rev. D40(1989) 2131.

[40] M.T. Ressell et al., Phys. Rev. D48(1993) 5519.

[41] N.J.Spooner et al., Phys. Lett. B 321(1994)156.

[42] G.J. Davies et al., Phys. Lett. B 322(1994)159.

[43] F. Arneode et al., Nucl. Instr. and Meth. A449(2000)147.

[44] D. Akimov et al., Nucl. Instr. and Meth. A524(2000)245.

[45] Y. Messous et al., Astropart. Phys.3(1995)361.

[46] G.Gerbier et al., Phys. Lett. B 436(1998)3211.

[47] Drukier et al., Phys. Rev. D 33 (1986)3495.

[48] S. Nakamura, private communication.

[49] T. Doke et. al., Jpn. J. Appl. Phys. 41(2002)1538.

[50] M. Miyajima et. al., IEEE Trans. Nucl. Sci. NS-40(4)(1993)553.

[51] S. Sasaki et. al., Proc. 7th Workshop on Radiation Detectors and their Uses, January 1993, pp. 20-30.

[52] N. Ishida et al., Nucl. Instr. and Meth. A384(1997)380.

[53] G.M. Seidel et al.,Nucl. Instr. and Meth. A 489 (2002)189.

[54] J. L. Pack et al., Phys. Rev. 127(1962)2084.
L. S. Miller et al., Phys. Rev. 166(1968)871.
Y. Yoshino et al., Phys. Rev. A14(1976)438.

[55] T. Doke, Port. Phys. 12(1981)9.

[56] E. Shibamura et al., Proc. Int. Seminar on Swarm Experiments in Atomic Collision Research, Tokyo, 47(1979)

[57] T. Doke et al., Nucl. Instr.and Meth. A420(1999) 62.

[58] M. Miyajima et al., Phys. Rev. A9(1974)1438.

[59] T. Takahashi et al., Phys. Rev. A12(1975)1771.

[60] J. Lindhard et al., Mat. Fys. Medd. Dan. Vid. Selsk. 33, no.10(1963)

[61] A. Hitachi,Proc. IDM2002 World Scientific, (York, UK,2002)

[62] A. Hitachi et al., Phys. Rev. B46(1992)11463.

[63] M. Chen et al., Nucl. Instr. and Meth. A267(1988)43.

[64] I.R. Barabanov et al., Nucl. Instr. and Meth. A310(1991)150.

[65] P. Belli et al., Nucl. Instr. and Meth. B63(1992)297.

[66] M. Miyajima et al., Nucl. INstr. and Meth. B63(1992)297.

[67] V.R. Weidner and J.J.Hsia, J.Opt.Soc.Am.71(1981)No.7

[68] P. Benetti et al., Nucl. Instr.and Meth. A327(1993)203.

[69] P. Benetti et al., Nucl. Instr. and Meth. A329(1993)361.

[70] Proc. idm 2002, 4th International Workshop on the Identification of Dark Matter, York, England,2002.World Scientific, to be published.

[71] Proc. of the Ninth International Workshop on Low Temperature Detectors, Ed.by F.Scott Porter et al. Amer. Inst. of Phys. Vol.605(2002).

[72] A. Benoit et al., Phys. Lett. B 545(2002)43.

[73] M. Bravin et al., Nucl. Instr. and Meth. A444(2000)323.

[74] R. Bernabei et al., Phys. Lett. B 480(2000)23.

[75] S. Suzuki et al., Low Energy Solar Neutrino Detection, World Scientific(2001)91.

[76] E. M. Gushchin et al., Sov. Phys. JETP 55(1982)5.

[77] K. T. Ospanov and I. M. Obodovski, Preprint MIFI, N006-q92, 1992.

[78] T. Tojo, Nucl. Instr. And Meth., A238 (1985)153.

[79] M. Yamashita et al., Proc. IEEE Nucl. Sci. Sympo. Lyon.(2000) 6-155.
M. Yamashita et al. to be submitted to Nucl. Instr. and Meth.

[80] S. Kubota et al, Phys, Rev. B17(1978)2762.
J. Thomas and D.A. Imel, Phys. Rev.A36(1987)614.

[81] Y. Suzuki, Low Energy Solar Neutrino Detection,World Scientific(2001)81.

[82] R. Bernabei et al., Phys. Lett. B 546(2002)23.

[83] A. Bolozdynya et al., Nucl. Instr. and Meth. A385(19996)225.

[84] Y. Suzuki et al, hep-ph/0008296.

[85] S. Moriyama et al, XMASS experiment I , Edited by Y. Suzuki et al., Technique and Application of Xenon Detectors. p.123(2002) World Scientific.

[86] M. Yamashita et al, XMASS experimemt II , Edited by Y. Suzuki et al., Technique and Application of Xenon Detectors. p.136(2002) World Scientific.

[87] T. Hashimoto, Master thesis ,University of Tokai (2002).

[88] Richard B. Firestone et al., Table of Isotopes. CD ROM Edition. Version 1.0 March, 1996.

[89] SAES Pure GAS, Inc.

[90] R. Bernabei et al., Nucl. Instr. and Meth. A482(2002)728.

[91] S. Fukuda et al., Nucl. Instr. and Meth. A 501(2003)418.

[92] H. Sekiya, Master thesis, University of Tokyo (2001)

[93] O. A. Ponkratenko, V. I. Tretyak and Yu. G. Zdesenko Phys. Atom. Nucl. 63(2000)1282.

[94] S.R.Hashemi-Nezhad and L.S.Peak, Nucl Instr. Meth. and A 357(1985)299
K. H. Beckurts and K. Wirts, NEUTRON PHYSICS Chap.7, (SPRINGER-VERLAG, BERLIN, GOTTINGEN, HEIDLBERG, NEW YORK, 1964)

[95] M. Ishitsuka, Master thesis ,University of Tokyo (2001).

[96] L. A. Currie, IEEE Trans. Nucl. Sci. NS-19(1972)119.

[97] V. D. Ashikov et al., Nucl. Instr. and Meth. A 416(1998)179

[98] P. Cauwels et al., Rad. Phys. and Chem. 61(2001)649

[99] Y. Igarashi et al., Jour. of Envi radi. 50(2000)107

[100] measured by T. Namba.

[101] Group T-16, Los Alamos National Laboratory.
http://t2.lanl.gov/

[102] K. Hagiwara et al., Phys. Rev. D66(2002)

[103] K. Miuchi, Doctor thesis ,University of Tokyo (2002),
A. Takeda, Doctor thesis ,University of Tokyo (2003),
K. Miuchi et al., Astropart. Phys. 19(2003)135.

[104] N. J. T. Smith et al., Phys. Lett. B 485(2000)9.

[105] V. A. Kudryavtsev et al., Astoropart. Phys. 17(2002)401.

[106] E. Aprile et al, SPIE Vol.4140(2000)